THE UTILIZATION OF SILICA NANOSPRINGS AS AN INSULATING SUPPORT TO
CHARACTERIZE THE MORPHOLOGY, ELECTRICAL TRANSPORT, AND
OPTOELECTRONIC PROPERTIES OF TWO-DIMENSIONAL NANOCOATINGS

A Dissertation

Presented in Partial Fulfillment of the Requirements for the

Degree of Doctor of Philosophy

with a

Major in Physics

in the

College of Graduate Studies

University of Idaho

by

Peter M. Wojcik

Major Professor: Christine Berven, Ph.D.

Committee Members: David N. McIlroy, Ph.D.; F. Marty Ytreberg, Ph.D.;

D. Eric Aston, Ph.D.

Department Administrator: John Hiller, Ph.D.

December 2020

AUTHORIZATION TO SUBMIT DISSERTATION

This dissertation of Peter M. Wojcik, submitted for the degree of Doctor of Philosophy with a major in Physics and titled "The Utilization of Silica Nanosprings as an Insulating Support to Characterize the Morphology, Electrical Transport, and Optoelectronic Properties of Two-Dimensional Nanocoatings," has been reviewed in final form. Permission, as indicated by the signatures and dates below, is now granted to submit final copies to the College of Graduate Studies for approval.

Major Professor: _____ Date: _____
Christine Berven, Ph.D.

Committee Members: _____ Date: _____
David N. McIlroy, Ph.D.

_____ Date: _____
F. Marty Ytreberg, Ph.D.

_____ Date: _____
D. Eric Aston, Ph.D.

Department Administrator: _____ Date: _____
John Hiller, Ph.D.

ABSTRACT

This dissertation explores the nucleation, evolution, and growth dynamics of silica nanosprings and the utilization of silica nanosprings as an insulating support to characterize the morphology, electrical transport, and optoelectronic properties of two-dimensional nanocoatings. The primary results of this research are threefold. First, we identify the mechanisms of initial formation and growth dynamics of silica nanosprings. Second, we coat the surface of silica nanosprings with a novel conductive carbon to create a core–shell structure and definitively identify that the conductive carbon is a nanocrystalline graphitic layer consisting of an agglomeration of carbon nanospheres formed by the accretion of graphitic flakes. Third, we observe the photoconductive behavior of a single ZnO-coated silica nanospring, present models to explain the photoconduction and recombination mechanisms responsible for the observed sub-bandgap photocurrent rise and decay behavior, and present a phenomenological model to describe the characteristics of the saturation photocurrent dependence on excitation intensity.

A single silica nanospring is composed of multiple individual amorphous silica nanowires bound together via a common catalyst to form a larger, well-defined helical structure with a wire diameter of ~70–500 nm, an outer diameter of ~200–1000 nm, and lengths on the order of hundreds of microns. Until now, the initial phases of formation and growth dynamics of this type of silica nanospring had not been explored. We find that the low-temperature growth conditions facilitate the formation of an asymmetrically-shaped gold catalyst. A row of silica nanowires is formed in an energetically favorable process beneath the gold catalyst. The varying growth rates of the individual nanowires produce an asymmetry in the interfacial surface tension and a corresponding variable work of adhesion along the outer boundary of the catalyst–nanowires interface. The variable work of adhesion provides the asymmetry necessary for the catalyst's helical precession, which subsequently produces the silica nanospring's helical morphology.

The surface of silica nanosprings can be coated with an assortment of conducting and semiconducting materials to create a multifunctional nanomaterial that can be utilized in a wide variety of applications. One of these conducting materials, referred to as graphite from the University of Idaho thermolyzed asphalt reaction (GUITAR), has been coated onto silica

nanosprings, and its structural and electrical properties have been investigated. Using a silica nanospring as a platform for GUITAR has allowed, for the first time, transmission electron microscopy images of a GUITAR coating that fully reveal its morphology. Images of a GUITAR coating obtained from scanning electron microscopy, transmission electron microscopy, and atomic force microscopy, together indicate that a GUITAR coating on a silica nanospring is a ~100 nm thick layer composed of an agglomeration of carbon hemispheres ~50–100 nm in diameter formed by the accretion of graphitic flakes ~1–5 nm in diameter. A Raman spectroscopic analysis of GUITAR and the measurements of the electrical resistivity and temperature coefficient of resistivity of 11 single GUITAR-coated silica nanospring electrical devices indicate that GUITAR is a form of nanocrystalline graphite.

Polycrystalline ZnO was coated onto silica nanosprings using atomic layer deposition, and an electrical device consisting of a single ZnO-coated silica nanospring was fabricated and used to investigate the optoelectronic properties of the ZnO layer using near-ultraviolet (405 nm) and sub-bandgap (532 and 633 nm) excitation. The photocurrent responses of all three excitation sources display a typical two-step fast and slow rise and decay response. Physical models are presented and propose that the photocurrent rise and decay characteristics depend on the excitation energy and the trapping of electrons and holes in intermediate defect levels within the bandgap. A phenomenological model is presented to explain the breaks in the slopes of the saturation photocurrent versus excitation intensity profile for each excitation source. We find that these slopes are a function of the transition probabilities of defect states, the number of carriers available to populate the conduction (valence) band, and the rate at which electrons and holes recombine.

ACKNOWLEDGEMENTS

This dissertation would not be possible without the many people who have supported and guided me during this long journey. First and foremost, I would like to thank my major professor, Dr. David N. McIlroy, for allowing me to join his research group and conduct research in his laboratory. I am grateful for the continuous financial support he provided during his tenure at the University of Idaho through the Office of Naval Research and the Microproducts Breakthrough Institute. Dr. McIlroy possesses an in-depth knowledge of condensed matter physics and I have been fortunate to have the opportunity to learn from him. I would like to express my deepest appreciation to Dr. Christine Berven for providing thoughtful insight into experimental design and teaching methodology, and for her general guidance and continuous encouragement throughout my doctoral studies at the University of Idaho. Dr. D. Eric Aston, thank you very much for your thoughtful discussions regarding the minutiae of the atomic force microscope I used in my research. Dr. F. Marty Ytreberg, you have been a great teacher and thank you for providing me with an overly powerful workstation from your laboratory.

I would like to express my appreciation to Dr. I. Francis Cheng for allowing me to conduct research in his laboratory and evoking interest in the carbon material, GUITAR, he created in his laboratory. Dr. Cheng's knowledge, insight, and previous research were instrumental in the completion of my research identifying the structure of GUITAR. Dr. Giancarlo Corti, thank you very much for your thoughtful discussions regarding research techniques and the time you spent training me to operate cleanroom and laboratory equipment. I would like to sincerely thank Dr. Thomas Williams for his unwavering patience and the time he spent training me to operate and continuously improve my imaging techniques using the scanning electron microscope. Dr. Williams also spent a significant amount of time imaging my samples with a transmission electron microscope. These images, specifically the transmission electron microscopy images of a GUITAR coating on a silica nanospring, were essential to the identification of GUITAR's structure, and I cannot thank Dr. Williams enough for this invaluable contribution to my research. Thank you also, Mr. John Failla and Mr. Charles Cornwall. Mr. Failla produced many machine parts that

were essential for the operation of experimental equipment. I am very grateful for your time, patience, and permission to work in the machine shop.

I would like to acknowledge the many professors I have been fortunate to work with and who have inspired and prepared me for every subsequent step of my education. I am extremely grateful to Dr. Ethan Minot at Oregon State University for allowing me to join and work in his research group. The experimental skills and knowledge I acquired under Dr. Minot's guidance were vital to my success as an experimentalist at the University of Idaho. I would like to sincerely thank all my former professors at Central Washington University: Dr. Andrew Piacsek, Dr. Michael Braunstein, Dr. Michael Jackson, Dr. Bruce Palmquist, and Dr. Timothy Melbourne. As a first-generation student, unsure of what lay ahead in higher education, I received from them the information and confidence I needed to succeed in all facets of my education. They are also the most influential teachers I have had the fortunate opportunity to learn from and have motivated me to continuously improve my teaching methodologies. I hope I can provide the same level of inspiration to future students as they did to me. I would like to express my deepest gratitude to the late Dr. Kelly Casey, who initially sparked my interest in physics at Yakima Valley Community College and began this long journey.

I gratefully acknowledge the assistance of all my laboratory group members and the other students I had the opportunity to work with at the University of Idaho. Dr. Pavel V. Bakharev and Dr. Blaise-Alexis Fouetio Kengne, thank you for the time you spent training me to operate laboratory and cleanroom equipment. Dr. Bakharev's knowledge of physics is inspiring, and his previous work in our laboratory was invaluable for the completion of my research. Special thanks to Dr. Negar Rajabi for her patience and contributions to my research. I am also grateful to Dr. Dinesh Thapa, Dr. Jesse Huso, Dr. Isaiah Gyan, and Dr. Haoyu Zhu for their time, patience, and contributions to my research.

Finally, I would like to acknowledge the unwavering support of my mother. She has provided an unparalleled level of care and guidance throughout my life. Words cannot express how much I sincerely appreciate the time, effort, and patience she has put forth during my undergraduate and graduate studies.

For my grandfathers.

TABLE OF CONTENTS

LIST OF FIGURES

LIST OF TABLES

STATEMENT OF CONTRIBUTION

This dissertation mainly consists of three published journal articles. Each article is presented as a separate chapter. The first page of each chapter includes the authors involved in the research for the respective article. Their contributions, and the contributions of others who are not listed as authors, are summarized below. All the material presented in this dissertation that is not summarized below was prepared by Peter M. Wojcik and reviewed and edited by David N. McIlroy and Peter M. Wojcik. David N. McIlroy supervised the research and was responsible for the acquisition of funding in all journal articles.

Chapter 2: The experiments and methodology were conceptualized by Peter M. Wojcik and David N. McIlroy. Peter M. Wojcik performed all experiments and acquired all scanning electron microscopy images. Thomas Williams acquired the transmission electron microscopy images. The data analysis was performed by Peter M. Wojcik, Pavel V. Bakharev, Giancarlo Corti, and David. N. McIlroy. Peter M. Wojcik prepared the original draft. The draft was reviewed and edited by David N. McIlroy and Peter M. Wojcik.

Chapter 3: The experiments and methodology were conceptualized by Peter M. Wojcik, David N. McIlroy, and I. Francis Cheng. David Estrada and Paul H. Davis supervised the acquisition of Raman spectroscopy data. Peter M. Wojcik performed the silica nanospring growth, GUITAR deposition, and electrical characterization; he also acquired the scanning electron microscopy and atomic force microscopy images, and analyzed all data. Thomas Williams acquired the transmission electron microscopy images. Negar Rajabi and Peter M. Wojcik fabricated the single GUITAR-coated silica nanospring electrical devices. Twinkle Pandhi acquired the Raman spectroscopy data. Haoyu Zhu and Paul H. Davis wrote a portion of the introduction and Raman spectroscopy experimental details; Peter M. Wojcik prepared the rest of the original draft. The draft was reviewed and edited by David N. McIlroy, Paul H. Davis, and Peter M. Wojcik.

Chapter 4: The experiments and methodology were conceptualized by Peter M. Wojcik and David N. McIlroy. Peter M. Wojcik performed the silica nanospring growth, fabrication of the single ZnO-coated silica nanospring device, electrical and optoelectronic characterization, and acquired the scanning electron microscopy images. Pavel V. Bakharev performed the deposition of ZnO on silica nanosprings. Negar Rajabi acquired and analyzed

the x-ray diffraction data. Lyndon D. Bastatas conceptualized the phenomenological model for the dependence of the saturation photocurrent on excitation intensity and analyzed the model's relevant data. Peter M. Wojcik analyzed all other data. Lyndon D. Bastatas wrote a portion of the section regarding the saturation photocurrent dependence on excitation intensity, and Negar Rajabi wrote the x-ray diffraction characterization section; Peter M. Wojcik prepared the rest of the original draft. The draft was reviewed and edited by David N. McIlroy, Pavel V. Bakharev, and Peter M. Wojcik.

CHAPTER 1

Introduction

1.1   Introduction to Nanoscience, Nanotechnology, and Nanomaterials

Nanoscience seeks to understand the novel physical properties of materials that emerge when one or more of their dimensions are reduced to a critical nanoscale size in the range of ~1 to 100 nm. Shrinking a material down to this nanoscale size produces an enhanced surface-area-to-volume ratio and reveals peculiar quantum phenomena, affecting strength, magnetic, optical, electrical, and optoelectronic material properties. The discoveries of these unique material properties exclusive to the nanoscale regime have accelerated the advancement of science and technologies in the physical, chemical, and biological sciences [1].

The evolving applications of nanoscience are grouped into a field referred to as nanotechnology, a term coined by Norio Taniguchi in 1974 that was used to describe the control of semiconductor processes on the order of nanometers [2]. Nanotechnology is a broad field encompassing a wide range of disciplines that focus on the application, manipulation, characterization, and production of materials at the nanoscale range, where material properties differ from those of their bulk constituents.

Despite the recent developments in nanoscience and nanotechnology, the concept of nanotechnology is not new. The earliest inquiry into possible technological applications of the nanoscale realm is commonly attributed to Dr. Richard P. Feynman's 1959 science lecture entitled "There's Plenty of Room at the Bottom: An Invitation to Enter a New Field of Physics" [3]. In this lecture, Feynman contemplated writing the Encyclopedia Britannica on the head of a pin, the miniaturization of the computer, miniaturization by evaporation, and the manipulation and rearrangement of individual atoms and molecules [3]. Sixty years later, nearly all the concepts presented in Feynman's lecture are actively being investigated by various nanoscience and nanotechnology researchers. Notable nanotechnological ideas proposed by Feynman that have since come to light include the manipulation and positioning of individual atoms via scanning tunneling microscopy [4, 5]; the miniaturization of the computer via the reduction of transistor gate dimensions from 10 μm in the 1970s [6] to 2.5 nm in 2018 [7]; and the manipulation of individual molecules via dip-pen nanolithography, a nanofabrication process that utilizes a scanning probe microscopy technique to create high-resolution molecular patterns [8].

Many nanomaterials have been revealed since the early discoveries of fullerenes in 1985 [9] and carbon nanotubes in 1991 [10]. Consequently, nanomaterials have been categorized according to shape and dimensionality. Some examples of nanomaterial shapes include nanoparticles, nanospheres, quantum dots, nanotubes, nanowires, nanocoils, nanosprings, and nanosheets. Nanomaterials are also classified according to their dimensionality, where the dimensionality is defined by the number of dimensions that are outside the nanoscale range (~1–100 nm) [11]. For example, zero-dimensional (0D) nanomaterials have no dimensions greater than 100 nm, the most common of which are nanoparticles, nanospheres, and quantum dots. One-dimensional (1D) nanomaterials have one dimension greater than 100 nm and include nanotubes, nanorods, and nanowires. Two-dimensional (2D) nanomaterials have two dimensions greater than 100 nm and include nanosheets and nano-thin films. Three-dimensional (3D) nanomaterials have three dimensions greater than 100 nm and include bundles of nanowires or nanotubes, bulk powders, and dispersions of nanoparticles. A nanostructure that is particularly important to this dissertation is the silica nanospring (SNS), which is composed of multiple silica nanowires that are bound together to form a larger, well-defined helical structure. Figure 1.1 shows a variety of nanomaterial shapes classified by their dimensionality.
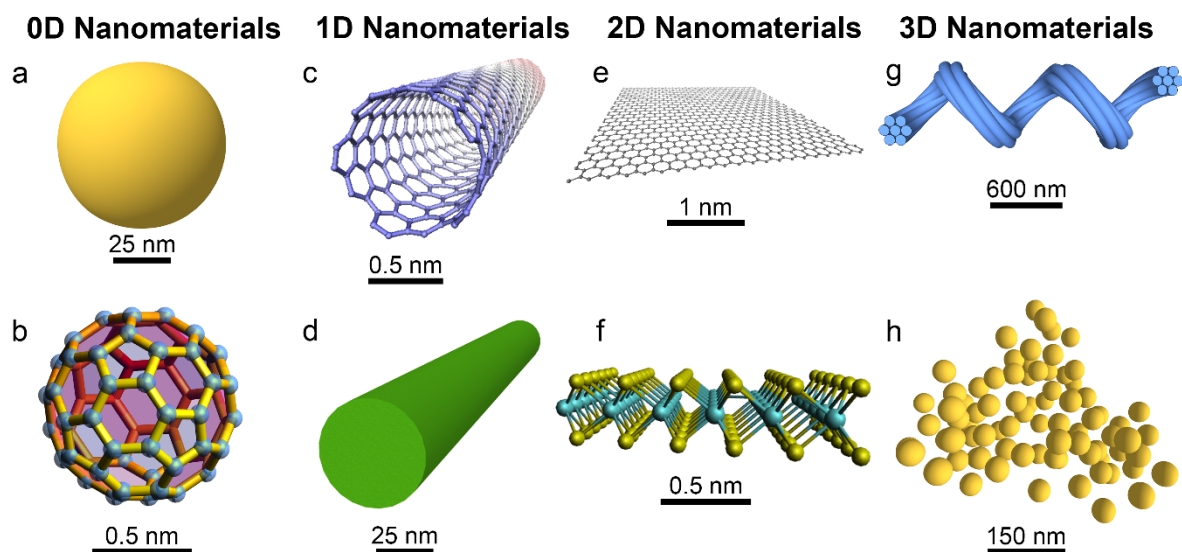
Figure 1.1 A variety of nanomaterial shapes classified by dimensionality. Scale bars are shown below each respective nanomaterial. (**a**) Gold nanoparticle. (**b**) Buckminsterfullerene. (**c**) Carbon nanotube. (**d**) Nanowire. (**e**) Graphene. (**f**) Molybdenum disulfide monolayer. (**g**) SNS. (**h**) Dispersion of gold nanoparticles.

At the forefront of nanotechnology research are carbon-based materials. These include: graphene, a 2D sheet of sp^2 hybridized carbon atoms; carbon nanotubes, 1D hollow cylinders comprised of rolled-up sheets of graphene; and other allotropes of carbon such as nanocrystalline graphite and amorphous carbon. Carbon nanotubes and graphene exhibit ultrahigh mobility [12, 13], excellent thermal conductivity [14, 15], superior mechanical strength [16, 17], and ultrahigh surface area [18, 19], which make them highly attractive candidates for applications in solar energy conversion [20, 21], photodetection [22, 23], biological sensing [24, 25], desalination [26, 27], wearable electronics [28, 29], and energy storage [30–33].

Nanocrystalline graphite and amorphous carbon are other interesting allotropes of carbon that are used in and are promising candidates for a broad range of applications due to their unique material properties and diverse nanostructured morphologies. Nanocrystalline graphite and amorphous carbon lack a crystalline structure and are comprised of random arrangements of sp^2 hybridized carbon layers with a fraction of sp^3 hybridized carbon. The sp^2:sp^3 fraction can be used to determine the amount of disorder in the material and distinguish nanocrystalline graphite from amorphous carbon [34]. Nanocrystalline graphite and amorphous carbon form several types of nanomaterials including nanofibers, nanoparticles, nano-foams, and nano-thin films [35], and can be combined with other nanomaterials to form nanocomposites [35]. They are also easy to synthesize, cost-effective, and have a high specific surface area in the form of nanoparticles, nano-foam [35], and when coated as a nano-thin film on the surface of nanowires and SNSs. These characteristics make nanocrystalline graphite and amorphous carbon excellent candidates for applications in antireflective coatings [36], temperature and chemical sensors [37], electron field emission cathodes [38], ultracapacitors [39], fuel cells [40], batteries [41, 42], and biological sensors [43].

A new type of nanocrystalline graphite dubbed graphite from the University of Idaho thermolyzed asphalt reaction (GUITAR) has recently become of interest due to its unique electrochemical properties [43–46]. Despite having morphologic and spectroscopic characteristics similar to graphite when coated as a thin-film on a flat substrate [47], GUITAR displays superior heterogeneous electron transfer kinetics at its basal plane when compared to graphites, graphene, and other carbon allotropes [44, 48]. GUITAR also

exhibits greater corrosion resistance compared to other graphitic materials [44–46]. Additionally, GUITAR is cost-effective, easily synthesized via the pyrolysis of roofing tar [47, 49] or a chemical vapor deposition process with a vegetable oil precursor [46], and can be coated on a variety of flat substrates and on the surface of SNSs [47, 49]. These characteristics make GUITAR an exceptional candidate for applications in biological sensing [43], energy storage and conversion [39–42, 46, 50], and water purification [48].

Zinc oxide (ZnO) is another multifunctional material on the forefront of nanoscience and nanotechnology research owing to its unique material properties and diverse nanostructured morphologies. ZnO is an n-type semiconductor with a direct wide 3.37 eV bandgap and large 60 meV exciton binding energy at room temperature. ZnO displays piezoelectric [51] and pyroelectric [52] properties, has a high electron mobility [53], is easily synthesized [54], and is chemically stable [55], non-toxic, and cost-effective. ZnO forms a variety of nanostructures, including nanowires, nanosprings, nanobelts, nanoparticles, and can be coated as a nano-thin film on the surface of SNSs [56–59]. The direct wide bandgap and large exciton binding energy make ZnO an excellent candidate for applications in ultraviolet (UV) photodetection [60–64] and light-emitting diodes [65, 66]. Photodetection responses in the visible light region have been observed in polycrystalline ZnO [56, 67] and surface functionalized ZnO nanowires [68, 69], which make ZnO an attractive material for solar energy conversion applications [53, 70]. ZnO is also commonly configured as a field-effect transistor and utilized in biological sensing [71, 72] and UV photodetection [73, 74] applications. Additionally, the adsorption of atmospheric oxygen on the surface of ZnO creates a surface reactive layer that is utilized in gas sensing applications [57–59, 75, 76].

1.2   Composite and Core–Shell Nanomaterials

Composite nanomaterials, or nanocomposites, are formed by combining two or more materials with distinct differences in material properties and structure to create new types of nanomaterials and architectures with enhanced physical properties that are not observed in their constituents independently [77, 78]. At least one constituent in a nanocomposite must have at least one dimension in the nanoscale range. The many possible combinations of materials and the ability to tune a material to suit a specific application make nanocomposites promising candidates for a broad range of applications [78]. For example,

ZnO nanowire photodetectors can be tuned to the visible spectrum by surface functionalization with carbon nanodots [69] and gold nanoparticles [68], and used in solar energy conversion applications. SNSs have been coated with metal nanoparticles and shown to be effective Fischer–Tropsch catalysts [79] and to increase the hydrogen storage capacity of SNS mats [80]. The surface of SNSs have also been functionalized with various materials and used to immobilize enzymes in microreactors [81] and as biological sensing devices [82].

Core–shell nanomaterials are a subclass of nanocomposites consisting of an inner (core) material and an outer (shell) layer forming a core–shell structure. The core material can be covered partially or fully by the shell layer as long as the two layers are distinguishable [83]. SNSs are often utilized as the core in a core–shell nanostructure by coating the outer surface of the SNS with one or more materials to create a multifunctional nanomaterial with a high surface-area-to-volume ratio. SNS core–shell nanostructures have been used in and are promising candidates for a diverse range of applications. For example, polycrystalline ZnO-coated SNSs have been used as chemical sensors [57–59, 75, 76] and photodetectors [56, 67]. Metal-oxide/metal multilayer-coated SNSs have been shown to improve the structural connection between orthopedic materials and bone [84]. Platinum-coated SNSs have potential uses in catalytic combustion applications [85]. SNSs have also been coated with GUITAR to create a nanocomposite that is a promising candidate for energy storage and conversion [41, 46, 50] and biological sensing [43] applications.

In this dissertation, core–shell structures were created by coating nano-thin film outer shell layers of GUITAR and polycrystalline ZnO on a SNS core. These core–shell structures were created as a preliminary step to investigate the electrical properties and morphology of GUITAR, and the electrical and optoelectronic properties of polycrystalline ZnO. Details of the GUITAR and polycrystalline ZnO deposition methods are described in chapters 3 and 4, respectively. A model of a SNS core–shell structure and scanning electron microscope and transmission electron microscope images of GUITAR-coated and ZnO-coated SNS core–shell structures are shown in Figure 1.2. Utilizing the SNS as a platform for a GUITAR nano-thin film has fully revealed GUITAR's morphology via detailed transmission electron microscope images of a GUITAR coating on a SNS. These images, in conjunction with SEM and atomic force microscopy images, aided in the identification of GUITAR's

morphology and the classification of GUITAR as a form of nanocrystalline graphite [49].
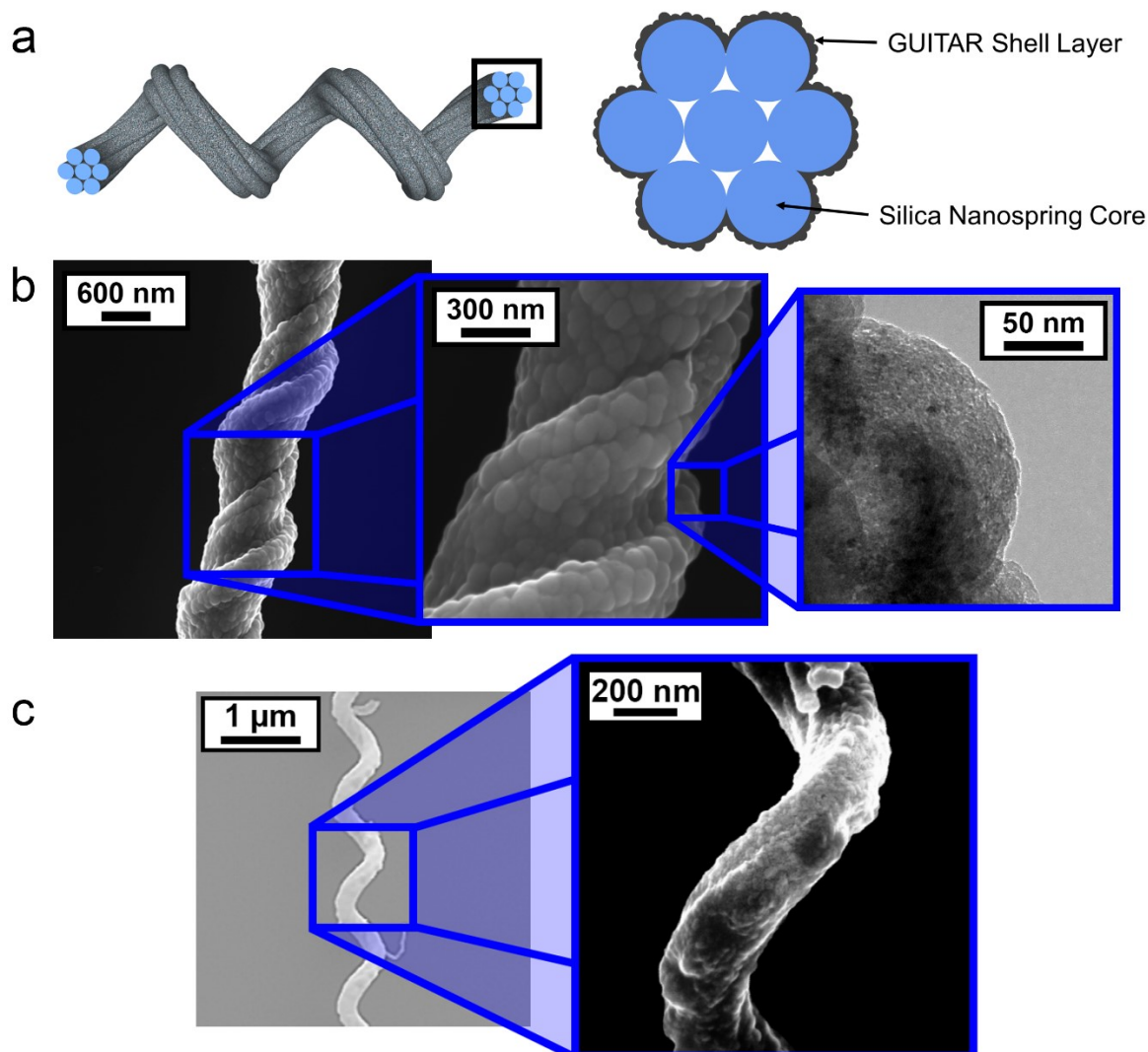
Figure 1.2 (**a**) A 3D model of a SNS used as a core–shell structure. The right-hand image shows a cross-sectional view of a GUITAR coating on a SNS. (**b**) Scanning electron microscope and transmission electron microscope images of a GUITAR coating on a SNS. The far right transmission electron microscope image shows an individual carbon hemisphere in the GUITAR coating. (**c**) Scanning electron microscope images of a ZnO-coated SNS.

1.3 Nanomaterials Characterization

The structural, compositional, electronic, and optoelectronic characterization of nanomaterials requires a broad range of characterization techniques and tools to probe their unique material properties. This dissertation utilizes various characterization techniques and

tools to investigate the initial stages of formation and growth dynamics of SNSs, the electrical, morphological, and structural properties of GUITAR, and the electrical, structural, and optoelectronic properties of polycrystalline ZnO. This section presents brief introductions to the characterization techniques and tools that were used to investigate the initial stages of formation and growth dynamics of SNSs, and the morphology and structure of GUITAR and polycrystalline ZnO. The characterization techniques and motivations for studying the electrical properties of GUITAR and the optoelectronic properties of polycrystalline ZnO are discussed in sections 1.4 and 1.5. The nanomaterials characterization techniques highlighted in this section are not a complete list or comprehensive review of the characterization techniques and tools currently used in the fields of nanoscience and nanotechnology. If the reader would like an in-depth review of common nanomaterials characterization techniques, we refer them to the following literature reviews: Kalantar-zadeh and Fry [86], Kumar et al. [87], and Salame et al. [88].

1.3.1   Electron Microscopy

Electron microscopy uses an electron–matter interaction to probe the surface topography, morphology, crystallographic structure, and chemical composition of materials. The general principle of operation involves focusing an energetic beam of electrons on a sample. The resulting electron–matter interactions are recorded by an array of detectors, which are then processed via computer software to create an image of the sample or give other analytical information. Electron microscopy instruments are perhaps the most utilized characterization tools in nanoscience and nanotechnology due to their nanoscale resolution, large depth of field, ability to characterize organic and inorganic materials, and ability to characterize morphological, topographical, and analytical information. Two electron microscopy techniques have been utilized in this dissertation; scanning electron microscopy (SEM) and transmission electron microscopy (TEM).

SEM is a versatile and valuable tool for investigating the surface topography, morphology, and chemical composition of materials. The resolution of a scanning electron microscope is ~1 nm [87] and can vary depending on a number of factors, including the composition of the sample, and the energy and size of the beam [87, 89]. SEM's depth of field, the distance above and below the plane of focus, is about 300 times greater than an

optical microscope, corresponding to a depth of field of ~10 µm at 10,000× magnification [88]. Compared to other microscopy techniques, the advantages of SEM include a wide range of adjustable magnification, a large depth of field, an adjustable tilting state that allows imaging of the sample from a wide range of angles, and an ability to collect additional analytical data. A schematic diagram of a scanning electron microscope is shown in Figure 1.3(a). The electron source at the top of the column emits energetic (primary) electrons that are focused and raster scanned on the sample via a set of lenses. Primary electrons interact with the sample and produce secondary electrons, backscattered electrons, and characteristic x-rays. Multiple detectors collect the signals produced from these interactions and the signals are analyzed with computer software. Secondary electrons are primarily used to create an image of the sample, while characteristic x-rays are used to analyze the sample's chemical composition.
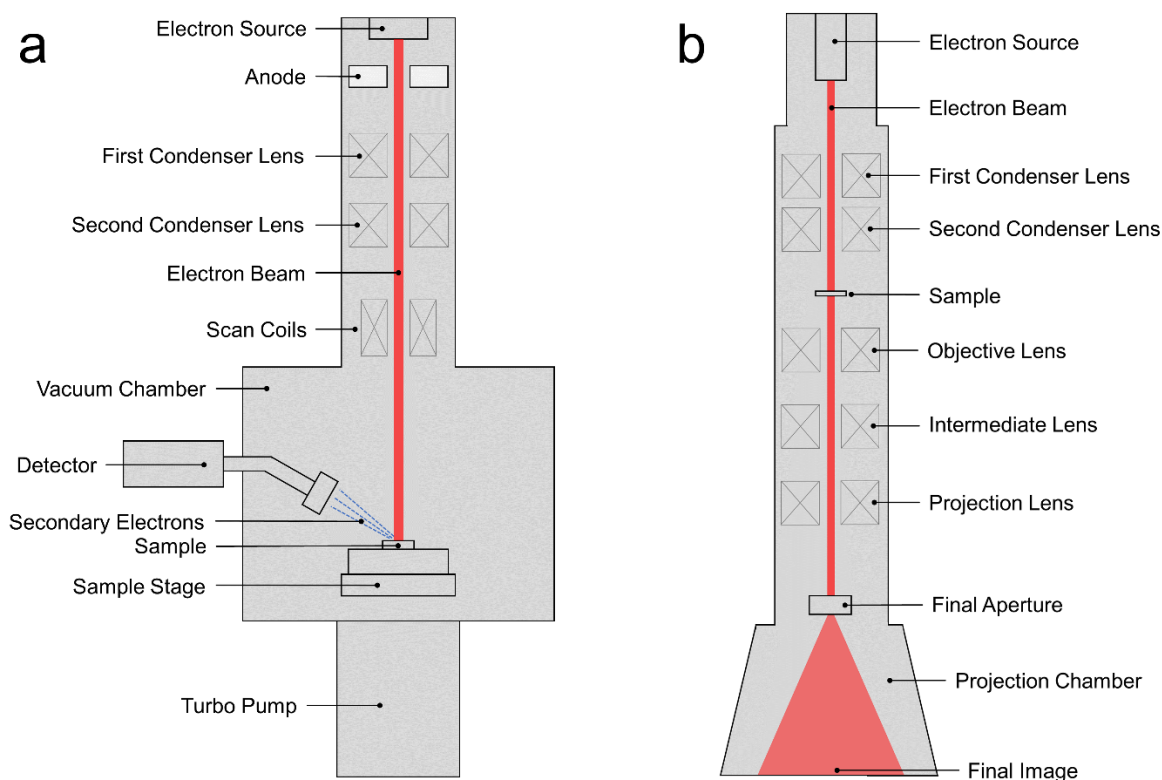
Figure 1.3 Schematic diagrams of a (**a**) scanning electron microscope and a (**b**) transmission electron microscope.

The components of a transmission electron microscope, e.g., the electron source and lenses, are similar to a scanning electron microscope. However, the required sample thickness, the sample's position in the column, and how signals are collected are quite different. Figure 1.3(b) shows a schematic diagram of a transmission electron microscope. An energetic beam of electrons at the top of the column is focused and transmitted through a ~50 to 100 nm thick [88] sample. The electrons from the beam interact with the electrons in the sample and are transformed into unscattered, elastically scattered, or inelastically scattered electrons, yielding x-rays, auger electrons, and light [88, 90]. These transmitted electrons are then focused using a set of lenses to produce a shadow image of the sample or an electron diffraction pattern. TEM has much greater spatial resolution than SEM, resolving objects separated by less than 0.2 nm [88] and providing images of atomic lattice structures [86, 91]. TEM drawbacks include the required thickness of the sample to facilitate the transmission of electrons and possible damage to the sample during preparation and data collection [88].

SEM and TEM have been utilized extensively in this dissertation. In chapter 2, we use a combination of SEM and TEM to investigate the initial stages of formation of the gold catalyst and SNS growth. In chapter 3, we use SEM and TEM to examine the morphology of a GUITAR coating on a SNS and the single GUITAR-coated SNS electrical devices used in the experiments. Detailed TEM images of a GUITAR-coated SNS fully revealed the morphology of an individual carbon hemisphere in a GUITAR coating, which aided in identifying the structure and formation of a GUITAR coating on a SNS [49]. In chapter 4, we use SEM to examine the surface morphology of polycrystalline ZnO and the single polycrystalline ZnO-coated SNS electrical device used in the experiments.

1.3.2 Atomic Force Microscopy

In 1982, Binnig and Rohrer invented the scanning tunneling microscope and showed that the instrument could probe surface topography with atomic-scale resolution [92]. This revolutionary discovery earned Binnig and Rohrer the 1986 Nobel Prize in Physics and spawned a vast array of scanning tunneling microscopy (STM) related techniques now referred to as scanning probe microscopy (SPM). SPM techniques characterize surface topography and other surface properties on the atomic scale. Four years after the invention

of the STM, Binnig, Quate, and Gerber invented another revolutionary SPM technique called atomic force microscopy (AFM) [93]. Unlike STM, AFM does not require a conductive sample and can probe the surface topography of a variety of materials.

Figure 1.4 shows a schematic diagram of the working principles of AFM and a 3D AFM image of a GUITAR coating on a silicon substrate. A small probe tip at the end of a microscale cantilever is oscillated close to the sample with a piezoelectric shaker, and the sample is raster scanned with a piezoelectric stage. When the probe tip is brought within a few nanometers of the surface, the resulting attractive and repulsive forces between the probe tip and the atoms on the surface of the sample cause the cantilever to deflect. A laser is reflected off the top of the cantilever tip and focused onto a photodetector to measure the cantilever's vertical and horizontal deflections as a function of position. A feedback mechanism monitors the probe tip position on the photodetector and the corresponding force, maintaining a constant amplitude of oscillation. Computer software then generates a 3D image of the surface topography with atomic-scale vertical resolution [94]. In chapter 3 and in an investigation of the electrochemical properties of GUITAR [44], we use AFM to probe the surface topography of a GUITAR coating on a flat substrate. In other work not included in this dissertation, AFM is utilized to probe the surface topography of a MgZnO film [95].
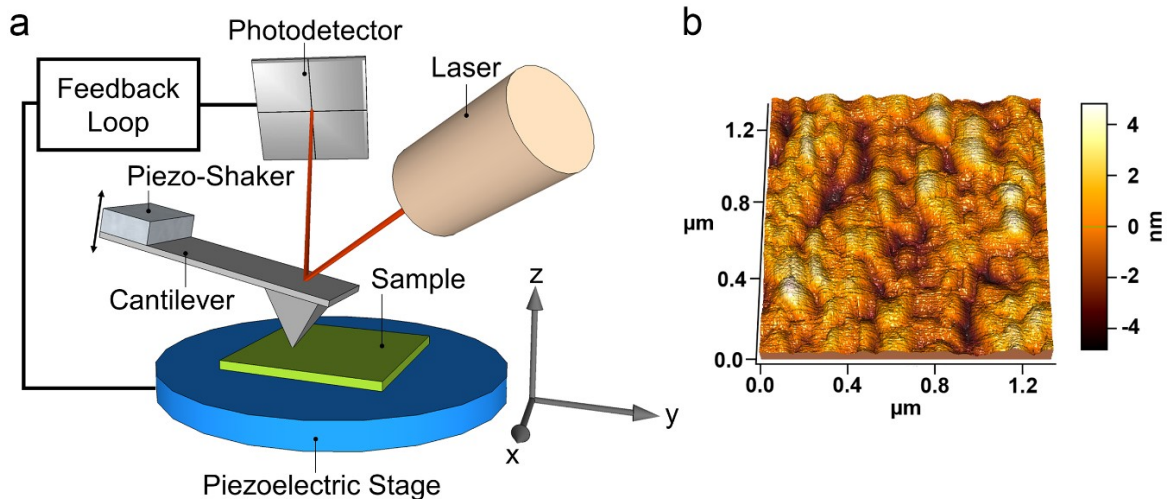
Figure 1.4 (**a**) A schematic diagram showing the working principles of AFM. (**b**) 3D AFM image showing the surface topography of a GUITAR coating on a silicon substrate.

1.3.3   Raman Spectroscopy

Raman spectroscopy is an inelastic light scattering characterization technique that provides qualitative and quantitative information about the composition of materials [96, 97]. When light with a known wavelength is irradiated on a material, an exchange of energy occurs between some of the incident photons and the molecules in the material. The resulting inelastically (Raman) scattered photons will have a higher or lower energy compared to the incident photons depending on the molecule's initial energy state. A Raman spectrum is constructed by plotting the shifts in frequencies of the incident and scattered photons. The shift in frequency, or analogously, the difference in the incident and scattered photon energies corresponds to the molecule's rotational and vibrational energy (phonon modes). These phonon modes are quantized and correspond to the specific molecular structure of the material. A Raman spectral analysis can therefore be used to identify the chemical composition of a material. A Raman spectral analysis of GUITAR was performed in chapter 3 to investigate the chemical structure of GUITAR. These results indicated that GUITAR is characteristic of nanocrystalline graphite with a low sp^3 content.

1.3.4   X-ray Diffraction

X-ray diffraction (XRD) is a non-destructive characterization technique that is used to identify and quantify crystalline structures in solid crystalline materials and powders [98]. When a monochromatic x-ray source is irradiated onto a crystalline material, constructive interference will occur when the scattered x-rays satisfy Bragg's Law, i.e., for a specific incident wavelength, crystal lattice spacing, and angle of incidence [86, 98]. Accordingly, different crystal lattice spacings will constructively interfere at specific angles. An XRD pattern is obtained by plotting the diffracted intensities as a function of the detector angle, 2θ, where each diffraction peak corresponds to the spacing of a crystal plane. Therefore, the XRD pattern gives information regarding the crystalline phases of the material, which can be identified by comparing to reference XRD patterns in databases such as the International Centre for Diffraction Data. In powder XRD, the sample ideally contains many randomly oriented crystallites to ensure that a statistically relevant number of crystalline grains are sampled. Powder XRD was utilized in chapter 4 to investigate the structure of

polycrystalline ZnO. The powder XRD pattern indicated that the polycrystalline ZnO used in the study had a hexagonal Wurtzite structure.

1.4 Nanoelectronics

The integration of nanomaterials into electronic devices is an area of intensive research due to the unique electronic and optoelectronic properties of nanomaterials and possible new functions available with nanomaterials and nanoelectronic device architectures. Typically, nanoelectronic devices are manufactured using a bottom-up approach, where device structures are synthesized via the self-assembly of atoms and molecules [99], offering precise control over device elements with near-atomic-scale-precision [100]. In contrast, a top-down approach starts with a bulk material that is patterned via chemical or mechanical processes [99]. The precision of the bottom-up approach is highly advantageous compared to a top-down approach, especially in the semiconductor industry, which is facing considerable challenges as device features are reduced to the sub-20 nm regime [101]. In this respect, nanoelectronic devices play an essential role in the continued scaling of conventional complementary metal-oxide semiconductor (CMOS) technology.

Nanoelectronic devices consisting of nanowire components are attractive because of the nanowire's atomically smooth surface, which offers ultrahigh precision of device components, exceeding the limit of conventional lithography [100]. Considerable progress has been made demonstrating the precise and controlled assembly of nanowire device components [102–105] and excellent synthetic control of semiconductor nanowires with tunable electronic properties, size, and composition [102, 103]. Nanowires can also function as both device components and interconnects in nanoelectronic devices, and can be synthesized as homogeneous semiconductors and heterostructures [102, 103, 106]. These attributes make nanowire-based electronic devices an attractive alternative to electronic devices manufactured with top-down approaches and offer a diverse range of possible device architectures and functions.

The active region in nanowire-based device architectures generally consists of nanowire arrays or a single nanowire. The exquisite demonstrated controlled assembly of nanowire components using a bottom-up approach in ordered nanowire arrays opens the door to future potential applications with highly functional integrated circuits [102, 104, 105], which will

be essential for the continued scaling of CMOS technology. Arrays of nanowires also exhibit an ultrahigh surface-area-to-volume ratio, which is attractive for sensing applications and has been shown to improve sensitivity and detectability in UV photodetectors [107]. Nanoelectronic devices with arrays of nanowires are also utilized in flexible electronics [108], gas sensing [109], biological sensing [110], and photodetection [111] applications. On the other hand, single nanowire electronic devices allow the direct observation of fundamental material properties, which are necessary to understand complicated nanoelectronic device architectures with nanowire arrays. For example, the origins of charge noise in single carbon nanotube field-effect transistors have been probed to understand sources of background noise and improve detection limits in carbon nanotube biological sensing applications [25]. A unique platform consisting of single nanowire electrodes has been studied to gain insight into the mechanism of battery capacity fading [112], a critical issue in the performance of lithium-ion batteries. Extensive research on single nanowire photovoltaics has been performed to understand the properties and potential applications of semiconductor nanowire-based photovoltaic devices [113]. Lastly, a single ZnO-coated SNS electrical device was utilized as a chemical sensor to investigate the sensor's responsivity and detectivity compared to a ZnO thin-film [58]. The experimental and numerical simulation results showed that a ZnO-coated cylindrical nanostructure exhibits lower detection limits than a ZnO thin-film—an important discovery for improving the sensitivity of a chemical sensor.

The work presented in this dissertation uses a unique approach to investigate the electrical properties of GUITAR, and the electrical and optoelectronic properties of polycrystalline ZnO by integrating single GUITAR-coated SNS and single ZnO-coated SNS core–shell structures into electronic devices to directly observe the electrical and optoelectronic properties of these two materials. Figure 1.5 shows a 3D representation of a single core–shell SNS electrical device and false-color SEM images of single GUITAR-coated SNS and single ZnO-coated SNS electrical devices. In chapter 3, we directly observe GUITAR's electrical characteristics using single GUITAR-coated SNS electrical devices. This electrical analysis showed that GUITAR has a similar resistivity and negative temperature dependence of resistivity compared to other allotropes of carbon, indicating that it is a graphitic semimetal [49]. The electrical analysis complemented other

structural and morphologic characterizations of GUITAR, which together suggest that GUITAR is a form of nanocrystalline graphite [49]. In chapter 4, we use a single polycrystalline ZnO-coated SNS device to investigate and directly observe the electronic and optoelectronic properties of polycrystalline ZnO, which reveals important information regarding the electronic and photoconductive properties of polycrystalline ZnO [56]. Understanding the fundamental material properties of GUITAR and ZnO is vital for the continued advancement of solar energy conversion, photodetection, chemical and biological sensing, and energy storage technologies.
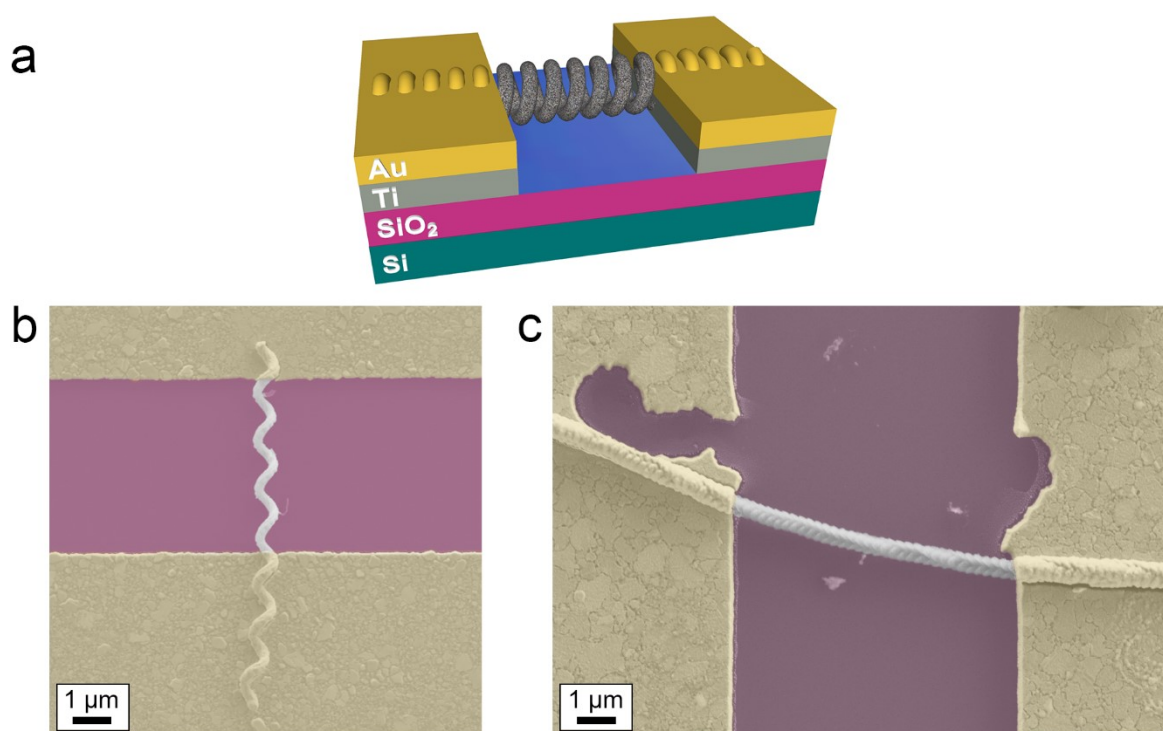
Figure 1.5 (**a**) 3D model of a single core–shell SNS electrical device. The SNS core–shell structure rests on an insulating Si/SiO$_2$ substrate. Ti and Au are thermally evaporated on each end of the core–shell structure and used as electrical contacts. False-color SEM images of (**b**) a single ZnO-coated SNS electrical device and (**c**) a single GUITAR-coated SNS electrical device.

1.5   Photoconductivity

The photoelectric effect was first observed in 1887 by Heinrich Hertz [114]; however, it was not fully explained until 1905 when Albert Einstein theorized that light is composed of individual quanta (photons) with energy equal to the frequency of the light multiplied by

Plank's constant [115]. Einstein used this principle to explain the photoelectric effect by proposing that a photon above a certain threshold frequency has enough energy to free an electron from the material and alter its electrical properties. The photoelectric effect is responsible for several phenomena, including photoconductivity, the photovoltaic effect, and the Auger and Compton effect. Photoconductivity is an internal photoelectric effect, where the conductivity of a semiconductor or insulator is increased due to the absorption of energy from photons [116]. The absorption of a photon occurs when the energy of the incident photon is greater than the energy of the material's bandgap or when the incident photon has sufficient energy to excite impurities within the bandgap. The magnitude of the photoconductivity depends on the generation of electron–hole pairs through the absorption of incident photons, their mobility, and their recombination processes. The study of these photoconductive characteristics and how they vary as a function of electric field strength, illumination intensity, temperature, and time, can reveal information about the electronic and structural properties of materials.

Low-dimensional semiconducting nanowires exhibit a variety of interesting photoconductive properties, such as a sensitivity to light polarization [117, 118], enhanced light absorption [119, 120], and high internal photoconductive gain [60, 121]. These unique characteristics, combined with the controllability of nanowire assemblies to create functional and complex device architectures, make semiconducting nanowires attractive candidates for optoelectronic applications in photodetection [60, 61, 74], solar energy conversion [70, 113, 119, 122], and light emitting diodes [65, 123]. Semiconductor nanowires have a high surface-area-to-volume ratio and, consequently, are sensitive to surface effects. The very high density of surface states in a semiconductor nanowire results in a surface depletion region which physically separates electrons and holes and can lead to enhanced carrier lifetimes [124–129], photodesorption effects [73, 125, 130], and high photoconductive gains [60, 121]. Studying these and other photoconductive properties can reveal important information about a material's carrier mobilities, carrier lifetimes, and density of localized electronic states.

The photoconductive properties of ZnO nanowires and thin-film polycrystalline ZnO are intensive areas of research due to their unique low-dimensional properties, n-type semiconducting behavior, wide 3.37 eV bandgap and large 60 meV exciton binding energy

at room temperature, high electron mobility [53], cost-effectiveness, non-toxicity, and ease of synthesis [54]. These attributes make ZnO a promising candidate for optoelectronic applications in solar energy conversion [53, 70], photodetection [60–64], and light emitting diodes [65, 66]. However, polycrystalline ZnO is a structurally disordered material and contains a variety of defects that strongly affect its photoconductive properties [56, 67, 73, 124, 128, 131–133]. For example, polycrystalline ZnO grain boundaries have been shown to contain a high density of defects [132], which are responsible for the adsorption of atmospheric oxygen molecules [134]. The adsorption of atmospheric oxygen on the surface creates a depletion region and corresponding potential gradient near the grain boundary. Following illumination and the generation of electron–hole pairs, holes can be swept to the grain boundary via the potential gradient and release adsorbed oxygen. This oxygen desorption mechanism frees electrons, which can then contribute to the conductivity. Conversely, the re-adsorption of oxygen traps electrons and decreases the conductivity. The competition between the oxygen adsorption and desorption mechanisms can lead to long electron lifetimes and a strong persistence in the photoconductivity [73, 124–129, 133, 135–141]. A persistence in the photoconductivity inhibits a quick recovery of the dark current, which is detrimental to the performance of ZnO-based photodetection applications. In addition to the oxygen adsorption and desorption mechanisms, various other photoconduction and recombination mechanisms, and the trapping of carriers in defect states can similarly affect the photoconductive properties of ZnO.

In chapter 4, we probe the photoconductive properties of a single polycrystalline ZnO-coated SNS electrical device by studying the resulting photocurrent rise and decay behavior from near-UV (405 nm) and sub-bandgap (532 and 633 nm) excitation sources. Additionally, we investigate the excitation intensity dependence of the saturation photocurrent for each excitation source. The results from this study revealed important information regarding the photocurrent generation and recombination mechanisms, defect density of states, and the trapping of carriers in ZnO. Understanding these fundamental photoconductive properties of ZnO is essential to understand and construct complex ZnO-based device architectures for solar energy conversion and photodetection applications.

1.6   Dissertation Overview

In chapter 1, we begin with an introduction to the fields of nanoscience and nanotechnology, and review and discuss the motivations for studying nanomaterials and nanocomposites. We give brief introductions to some of the characterization techniques and tools that were utilized in this dissertation. Motivations for characterizing the electrical and optoelectronic properties of GUITAR and ZnO are presented.

In chapter 2, we study the initial formation and growth dynamics of SNSs, the core material that was used as an insulating support for the electrical and morphological characterization of GUITAR, and the electrical and optoelectronic characterization of polycrystalline ZnO. We find that the helical morphology of a SNS is due to the varying growth rates of the individual silica nanowires, which create an asymmetry in the interfacial surface tension and a corresponding variable work of adhesion on the outer boundary of the catalyst–nanowires interface.

In chapter 3, we coat SNSs with a novel conductive carbon, GUITAR, to investigate its structural, morphological, and electronic properties. SEM, TEM, and AFM images fully reveal GUITAR's morphology and indicate that a GUITAR nano-thin film coating on a SNS is comprised of an agglomeration of carbon hemispheres that are formed by the accretion of small graphitic flakes. A Raman spectroscopic analysis and the electrical characterization of 11 single GUITAR-coated SNS electrical devices indicate that GUITAR is a form of nanocrystalline graphite with a low sp^3 content.

In chapter 4, we investigate the optoelectronic properties of a polycrystalline ZnO nano-thin film coating on a SNS. We study the near-UV (405 nm) and sub-bandgap (532 and 633 nm) photocurrent response of a single polycrystalline ZnO-coated SNS electrical device. We find that the photocurrent responses to these excitation sources depend on the energy of the excitation source, the depths of the native point defect levels within ZnO, and the trapping of electrons and holes. We also present a phenomenological model to explain the observed sub-linearity and the breaks in the slopes of the saturation photocurrent versus excitation intensity profile for each excitation source.

We conclude with chapter 5 and provide a summary and conclusion of the dissertation. We also offer suggestions for improvements and future directions for the work presented in this dissertation.

References

1. Kulkarni, S.K. Applications. In *Nanotechnology: Principles and Practices*; Kulkarni, S.K., Ed.; Springer International Publishing: Cham, Switzerland, 2015; pp. 317–348; ISBN 978-3-319-09171-6.

2. Taniguchi, N. On the Basic concept of Nanotechnology. In Proceedings of the International Conference on Production Engineering; Tokyo, Japan, 1974; pp. 18–23.

3. Goddard, W.A.; Brenner, D.; Lyshevski, S.; Iafrate, G.J. *Handbook of nanoscience, engineering, and technology*; 3rd ed.; CRC Press: Boca Raton, FL, USA, 2012; ISBN 978-1-4398-6015-1.

4. Eigler, D.M.; Schweizer, E.K. Positioning single atoms with a scanning tunnelling microscope. *Nature* **1990**, *344*, 524–526.

5. Celotta, R.J.; Balakirsky, S.B.; Fein, A.P.; Hess, F.M.; Rutter, G.M.; Stroscio, J.A. Invited Article: Autonomous assembly of atomically perfect nanostructures using a scanning tunneling microscope. *Review of Scientific Instruments* **2014**, *85*, 121301.

6. Thompson, S.; Packan, P.; Bohr, M. MOS scaling: Transistor challenges for the 21st century. *Intel Technology Journal* **1998**, *Q3 '98*, 1–19.

7. Lu, W.; Lee, Y.; Murdzek, J.; Gertsch, J.; Vardi, A.; Kong, L.; George, S.M.; del Alamo, J.A. First Transistor Demonstration of Thermal Atomic Layer Etching: InGaAs FinFETs with sub-5 nm Fin-width Featuring in situ ALE-ALD. In Proceedings of the 2018 IEEE International Electron Devices Meeting (IEDM); IEEE: San Francisco, CA, USA, 2018; p. 39.1.1-39.1.4.

8. Liu, G.; Hirtz, M.; Fuchs, H.; Zheng, Z. Development of Dip-Pen Nanolithography (DPN) and Its Derivatives. *Small* **2019**, *15*, 1900564.

9. Kroto, H.W.; Heath, J.R.; O'Brien, S.C.; Curl, R.F.; Smalley, R.E. C60: Buckminsterfullerene. *Nature* **1985**, *318*, 162–163.

10. Iijima, S. Helical microtubules of graphitic carbon. *Nature* **1991**, *354*, 56–58.

11. Siegel, R.W. Synthesis and Processing of Nanostructured Materials. In *Mechanical Properties and Deformation Behavior of Materials Having Ultra-Fine Microstructures*; Nastasi, M., Parkin, D.M., Gleiter, H., Eds.; Springer Netherlands: Dordrecht, Netherlands, 1993; pp. 509–538; ISBN 978-94-010-4775-3.

12. Dürkop, T.; Getty, S.A.; Cobas, E.; Fuhrer, M.S. Extraordinary Mobility in Semiconducting Carbon Nanotubes. *Nano Letters* **2004**, *4*, 35–39.

13. Bolotin, K.I.; Sikes, K.J.; Jiang, Z.; Klima, M.; Fudenberg, G.; Hone, J.; Kim, P.; Stormer, H.L. Ultrahigh electron mobility in suspended graphene. *Solid State Communications* **2008**, *146*, 351–355.

14. Balandin, A.A.; Ghosh, S.; Bao, W.; Calizo, I.; Teweldebrhan, D.; Miao, F.; Lau, C.N. Superior Thermal Conductivity of Single-Layer Graphene. *Nano Letters* **2008**, *8*, 902–907.

15. Berber, S.; Kwon, Y.-K.; Tománek, D. Unusually High Thermal Conductivity of Carbon Nanotubes. *Physical Review Letters* **2000**, *84*, 4613–4616.

16. Treacy, M.M.J.; Ebbesen, T.W.; Gibson, J.M. Exceptionally high Young's modulus observed for individual carbon nanotubes. *Nature* **1996**, *381*, 678–680.

17. Lee, C.; Wei, X.; Kysar, J.W.; Hone, J. Measurement of the Elastic Properties and Intrinsic Strength of Monolayer Graphene. *Science* **2008**, *321*, 385–388.

18. McAllister, M.J.; Li, J.-L.; Adamson, D.H.; Schniepp, H.C.; Abdala, A.A.; Liu, J.; Herrera-Alonso, M.; Milius, D.L.; Car, R.; Prud'homme, R.K.; et al. Single Sheet Functionalized Graphene by Oxidation and Thermal Expansion of Graphite. *Chemistry of Materials* **2007**, *19*, 4396–4404.

19. Peigney, A.; Laurent, Ch.; Flahaut, E.; Bacsa, R.R.; Rousset, A. Specific surface area of carbon nanotubes and bundles of carbon nanotubes. *Carbon* **2001**, *39*, 507–514.

20. Wang, L.; Liu, H.; Konik, R.M.; Misewich, J.A.; Wong, S.S. Carbon nanotube-based heterostructures for solar energy applications. *Chemical Society Reviews* **2013**, *42*, 8134.

21. Hu, Y.H.; Wang, H.; Hu, B. Thinnest Two-Dimensional Nanomaterial-Graphene for Solar Energy. *ChemSusChem* **2010**, *3*, 782–796.

22. Xia, F.; Mueller, T.; Lin, Y.; Valdes-Garcia, A.; Avouris, P. Ultrafast graphene photodetector. *Nature Nanotechnology* **2009**, *4*, 839–843.

23. Avouris, P.; Freitag, M.; Perebeinos, V. Carbon-nanotube photonics and optoelectronics. *Nature Photonics* **2008**, *2*, 341–350.

24. Saltzgaber, G.; Wojcik, P.; Sharf, T.; Leyden, M.R.; Wardini, J.L.; Heist, C.A.; Adenuga, A.A.; Remcho, V.T.; Minot, E.D. Scalable graphene field-effect sensors for specific protein detection. *Nanotechnology* **2013**, *24*, 355502.

25. Sharf, T.; Kevek, J.W.; DeBorde, T.; Wardini, J.L.; Minot, E.D. Origins of Charge Noise in Carbon Nanotube Field-Effect Transistor Biosensors. *Nano Letters* **2012**, *12*, 6380–6384.

26. Surwade, S.P.; Smirnov, S.N.; Vlassiouk, I.V.; Unocic, R.R.; Veith, G.M.; Dai, S.; Mahurin, S.M. Water desalination using nanoporous single-layer graphene. *Nature Nanotechnology* **2015**, *10*, 459–464.

27. Yang, H.Y.; Han, Z.J.; Yu, S.F.; Pey, K.L.; Ostrikov, K.; Karnik, R. Carbon nanotube membranes with ultrahigh specific adsorption capacity for water desalination and purification. *Nature Communications* **2013**, *4*, 2220.

28. Kim, J.H.; Hwang, J.-Y.; Hwang, H.R.; Kim, H.S.; Lee, J.H.; Seo, J.-W.; Shin, U.S.; Lee, S.-H. Simple and cost-effective method of highly conductive and elastic carbon nanotube/polydimethylsiloxane composite for wearable electronics. *Scientific Reports* **2018**, *8*, 1375.

29. Kang, M.; Kim, J.; Jang, B.; Chae, Y.; Kim, J.-H.; Ahn, J.-H. Graphene-Based Three-Dimensional Capacitive Touch Sensor for Wearable Electronics. *ACS Nano* **2017**, *11*, 7950–7957.

30. Hu, S.; Rajamani, R.; Yu, X. Flexible solid-state paper based carbon nanotube supercapacitor. *Applied Physics Letters* **2012**, *100*, 104103.

31. Wang, Y.; Shi, Z.; Huang, Y.; Ma, Y.; Wang, C.; Chen, M.; Chen, Y. Supercapacitor Devices Based on Graphene Materials. *The Journal of Physical Chemistry C* **2009**, *113*, 13103–13107.

32. Pumera, M. Graphene-based nanomaterials for energy storage. *Energy & Environmental Science* **2011**, *4*, 668–674.

33. Cao, Z.; Wei, B. (B. Q.) A perspective: carbon nanotube macro-films for energy storage. *Energy & Environmental Science* **2013**, *6*, 3183–3201.

34. Ferrari, A.C.; Robertson, J. Interpretation of Raman spectra of disordered and amorphous carbon. *Physical review B* **2000**, *61*, 14095.

35. Ho, M.P.; Lau, A.K.-T. Amorphous carbon nanocomposites. In *Fillers and Reinforcements for Advanced Nanocomposites*; Woodhead Publishing: Cambridge, England, 2015; pp. 309–328; ISBN 978-0-08-100079-3.

36. da Silva, D.S.; Côrtes, A.D.S.; Oliveira, M.H.; Motta, E.F.; Viana, G.A.; Mei, P.R.; Marques, F.C. Application of amorphous carbon based materials as antireflective coatings on crystalline silicon solar cells. *Journal of Applied Physics* **2011**, *110*, 043510.

37. Kumar, V.; Bergman, A.A.; Gorokhovsky, A.A.; Zaitsev, A.M. Formation of carbon nanofilms on diamond for all-carbon based temperature and chemical sensor application. *Carbon* **2011**, *49*, 1385–1394.

38. Krivchenko, V.A.; Pilevsky, A.A.; Rakhimov, A.T.; Seleznev, B.V.; Suetin, N.V.; Timofeyev, M.A.; Bespalov, A.V.; Golikova, O.L. Nanocrystalline graphite: Promising material for high current field emission cathodes. *Journal of Applied Physics* **2010**, *107*, 014315.

39. Barranco, V.; Lillo-Rodenas, M.A.; Linares-Solano, A.; Oya, A.; Pico, F.; Ibañez, J.; Agullo-Rueda, F.; Amarilla, J.M.; Rojo, J.M. Amorphous Carbon Nanofibers and Their Activated Carbon Nanofibers as Supercapacitor Electrodes. *The Journal of Physical Chemistry C* **2010**, *114*, 10302–10307.

40. Yi, P.; Peng, L.; Feng, L.; Gan, P.; Lai, X. Performance of a proton exchange membrane fuel cell stack using conductive amorphous carbon-coated 304 stainless steel bipolar plates. *Journal of Power Sources* **2010**, *195*, 7061–7066.

41. Kabir, H.; Gyan, I.O.; Francis Cheng, I. Electrochemical modification of a pyrolytic graphite sheet for improved negative electrode performance in the vanadium redox flow battery. *Journal of Power Sources* **2017**, *342*, 31–37.

42. Li, Y.; Mu, L.; Hu, Y.-S.; Li, H.; Chen, L.; Huang, X. Pitch-derived amorphous carbon as high performance anode for sodium-ion batteries. *Energy Storage Materials* **2016**, *2*, 139–145.

43. Gyan, I.O.; Cheng, I.F. Electrochemical study of biologically relevant molecules at electrodes constructed from GUITAR, a new carbon allotrope. *Microchemical Journal* **2015**, *122*, 39–44.

44. Gyan, I.O.; Wojcik, P.M.; Aston, D.E.; McIlroy, D.N.; Cheng, I.F. A Study of the Electrochemical Properties of a New Graphitic Material: GUITAR. *ChemElectroChem* **2015**, *2*, 700–706.

45. Cheng, I.F.; Xie, Y.; Gyan, I.O.; Nicholas, N.W. Highest measured anodic stability in aqueous solutions: graphenic electrodes from the thermolyzed asphalt reaction. *RSC Advances* **2013**, *3*, 2379.

46. Kabir, H.; Zhu, H.; May, J.; Hamal, K.; Kan, Y.; Williams, T.; Echeverria, E.; McIlroy, D.N.; Estrada, D.; Davis, P.H.; et al. The sp2-sp3 carbon hybridization content of nanocrystalline graphite from pyrolyzed vegetable oil, comparison of electrochemistry and physical properties with other carbon forms and allotropes. *Carbon* **2019**, *144*, 831–840.

47. Cheng, I.F.; Xie, Y.; Allen Gonzales, R.; Brejna, P.R.; Sundararajan, J.P.; Fouetio Kengne, B.A.; Eric Aston, D.; McIlroy, D.N.; Foutch, J.D.; Griffiths, P.R. Synthesis of graphene paper from pyrolyzed asphalt. *Carbon* **2011**, *49*, 2852–2861.

48. Villarreal, C.C.; Pham, T.; Ramnani, P.; Mulchandani, A. Carbon allotropes as sensors for environmental monitoring. *Current Opinion in Electrochemistry* **2017**, *3*, 106–113.

49. Wojcik, P.M.; Rajabi, N.; Zhu, H.; Estrada, D.; Davis, P.H.; Pandhi, T.; Cheng, I.F.; McIlroy, D.N. Utilizing a Single Silica Nanospring as an Insulating Support to Characterize the Electrical Transport and Morphology of Nanocrystalline Graphite. *Materials* **2019**, *12*, 3794.

50. Kabir, H.; Gyan, I.; Foutch, J.; Zhu, H.; Cheng, I. Application of GUITAR on the Negative Electrode of the Vanadium Redox Flow Battery: Improved V3+/2+ Heterogeneous Electron Transfer with Reduced Hydrogen Gassing. *Journal of Carbon Research* **2016**, *2*, 13.

51. Le, A.T.; Ahmadipour, M.; Pung, S.-Y. A review on ZnO-based piezoelectric nanogenerators: Synthesis, characterization techniques, performance enhancement and applications. *Journal of Alloys and Compounds* **2020**, *844*, 156172.

52. Hsiao, C.-C.; Huang, K.-Y.; Hu, Y.-C. Fabrication of a ZnO Pyroelectric Sensor. *Sensors* **2008**, *8*, 185–192.

53. Tiwana, P.; Docampo, P.; Johnston, M.B.; Snaith, H.J.; Herz, L.M. Electron Mobility and Injection Dynamics in Mesoporous ZnO, SnO $_2$, and TiO $_2$ Films Used in Dye-Sensitized Solar Cells. *ACS Nano* **2011**, *5*, 5158–5166.

54. Wang, J.; Chen, R.; Xiang, L.; Komarneni, S. Synthesis, properties and applications of ZnO nanomaterials with oxygen vacancies: A review. *Ceramics International* **2018**, *44*, 7357–7377.

55. Kołodziejczak-Radzimska, A.; Jesionowski, T. Zinc Oxide—From Synthesis to Application: A Review. *Materials* **2014**, *7*, 2833–2881.

56. Wojcik, P.M.; Bastatas, L.D.; Rajabi, N.; Bakharev, P.V.; McIlroy, D.N. The effects of sub-bandgap transitions and the defect density of states on the photocurrent response of a single ZnO-coated silica nanospring. *Nanotechnology* **2021**, *32*, 035202.

57. Bakharev, P.; McIlroy, D. Signal-to-Noise Enhancement of a Nanospring Redox-Based Sensor by Lock-in Amplification. *Sensors* **2015**, *15*, 13110–13120.

58. Bakharev, P.V.; McIlroy, D.N. The effect of the periodic boundary conditions of a ZnO-coated nanospring on its surface redox-induced electrical response. *Nanotechnology* **2014**, *25*, 475501.

59. Bakharev, P.; Dobrokhotov, V.; McIlroy, D. A Method for Integrating ZnO Coated Nanosprings into a Low Cost Redox-Based Chemical Sensor and Catalytic Tool for Determining Gas Phase Reaction Kinetics. *Chemosensors* **2014**, *2*, 56–68.

60. Soci, C.; Zhang, A.; Xiang, B.; Dayeh, S.A.; Aplin, D.P.R.; Park, J.; Bao, X.Y.; Lo, Y.H.; Wang, D. ZnO Nanowire UV Photodetectors with High Internal Gain. *Nano Letters* **2007**, *7*, 1003–1009.

61. Kind, H.; Yan, H.; Messer, B.; Law, M.; Yang, P. Nanowire Ultraviolet Photodetectors and Optical Switches. *Advanced Materials* **2002**, *14*, 158–160.

62. Yuan, J.; Hu, L.; Xu, Z.; Zhang, Y.; Li, H.; Cao, X.; Liang, H.; Ruan, S.; Zeng, Y.-J. Concurrent Improvement of Photocarrier Separation and Extraction in ZnO Nanocrystal Ultraviolet Photodetectors. *The Journal of Physical Chemistry C* **2019**, *123*, 14766–14773.

63. Khokhra, R.; Bharti, B.; Lee, H.-N.; Kumar, R. Visible and UV photo-detection in ZnO nanostructured thin films via simple tuning of solution method. *Scientific Reports* **2017**, *7*, 15032.

64. Deka Boruah, B. Zinc oxide ultraviolet photodetectors: rapid progress from conventional to self-powered photodetectors. *Nanoscale Advances* **2019**, *1*, 2059–2085.

65. Liang, H.; Feng, Q.; Xia, X.; Li, R.; Guo, H.; Xu, K.; Tao, P.; Chen, Y.; Du, G. Room temperature electroluminescence from arsenic doped p-type ZnO nanowires/n-ZnO thin film homojunction light-emitting diode. *Journal of Materials Science: Materials in Electronics* **2014**, *25*, 1955–1958.

66. Son, D.I.; Kwon, B.W.; Park, D.H.; Seo, W.-S.; Yi, Y.; Angadi, B.; Lee, C.-L.; Choi, W.K. Emissive ZnO–graphene quantum dots for white-light-emitting diodes. *Nature Nanotechnology* **2012**, *7*, 465–471.

67. Bastatas, L.D.; Wagle, P.; Echeverria, E.; Slinker, J.D.; McIlroy, D.N. Electrical characterization of ZnO-coated nanospring ensemble by impedance spectroscopy: probing the effect of thermal annealing. *Nanotechnology* **2019**, *30*, 234006.

68. Bora, T.; Zoepfl, D.; Dutta, J. Importance of Plasmonic Heating on Visible Light Driven Photocatalysis of Gold Nanoparticle Decorated Zinc Oxide Nanorods. *Scientific Reports* **2016**, *6*, 26913.

69. Cammi, D.; Zimmermann, K.; Gorny, R.; Vogt, A.; Dissinger, F.; Gad, A.; Markiewcz, N.; Waag, A.; Prades, J.D.; Ronning, C.; et al. Enhancement of the Sub-Band-Gap Photoconductivity in ZnO Nanowires through Surface Functionalization with Carbon Nanodots. *The Journal of Physical Chemistry C* **2018**, *122*, 1852–1859.

70. Chou, J.-C.; Ko, C.-C.; Kuo, P.-Y.; Lai, C.-H.; Nien, Y.-H.; Chang, J.-X. Fabrication of Dye-Sensitized Solar Cells Using Zinc Oxide Nanorod-Modified Titanium Dioxide Photoanode. *IEEE Transactions on Nanotechnology* **2019**, *18*, 553–561.

71. Tripathy, N.; Kim, D.-H. Metal oxide modified ZnO nanomaterials for biosensor applications. *Nano Convergence* **2018**, *5*, 27.

72. Ditshego, N.M.J. ZnO Nanowire Field Effect Transistor for Biosensing: A Review. *Journal of Nano Research* **2019**, *60*, 94–112.

73. Liu, Y.; Zhang, Z.; Xu, H.; Zhang, L.; Wang, Z.; Li, W.; Ding, L.; Hu, Y.; Gao, M.; Li, Q.; et al. Visible Light Response of Unintentionally Doped ZnO Nanowire Field Effect Transistors. *The Journal of Physical Chemistry C* **2009**, *113*, 16796–16801.

74. Kim, W.; Chu, K.S. ZnO nanowire field-effect transistor as a UV photodetector; optimization for maximum sensitivity. *Physica Status Solidi (A)* **2009**, *206*, 179–182.

75. Bastatas, L.; Wagle, P.; Echeverria, E.; Austin, A.; McIlroy, D. The Effect of UV Illumination on the Room Temperature Detection of Vaporized Ammonium Nitrate by a ZnO Coated Nanospring-Based Sensor. *Materials* **2019**, *12*, 302.

76. Dobrokhotov, V.; Oakes, L.; Sowell, D.; Larin, A.; Hall, J.; Kengne, A.; Bakharev, P.; Corti, G.; Cantrell, T.; Prakash, T.; et al. ZnO coated nanospring-based chemiresistors. *Journal of Applied Physics* **2012**, *111*, 044311.

77. Sahay, R.; Reddy, V.J.; Ramakrishna, S. Synthesis and applications of multifunctional composite nanomaterials. *International Journal of Mechanical and Materials Engineering* **2014**, *9*, 25.

78. Ajayan, P.M.; Schadler, L.S.; Braun, P.V. *Nanocomposite Science and Technology*; John Wiley & Sons: Hoboken, NJ, USA, 2006; ISBN 978-3-527-60517-0.

79. Luo, G.; Fouetio Kengne, B.-A.; McIlroy, D.N.; McDonald, A.G. A novel nano fischer-tropsch catalyst for the production of hydrocarbons. *Environmental Progress & Sustainable Energy* **2014**, *33*, 693–698.

80. Corti, G.; Zhan, Y.; Wang, L.; Hare, B.; Cantrell, T.; Ii, M.B.; Prakash, T.; Ytreberg, F.M.; Miller, M.A.; McIlroy, D.N. The effects of nanoscale geometry and spillover on room temperature storage of hydrogen on silica nanosprings. *Journal of Physics D: Applied Physics* **2013**, *46*, 505307.

81. Schilke, K.F.; Wilson, K.L.; Cantrell, T.; Corti, G.; McIlroy, D.N.; Kelly, C. A novel enzymatic microreactor with Aspergillus oryzae β-galactosidase immobilized on silicon dioxide nanosprings. *Biotechnology Progress* **2010**, *26*, 1597–1605.

82. Yukta P. Timalsina; Josh R. Branen; Jeremy Eilers; Blaise Alexis Fouetio Kengne; Giancarlo Corti; D. Eric Aston; David N. McIlroy The Role of Biofunctionalized Silica Nanospring Surface for Selective Biosensing. *Advances in Biosensors and Bioelectronics* **2012**, *1*, 1–10.

83. Kalambate, P.K.; Dhanjai; Huang, Z.; Li, Y.; Shen, Y.; Xie, M.; Huang, Y.; Srivastava, A.K. Core-shell nanomaterials based sensing devices: A review. *TrAC Trends in Analytical Chemistry* **2019**, *115*, 147–161.

84. Hass, J.L.; Garrison, E.M.; Wicher, S.A.; Knapp, B.; Bridges, N.; McIlroy, D.N.; Arrizabalaga, G. Synthetic osteogenic extracellular matrix formed by coated silicon dioxide nanosprings. *Journal of Nanobiotechnology* **2012**, *10*, 1–12.

85. Quinn, C.; Steciak, J.; Budwig, R.; McIlroy, D.; Beyerlein, S. Measuring the Temperature Coefficient of Resistance for Nanospring Combustion Catalysts. In Proceedings of the ASME 2013 International Mechanical Engineering Congress and Exposition; San Diego, CA, USA, 2013.

86. Kalantar-zadeh, K.; Fry, B. Characterization Techniques for Nanomaterials. In *Nanotechnology-Enabled Sensors*; Springer: Boston, MA, USA, 2008; pp. 211–281; ISBN 978-0-387-68023-1.

87. Kumar, P.S.; Pavithra, K.G.; Naushad, Mu. Characterization techniques for nanomaterials. In *Nanomaterials for Solar Cell Applications*; Elsevier: Amsterdam, Netherlands, 2019; pp. 97–124; ISBN 978-0-12-813337-8.

88. Salame, P.H.; Pawade, V.B.; Bhanvase, B.A. Characterization Tools and Techniques for Nanomaterials. In *Nanomaterials for Green Energy*; Elsevier: Amsterdam, Netherlands, 2018; pp. 83–111; ISBN 978-0-12-813731-4.

89. Srivastava, R. Synthesis and Characterization Techniques of Nanomaterials. *International Journal of Green Nanotechnology* **2012**, *4*, 17–27.

90. Sadik, O.A.; Du, N.; Kariuki, V.; Okello, V.; Bushlyar, V. Current and Emerging Technologies for the Characterization of Nanomaterials. *ACS Sustainable Chemistry & Engineering* **2014**, *2*, 1707–1716.

91. Murr, L.E. Classifications and Structures of Nanomaterials. In *Handbook of Materials Structures, Properties, Processing and Performance*; Springer International Publishing: Cham, Switzerland, 2015; pp. 719–746; ISBN 978-3-319-01814-0.

92. Binnig, G.; Rohrer, H. Scanning tunneling microscopy. *Surface Science* **1983**, *126*, 236–244.

93. Binnig, G.; Quate, C.F.; Gerber, Ch. Atomic Force Microscope. *Physical Review Letters* **1986**, *56*, 930–933.

94. Nasrollahzadeh, M.; Sajadi, S.M.; Sajjadi, M.; Issaabadi, Z. An Introduction to Nanotechnology. In *Interface Science and Technology*; Academic Press: Cambridge, MA, USA, 2019; Vol. 28, pp. 1–27; ISBN 978-0-12-813586-0.

95. Thapa, D.; Huso, J.; Miklos, K.; Wojcik, P.M.; McIlroy, D.N.; Morrison, J.L.; Corolewski, C.; McCluskey, M.D.; Williams, T.J.; Grant Norton, M.; et al. UV-luminescent MgZnO semiconductor alloys: nanostructure and optical properties. *Journal of Materials Science: Materials in Electronics* **2017**, *28*, 2511–2520.

96. Colthup, N. *Introduction to Infrared and Raman Spectroscopy*; Academic Press: Cambridge, MA, USA, 2012; ISBN 978-0-323-16160-2.

97. Bumbrah, G.S.; Sharma, R.M. Raman spectroscopy – Basic principle, instrumentation and selected applications for the characterization of drugs of abuse. *Egyptian Journal of Forensic Sciences* **2016**, *6*, 209–215.

98. Warren, B.E. *X-Ray Diffraction*; Dover Publications, Inc.: Mineola, NY, USA, 1990; ISBN 978-0-486-14161-9.

99. Mijatovic, D.; Eijkel, J.C.T.; van den Berg, A. Technologies for nanofluidic systems: top-down vs. bottom-up—a review. *Lab on a Chip* **2005**, *5*, 492.

100. McEuen, P.L.; Fuhrer, M.S.; Hongkun Park Single-walled carbon nanotube electronics. *IEEE Transactions on Nanotechnology* **2002**, *1*, 78–85.

101. Vaidyanathan, K.; Zhu, Q.; Liebmann, L.; Lai, K.; Wu, S.; Liu, R.; Liu, Y.; Strojwas, A.; Pileggi, L. Exploiting sub-20-nm complementary metal-oxide semiconductor technology challenges to design affordable systems-on-chip. *Journal of Micro/Nanolithography, MEMS, and MOEMS* **2014**, *14*, 011007.

102. Jia, C.; Lin, Z.; Huang, Y.; Duan, X. Nanowire Electronics: From Nanoscale to Macroscale. *Chemical Reviews* **2019**, *119*, 9074–9135.

103. Wang, F.; Dong, A.; Buhro, W.E. Solution–Liquid–Solid Synthesis, Properties, and Applications of One-Dimensional Colloidal Semiconductor Nanorods and Nanowires. *Chemical Reviews* **2016**, *116*, 10888–10933.

104. Lu, W.; Lieber, C.M. Nanoelectronics from the bottom up. *Nature Materials* **2007**, *6*, 841–850.

105. Che, Y.; Chen, H.; Gui, H.; Liu, J.; Liu, B.; Zhou, C. Review of carbon nanotube nanoelectronics and macroelectronics. *Semiconductor Science and Technology* **2014**, *29*, 073001.

106. Li, A.; Zou, J.; Han, X. Growth of III-V semiconductor nanowires and their heterostructures. *Science China Materials* **2016**, *59*, 51–91.

107. Alenezi, M.R.; Henley, S.J.; Silva, S.R.P. On-chip Fabrication of High Performance Nanostructured ZnO UV Detectors. *Scientific Reports* **2015**, *5*, 8516.

108. Wang, J.-L.; Hassan, M.; Liu, J.-W.; Yu, S.-H. Nanowire Assemblies for Flexible Electronic Devices: Recent Advances and Perspectives. *Advanced Materials* **2018**, *30*, 1803430.

109. Tiwale, N. Zinc oxide nanowire gas sensors: fabrication, functionalisation and devices. *Materials Science and Technology* **2015**, *31*, 1681–1697.

110. Neveling, D.P.; van den Heever, T.S.; Perold, W.J.; Dicks, L.M.T. A nanoforce ZnO nanowire-array biosensor for the detection and quantification of immunoglobulins. *Sensors and Actuators B: Chemical* **2014**, *203*, 102–110.

111. He, Y.; Zhang, W.; Zhang, S.; Kang, X.; Peng, W.; Xu, Y. Study of the photoconductive ZnO UV detector based on the electrically floated nanowire array. *Sensors and Actuators A: Physical* **2012**, *181*, 6–12.

112. Mai, L.; Dong, Y.; Xu, L.; Han, C. Single Nanowire Electrochemical Devices. *Nano Letters* **2010**, *10*, 4273–4278.

113. Tian, B.; Kempa, T.J.; Lieber, C.M. Single nanowire photovoltaics. *Chemical Society Reviews* **2008**, *38*, 16–24.

114. Hertz, H. Ueber einen Einfluss des ultravioletten Lichtes auf die electrische Entladung. *Annalen der Physik* **1887**, *267*, 983–1000.

115. Einstein, A. A Heuristic Point of View About the Generation and Transformation of Light. *Annalen der Physik.* **1905**, *17*, 132.

116. Bube, R.H. *Photoconductivity of solids*; R.E. Krieger Pub. Co: Huntington, NY, USA, 1978; ISBN 978-0-88275-660-8.

117. Yu, Y.; Protasenko, V.; Jena, D.; Xing, H. (Grace); Kuno, M. Photocurrent Polarization Anisotropy of Randomly Oriented Nanowire Networks. *Nano Letters* **2008**, *8*, 1352–1357.

118. Wang, J. Highly Polarized Photoluminescence and Photodetection from Single Indium Phosphide Nanowires. *Science* **2001**, *293*, 1455–1457.

119. Muskens, O.L.; Rivas, J.G.; Algra, R.E.; Bakkers, E.P.A.M.; Lagendijk, A. Design of Light Scattering in Nanowire Materials for Photovoltaic Applications. *Nano Letters* **2008**, *8*, 2638–2642.

120. Zhang, A.; You, S.; Soci, C.; Liu, Y.; Wang, D.; Lo, Y.-H. Silicon nanowire detectors showing phototransistive gain. *Applied Physics Letters* **2008**, *93*, 121110.

121. Prades, J.D.; Jimenez-Diaz, R.; Hernandez-Ramirez, F.; Fernandez-Romero, L.; Andreu, T.; Cirera, A.; Romano-Rodriguez, A.; Cornet, A.; Morante, J.R.; Barth, S.; et al. Toward a Systematic Understanding of Photodetectors Based on Individual Metal Oxide Nanowires. *The Journal of Physical Chemistry C* **2008**, *112*, 14639–14644.

122. Kelzenberg, M.D.; Turner-Evans, D.B.; Kayes, B.M.; Filler, M.A.; Putnam, M.C.; Lewis, N.S.; Atwater, H.A. Photovoltaic Measurements in Single-Nanowire Silicon Solar Cells. *Nano Letters* **2008**, *8*, 710–714.

123. Alvi, N.H.; ul Hasan, K.; Nur, O.; Willander, M. The origin of the red emission in n-ZnO nanotubes/p-GaN white light emitting diodes. *Nanoscale Research Letters* **2011**, *6*, 130.

124. Moazzami, K.; Murphy, T.E.; Phillips, J.D.; Cheung, M.C.-K.; Cartwright, A.N. Sub-bandgap photoconductivity in ZnO epilayers and extraction of trap density spectra. *Semiconductor Science and Technology* **2006**, *21*, 717–723.

125. Li, Q.H.; Gao, T.; Wang, Y.G.; Wang, T.H. Adsorption and desorption of oxygen probed from ZnO nanowire films by photocurrent measurements. *Applied Physics Letters* **2005**, *86*, 123117.

126. Reemts, J.; Kittel, A. Persistent photoconductivity in highly porous ZnO films. *Journal of Applied Physics* **2007**, *101*, 013709.

127. Bao, J.; Shalish, I.; Su, Z.; Gurwitz, R.; Capasso, F.; Wang, X.; Ren, Z. Photoinduced oxygen release and persistent photoconductivity in ZnO nanowires. *Nanoscale Research Letters* **2011**, *6*, 404.

128. Cammi, D.; Ronning, C. Persistent Photoconductivity in ZnO Nanowires in Different Atmospheres. *Advances in Condensed Matter Physics* **2014**, *2014*, 1–5.

129. Wang, Y.; Liao, Z.; She, G.; Mu, L.; Chen, D.; Shi, W. Optical modulation of persistent photoconductivity in ZnO nanowires. *Applied Physics Letters* **2011**, *98*, 203108.

130. Chen, R.-S.; Wang, W.-C.; Chan, C.-H.; Hsu, H.-P.; Tien, L.-C.; Chen, Y.-J. Photoconductivities in monocrystalline layered V2O5 nanowires grown by physical vapor deposition. *Nanoscale Research Letters* **2013**, *8*, 443.

131. Kavitha, M.K.; Jinesh, K.B.; Philip, R.; Gopinath, P.; John, H. Defect engineering in ZnO nanocones for visible photoconductivity and nonlinear absorption. *Physical Chemistry Chemical Physics* **2014**, *16*, 25093–25100.

132. Bandopadhyay, K.; Mitra, J. Spatially resolved photoresponse on individual ZnO nanorods: correlating morphology, defects and conductivity. *Scientific Reports* **2016**, *6*, 28468.

133. Prades, J.D.; Hernandez-Ramirez, F.; Jimenez-Diaz, R.; Manzanares, M.; Andreu, T.; Cirera, A.; Romano-Rodriguez, A.; Morante, J.R. The effects of electron–hole separation on the photoconductivity of individual metal oxide nanowires. *Nanotechnology* **2008**, *19*, 465501.

134. An, W.; Wu, X.; Zeng, X.C. Adsorption of O$_2$, H$_2$, CO, NH$_3$, and NO$_2$ on ZnO Nanotube: A Density Functional Theory Study. *The Journal of Physical Chemistry C* **2008**, *112*, 5747–5755.

135. Fan, Z.; Chang, P.; Lu, J.G.; Walter, E.C.; Penner, R.M.; Lin, C.; Lee, H.P. Photoluminescence and polarized photodetection of single ZnO nanowires. *Applied Physics Letters* **2004**, *85*, 6128–6130.

136. Keem, K.; Kim, H.; Kim, G.-T.; Lee, J.S.; Min, B.; Cho, K.; Sung, M.-Y.; Kim, S. Photocurrent in ZnO nanowires grown from Au electrodes. *Applied Physics Letters* **2004**, *84*, 4376–4378.

137. Moore, J.; Thompson, C. A Phenomenological Model for the Photocurrent Transient Relaxation Observed in ZnO-Based Photodetector Devices. *Sensors* **2013**, *13*, 9921–9940.

138. Covington, L.R.; Moore, J.C. Photoconductivity and transient response of Al:ZnO:Al planar structures fabricated via a thermal oxidation process. *Thin Solid Films* **2013**, *540*, 106–111.

139. Madel, M.; Huber, F.; Mueller, R.; Amann, B.; Dickel, M.; Xie, Y.; Thonke, K. Persistent photoconductivity in ZnO nanowires: Influence of oxygen and argon ambient. *Journal of Applied Physics* **2017**, *121*, 124301.

140. Collins, R.J.; Thomas, D.G. Photoconduction and Surface Effects with Zinc Oxide Crystals. *Physical Review* **1958**, *112*, 388–395.

141. Melnick, D.A. Zinc Oxide Photoconduction, an Oxygen Adsorption Process. *The Journal of Chemical Physics* **1957**, *26*, 1136–1146.

CHAPTER 2

Nucleation, Evolution, and Growth Dynamics of Amorphous Silica Nanosprings

Peter M. Wojcik, Pavel V. Bakharev, Giancarlo Corti, and David N. McIlroy

The initial phases of amorphous silica nanospring formation via a vapor–liquid–solid mechanism are reported. The low-temperature eutectic of Au–Si results in the formation of an asymmetrically-shaped catalyst at the early stages of nanospring formation. As solid silica is formed below the Au–Si catalyst, the system lowers its surface free energy and forms multiple amorphous silica nanowires beneath a common catalyst, as opposed to a single nanowire. The diameter of one of the nanowires forming the nanospring ranges between ~10 to 20 nm. The difference in growth rates of the individual nanowires creates an asymmetry in the interfacial surface tension on the boundary of the Au–Si catalyst–nanowires interface. Using Stokes' theorem, it is shown that there is a variable work of adhesion on the outer boundary of the Au–Si catalyst–nanowires interface of a nanospring, which is defined as an effective contact angle anisotropy. The anisotropic growth on the catalyst–nanowires boundary results in the nanowires coherently coiling into a single, larger, helical structure with a wire diameter of ~70–500 nm and outer diameter of ~200–1000 nm.

2.1 Author's Note

Most of the material presented in this chapter has been published in *Materials Research Express* **2017**, *4*, 015004 [1]. Additional information that does not appear in the journal publication has been included in the main body of the text to provide a more thorough examination of the topic. If the reader would like to cite the work presented in this chapter, we refer them to the published journal article. The version of the journal publication presented in this chapter corrects some minor errors present in the journal article. These amendments include:

- A correction to the units of energy presented in section 3.3 of the journal publication (section 2.4.3 in this chapter), which should be: $P\ m^3$.
- A correction to the second line of Equation 3 in the journal publication (Equation 2.3 in this chapter), which should read: $W_A = \gamma_{SV} + \gamma_{SL} - (\gamma_{SL} + \gamma_{SV} \cos \theta)$.
- A correction to the definition of the angle, θ, in section 3.5 of the journal publication (section 2.4.5 in this chapter), which should read: θ is the angle between the solid–vapor and solid–liquid interfacial surface tensions.

2.2 Introduction

Materials research over the past 20 years has led to the development of materials with dimensions in the micro- to nano-scale range with enhanced or new properties that have facilitated their use in applications such as biological sensors [2–8], drug delivery to cells and tissue [9], lithium batteries [10], supercapacitors [11, 12], solar cells [13–15], and nanoelectronic power sources [13]. One-dimensional nanostructures, typically referred to as nanowires (NWs), are a class of nanomaterials that have been shown to be an extremely versatile platform for a wide range of applications. If the NW is twisted, forming a helical structure, it is often referred to as a nanospring [16–19]. The material, mechanical, and electrical properties of nanosprings, and other helical nanostructures, have been extensively studied [16–25] and continue to be of interest.

One member of the nanospring family of nanostructures are silica nanosprings (SNSs). Single SNSs and random ensembles of SNSs, or SNS mats, have been used for a variety of applications because of their versatility as a nanoscale engineering platform and their large 330 m^2 g^{-1} specific surface area [26]. The low-temperature growth of SNSs enables them to be grown on a broad range of substrates such as silicon, silicon dioxide, copper, steel, stainless steel, glass slides, light bulbs [27], quartz, aluminum, carbon fiber, and graphite. SNS mats have been used as supports for immobilizing enzymes in microreactors [28] and functionalized with biological molecules for use as electronic biosensors [4]. The applications of SNS mats and single SNSs can be extended by coating them with semiconductors such as ZnO, TiO$_2$, and SnO$_2$. Metal-oxide/metal multilayer-coated SNSs have been shown to improve the structural and functional connection between bone and orthopedic materials [29]. ZnO-coated SNS mats and a single ZnO-coated SNS have been used as highly sensitive chemical sensors for detection of explosives vapor [27, 30–33]. Metal nanoparticle coatings of SNSs have been shown to increase the hydrogen storage capacity of SNS mats [34], enhance the response of ZnO-coated SNS chemical sensors [31], and be effective Fischer–Tropsch catalysts [26]. SNSs have also been coated with a novel conductive carbon material, GUITAR (graphite from the University of Idaho thermolyzed asphalt reaction) [35]. The combination of the SNS's high surface area and the conductive properties of GUITAR has led to their inclusion in electrodes for capacitors and desalination devices.

It is important to note that an individual SNS forms via the vapor–liquid–solid (VLS) mechanism [36] and is composed of a bundle of individual amorphous silica NWs with diameters ranging from ~10 to 20 nm, collectively coupled via a common catalyst. SNSs have previously been reported [19]; however, a detailed understanding of the mechanism(s) responsible for multiple NW nucleation from a single catalyst particle, much less their helical morphology, is still lacking. Given the technological relevance of SNSs, a detailed study of their initial phases of formation is in order. Herein, we present the results of a detailed study of SNS catalyst formation, a thermodynamic explanation of multi-NW nucleation from a single catalyst, and the SNS's subsequent helical morphology. The outcomes of this study will assist future researchers with the development of processes for producing NWs and nanosprings from other materials.

2.3 Experimental Methods

2.3.1 Gold Catalyst Deposition

The substrates used in this study were ⟨100⟩ oriented Si wafers with a 500 nm thermal oxide (Si/SiO_2) and pyrolytic carbon. The Si/SiO_2 substrates were cleaned sequentially with acetone, isopropanol, and deionized water, followed by drying with N_2 prior to sputtering and photolithography. The catalyst for SNS growth, gold, was sputtered onto the Si/SiO_2 and pyrolytic carbon substrates. Sputtering of gold was performed via argon plasma-assisted sputtering in a vacuum chamber operated at an Ar pressure of ~10 mTorr. In all the experiments, the substrates were sputtered with a ~5–10 nm thick layer of gold.

2.3.2 Photolithography

A standard photolithography process was used to create circular, rectangular, and triangular shapes of gold catalyst. The growth of SNSs from the edge of these gold catalyst shapes facilitated the imaging of the SNSs' initial stages of formation. A variety of catalyst shapes and sizes were patterned onto Si/SiO_2 substrates using a standard photolithography process. Briefly, SPR220-4.5 photoresist was patterned on the Si/SiO_2 substrate, sputtered with ~5–10 nm of gold, then sonicated in acetone to remove the photoresist. Figure 2.1 shows optical and scanning electron microscopy (SEM) images of a sample that was patterned with gold

catalyst and used to grow SNSs. The upper-left image shows the substrate (blue) with patterned gold catalyst (tan) that was used to grow SNSs. The upper-center image shows some of the gold catalyst patterns that were used to image the initial stages of SNS formation and growth. The remaining images in Figure 2.1 are SEM images showing the initial stages of SNS formation and growth.
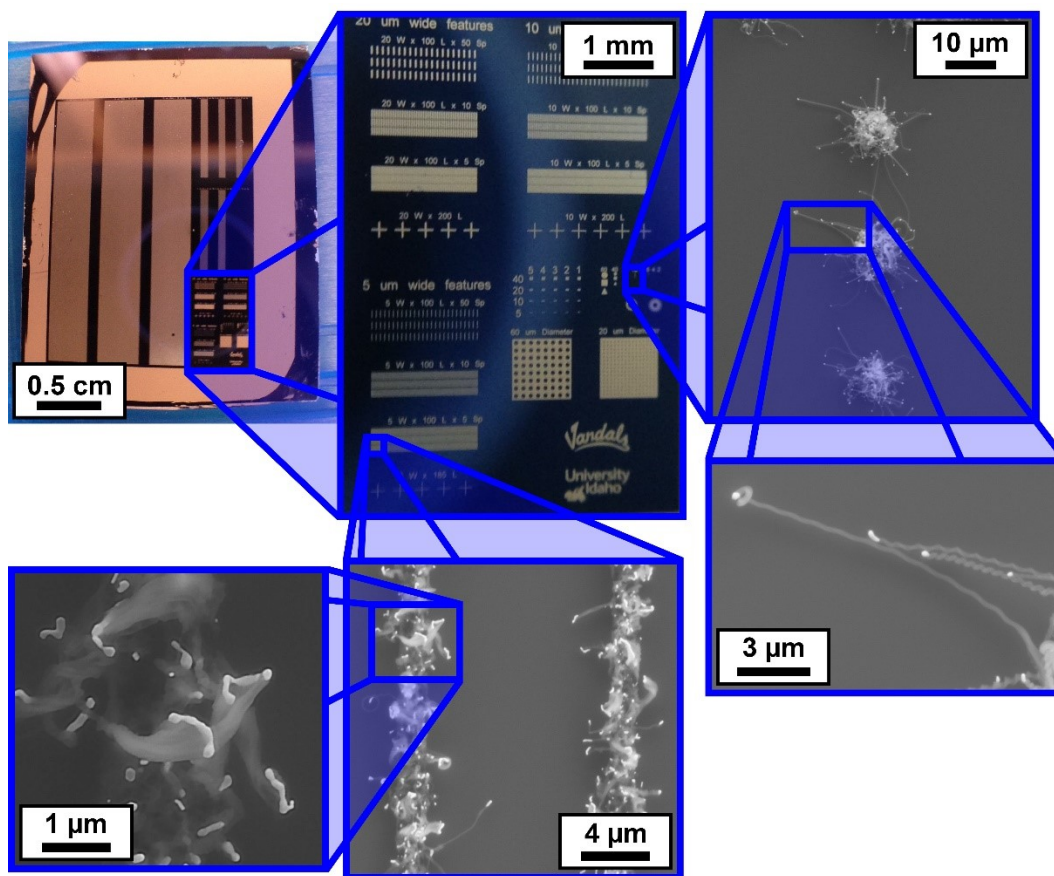
Figure 2.1 Image sequence showing optical and SEM images of the rectangular, triangular, and circular catalyst shapes used to investigate the initial stages of SNS formation.

2.3.3 Silica Nanospring Growth

Figure 2.2 is a schematic diagram of the experimental setup used for SNS growth. Gold sputtered substrates were placed into a vertically-oriented tube furnace and heated to 250 °C ± 5 °C while flowing N_2 at atmospheric pressure. Following warm-up in N_2, a proprietary Si-based precursor was introduced into the tube furnace on top of the already flowing N_2. 10 s after the addition of the Si precursor, O_2 was introduced into the tube furnace. The

temperature inside the tube furnace continued to increase after the introduction of the Si precursor and O_2, until the final set-point temperature of 350 °C ± 5 °C was reached. SNS growth begins with the introduction of O_2 and SNS growth was terminated by turning the heaters off and discontinuing the flow of the Si precursor and O_2. The SNS growth time (temperature inside the tube furnace at the termination of the growth cycle) varied from 90 s (260 °C ± 5 °C) to 10 min (350 °C ± 5 °C). The samples were taken out of the tube furnace ~3 min after termination of the growth cycle. The temperature inside the tube furnace at a location near the substrate was monitored with an Omega Model HH12 (Omega Engineering, Norwalk, CT, USA) digital thermometer. All experiments in this study were conducted at atmospheric pressure.
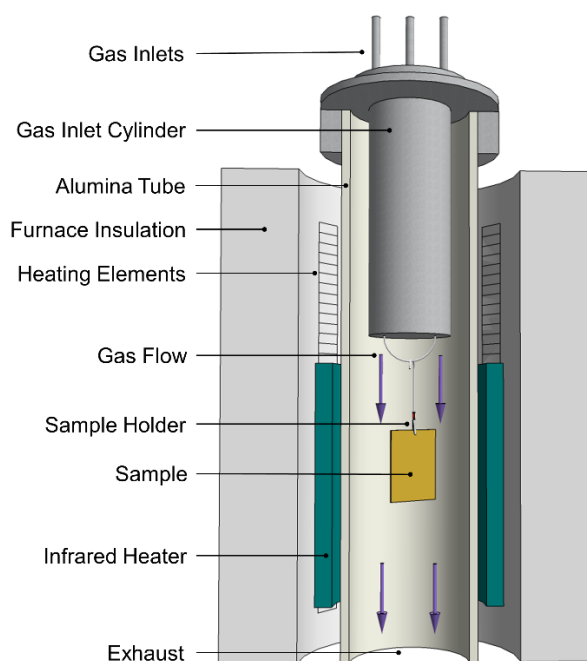
Figure 2.2 Schematic diagram of the experimental setup used for SNS growth showing a sectional view of the vertically-oriented tube furnace.

2.3.4 Microscopy Equipment

SEM images were obtained with a Zeiss Supra 35 scanning electron microscope (Zeiss, Peabody, MA, USA). Transmission electron microscopy (TEM) images were obtained with a JEOL-2010J transmission electron microscope (JEOL USA, Peabody, MA, USA) operating at 200 kV.

2.4 Results and Discussion

2.4.1 Catalyst Formation and Evolution

The catalyst is critical to VLS formation of nanostructures such as SNSs, where it is assumed that the catalyst is, or evolves into, a nanoparticle [17]. Therefore, it is important to understand the evolution of the gold film at the early stage of SNS formation. The effects of annealing on the morphology of gold films on Si/SiO$_2$ substrates at 250 °C ± 5 °C under a variety of conditions are displayed in Figure 2.3. Figure 2.3(a) is an SEM image of an as-sputtered gold film prior to annealing. The as-sputtered gold film exhibits dark regions, or crack-like voids, typical of gold sputtered on Si [37] and glass [38–40] substrates. Figure 2.3(b) is an SEM image of the same gold film shown in Figure 2.3(a) after heating to 250 °C ± 5 °C under a constant flow of N$_2$. Under these conditions, the gold film begins to diffuse and nucleate (bright regions), concomitant with the formation of large voids (dark regions), at the expense of the crack-like voids in the as-sputtered film. However, at this stage the gold film has not broken up into individual islands associated with VLS formation of nanostructures.
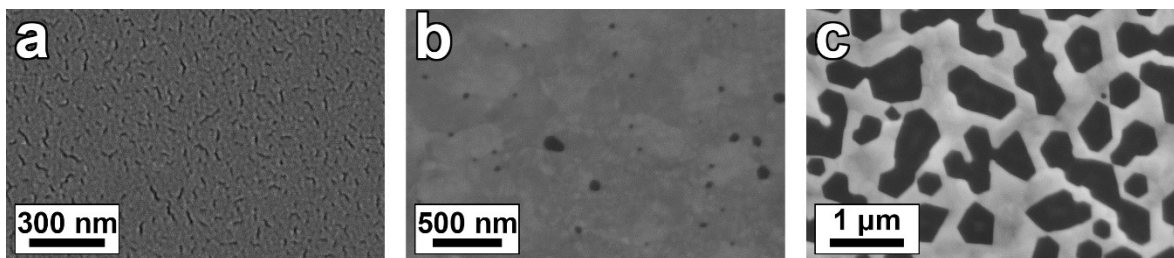
Figure 2.3 SEM images of the initial stages of diffusion and nucleation of gold films on Si/SiO$_2$ substrates. (**a**) Substrate sputtered with ~5–10 nm gold. (**b**) Gold film heated to 250 °C ± 5 °C under a constant flow of N$_2$. (**c**) Gold film heated to 250 ± 5 °C while continuously flowing N$_2$, subsequently followed by the addition of the Si precursor for 10 s. The addition of Si precursor facilitates the coalescence of the gold (white areas).

Figure 2.3(c) shows an SEM image of a gold film on a Si/SiO$_2$ substrate heated to 250 °C ± 5 °C while continuously flowing N$_2$, subsequently followed by the addition of the Si precursor for 10 s. The temperature inside the tube furnace at the termination of the 10 s exposure to Si precursor was 250 °C ± 5 °C. Under these conditions, the gold film rapidly coalesces into a network of interconnected gold islands, thereby creating large regions

devoid of gold. It is well known that Si diffuses rapidly into gold, even at room temperature [41]. In the present case, the Si precursor is absorbed by the gold to form a Au–Si alloy, which has a surface tension that favors coalescence. The faceting is a consequence of equilibration of the Au–Si alloy's surface tension with that of the substrate and the vapor. The eutectic temperature for bulk Au–Si is 363 °C at a concentration of 19% Si [42]; however, decreasing the volume of the Au–Si eutectic can lower the eutectic temperature to 260 °C, as is the case with nanometer-sized gold particles [43].

Figure 2.4 shows SEM images of a gold film on a Si/SiO$_2$ substrate heated to 250 °C ± 5 °C while continuously flowing N$_2$, subsequently followed by the addition of the Si precursor and O$_2$ for 90 s. The temperature inside the tube furnace at the termination of the 90 s growth cycle was 260 °C ± 5 °C. The slight increase in temperature and the addition of O$_2$ increases the coalescence of the Au–Si alloy. The fuzzy regions in Figure 2.4 are the very preliminary stages of SNS formation. Increased heating of the substrate while flowing N$_2$ and the Si precursor does not initiate any type of NW or nanospring growth, i.e., we are unable to create silicon NWs or silicon nanosprings while flowing N$_2$ and Si precursor in the absence of O$_2$. Therefore, the VLS process is initiated with the introduction of O$_2$. This indicates that oxidation of the Si absorbed by the catalyst is a strong driving force of SNS formation, which will be discussed in greater detail shortly.
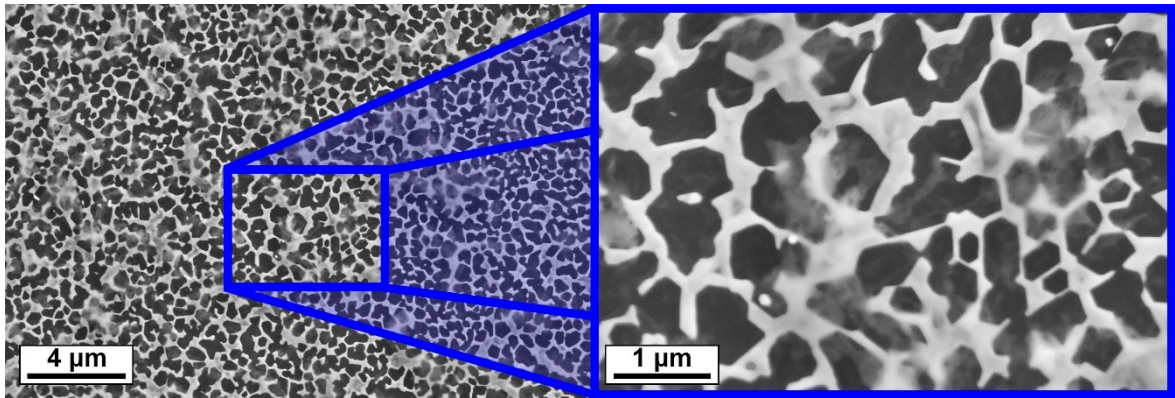
Figure 2.4 SEM images of a gold film heated to 250 °C ± 5 °C while continuously flowing N$_2$, subsequently followed by the addition of the Si precursor and O$_2$ for 90 s.

Figure 2.5 shows SEM images of a gold film on a Si/SiO$_2$ substrate heated to 250 °C ± 5 °C while continuously flowing N$_2$, subsequently followed by the addition of the

Si precursor and O_2 for 105 s. The temperature inside the tube furnace at the termination of the 105 s growth cycle was 300 °C ± 5 °C. The SEM images in Figure 2.5 were acquired at different locations on the same sample and show several stages of SNS growth. In the right-hand panels of Figure 2.5, one can see that the Au–Si catalyst tip for a single SNS (white areas) emerges from the edge of the bulk Au–Si catalyst. It is well known that Au–O interactions are weak, where diffusion of O, or O_2, through the liquid Au–Si catalyst is energetically unfavorable. Consequently, it is proposed that O_2 reacts with Si along the liquid–solid interface to form amorphous silica below the liquid Au–Si catalyst. Following the formation of an asymmetrically-shaped Au–Si catalyst, the Au–Si catalyst droplet absorbs Si precursor to the point of reaching supersaturation. As the excess Si diffuses from the catalyst, it reacts with O_2 along the liquid–solid interface to form solid silica below the Au–Si catalyst droplet.
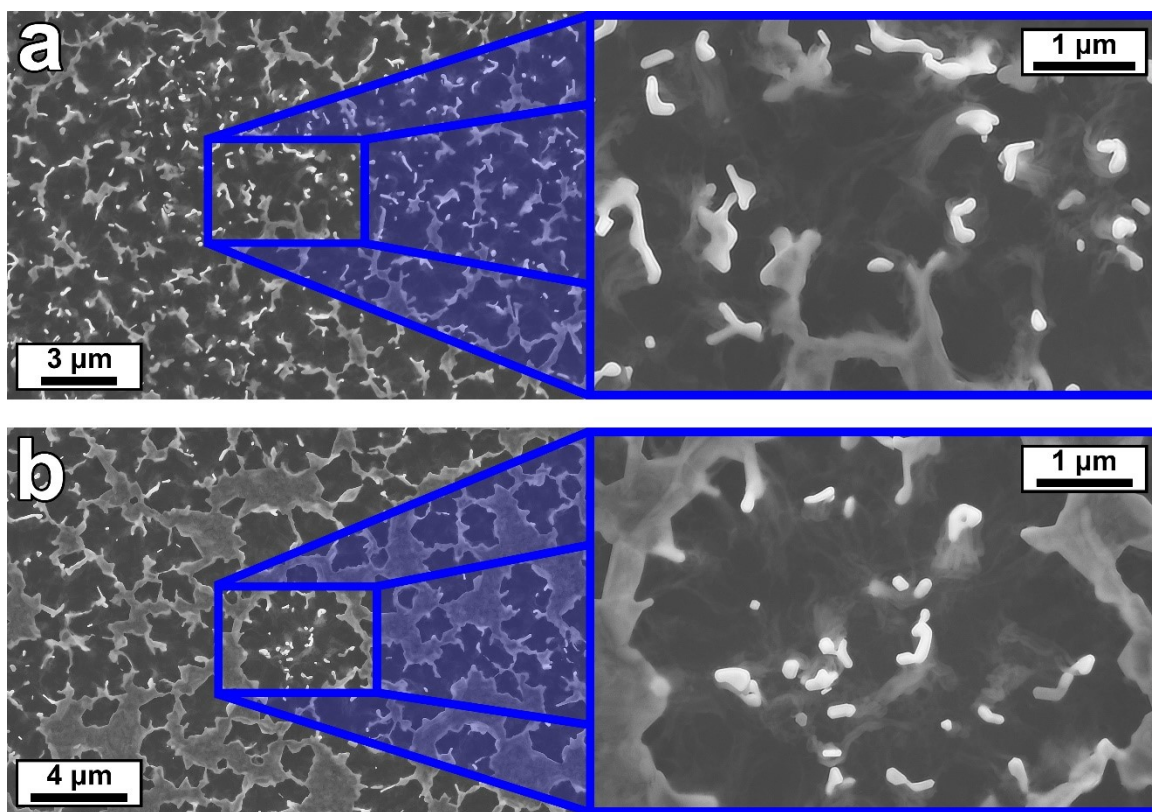
Figure 2.5 SEM images of a gold film heated to 250 °C ± 5 °C while continuously flowing N_2, subsequently followed by the addition of the Si precursor and O_2 for 105 s. The SEM images (**a**) and (**b**) were acquired at different locations on the same sample.

2.4.2 Formation of Individual Nanowires Beneath the Au–Si Catalyst

Figure 2.6 shows TEM images of SNSs and their Au–Si catalyst tips. The SNS growth time for the sample shown in Figure 2.6 was 5 min and the temperature inside the tube furnace at the termination of the 5 min growth cycle was 330 °C ± 5 °C. These images show that SNSs are composed of individual NWs coupled together via a common Au–Si catalyst tip (black areas). The formation of individual silica NWs below a common Au–Si catalyst can be explained thermodynamically in terms of the silica structure's surface free energy and the Au–Si catalyst. In the synthesis of a nanoscale structure with a high surface-area-to-volume ratio, the surface free energy is significant and very important to the growth kinetics. As solid silica is formed below the Au–Si catalyst, the system lowers its surface free energy by forming individual silica NWs instead of a solid silica structure. The low temperature of the process likely impedes the gold catalyst from forming a spherical or hemispherical shape, and once silica begins to form under the catalyst, the surface tension of the catalyst is unable to overcome the mechanical stiffness of the silica.
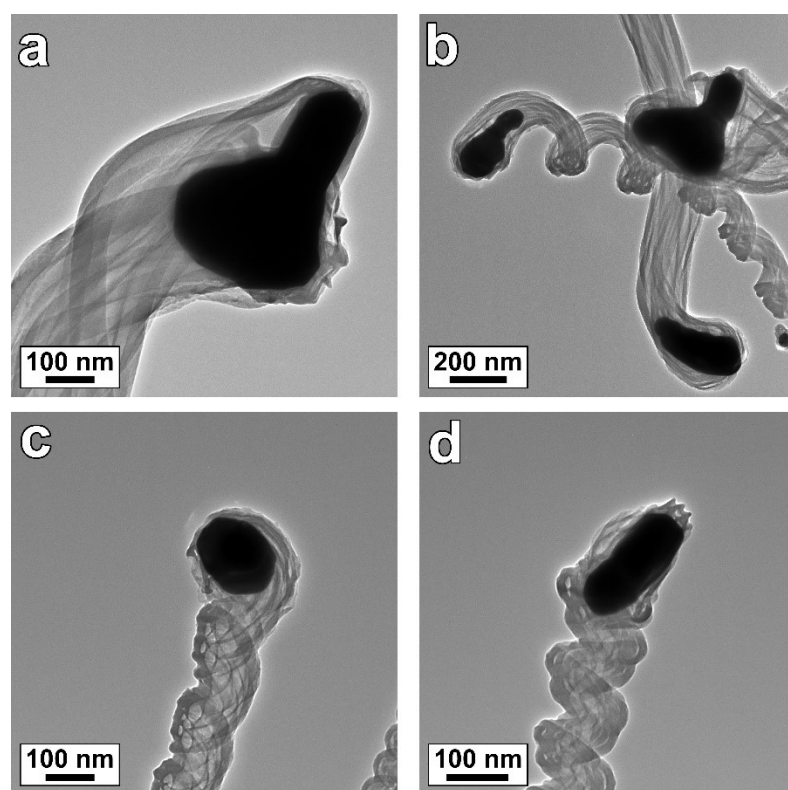
Figure 2.6 TEM images of SNSs which show that a SNS is composed of individual silica NWs. The solid black areas are the Au–Si catalyst tips.

2.4.3   Au–Si Catalyst Necking

The formation of individual NWs beneath the Au–Si catalyst is concomitant with the necking or "pinching" of the Au–Si catalyst. Figure 2.7 shows SEM images of the initial stages of SNS formation and the pinching of the Au–Si catalyst tip. The SNS growth time for the sample shown in Figure 2.7 was 150 s and the temperature inside the tube furnace at the termination of the 150 s growth cycle was 310 °C ± 5 °C. The SEM images show that SNSs are composed of individual NWs connected via a single Au–Si catalyst tip that exhibits necking, indicating that each silica NW is localized to a region of the Au–Si catalyst droplet. The individual NWs that comprise the SNS are not uniform in shape or diameter.
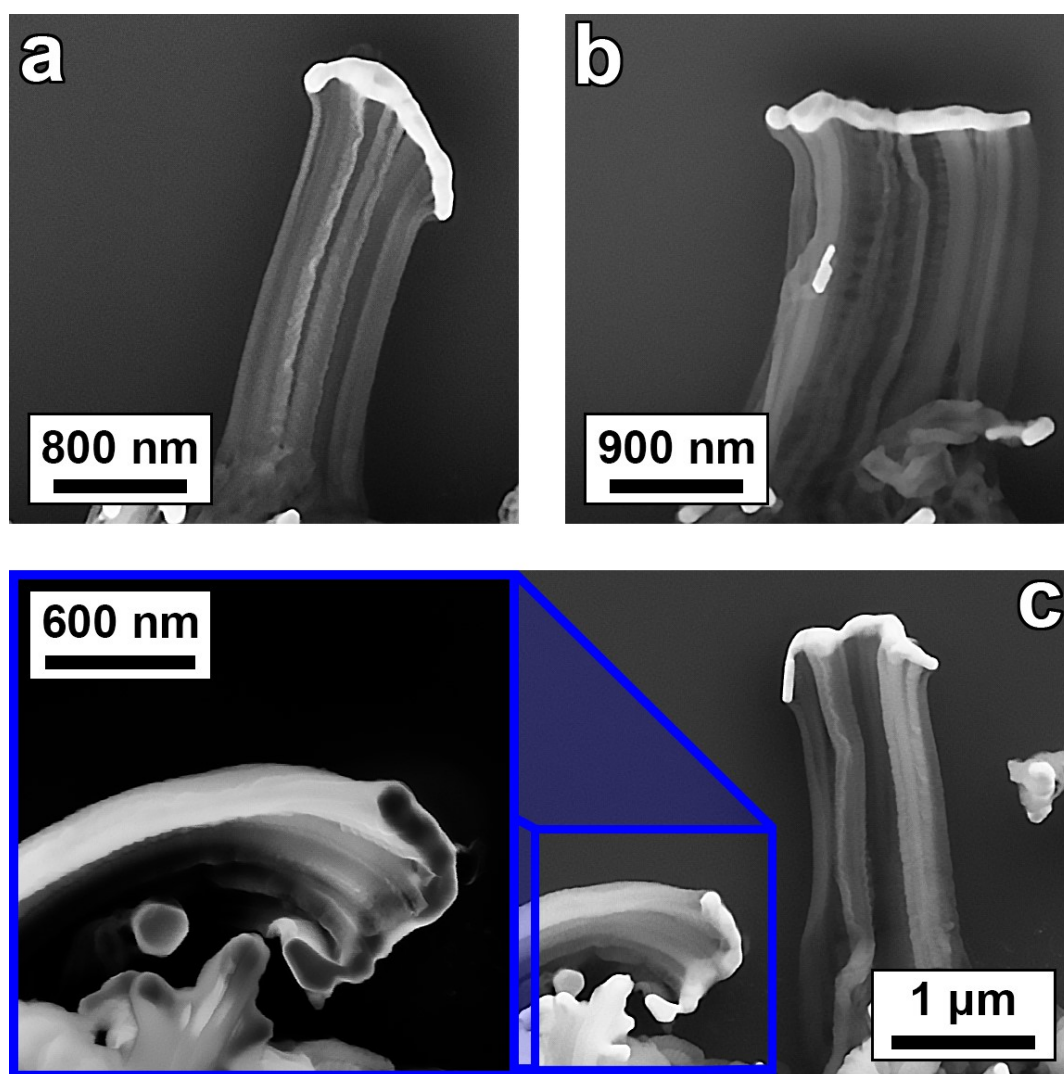
Figure 2.7 SEM images of the initial stages of SNS formation showing the individual NWs connected via a common Au–Si catalyst tip (white regions), which exhibits necking.

To better understand the necking process, approximate an asymmetrical bar-shaped catalyst at the initial stage of growth as a cylinder with hemispheres on both ends. Figure 2.8(a) shows a top-down view of this idealized geometry. The dotted lines represent four terminal locations of individual NWs nucleating from the catalyst, where each NW has unit radius. According to Laplace's Law, the wall tension on the cylindrical section is PR, and $PR/2$ on each of the spherical endcaps, where P is the pressure inside the catalyst droplet, and R is the radius of the cylinder and end caps. The total energy of the configuration in Figure 2.8(a) is $14\pi P\ m^3$. The total energy is reduced to $8\pi P\ m^3$ if the catalyst droplet takes the form of four individual spheres of unit radius, i.e., the individual NWs have their own spherical-shaped catalyst droplet as shown in Figure 2.8(b). Therefore, the necking of the catalyst droplet in Figure 2.8(c) is a result of the bar-shaped catalyst minimizing its energy. Note, the force exerted by the NWs on the gold catalyst is insufficient to overcome the surface tension of Au–Si eutectic, which is why they remain bundled together, as opposed to bifurcating into individual NWs.
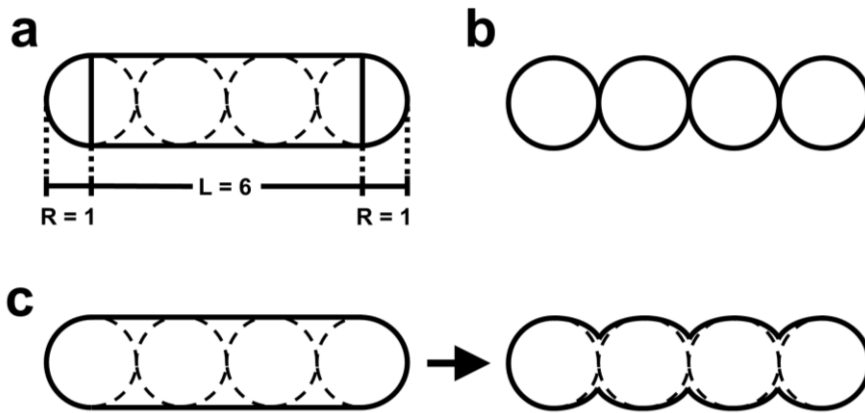
Figure 2.8 Schematic diagrams showing top-down views of: (**a**) An initial configuration of the Au–Si catalyst droplet that takes the shape of a three-dimensional cylinder with hemispherical caps. (**b**) An ideal configuration of four NWs nucleating from individual Au–Si catalyst droplets. (**c**) An initial configuration of an Au–Si catalyst droplet with four individual NWs (dotted lines) nucleating from beneath it and the subsequent necking of the catalyst droplet.

2.4.4   Growth Rates of Individual Nanowires

The twisting of the NW bundles and subsequent formation of a helical structure is driven by variations in the growth rates of the individual silica NWs growing beneath a common Au–

Si catalyst. The difference in growth rates of the individual NWs can be directly related to their diameters. The growth velocity or rate, v, of the individual NWs according to classical crystal growth kinetics theory is given by,

$$v = \mu_k \left(\frac{\Delta C}{kT}\right)^2, \tag{2.1}$$

where μ_k is the kinetic coefficient of growth at the solid–liquid interface, and ΔC is the supersaturation concentration [44–46]. In the context of the Gibbs–Thompson approach to VLS growth, the growth rate depends on the NW diameter via the supersaturation concentration, ΔC, as follows:

$$\Delta C = \Delta\mu_0 - \frac{4\Omega\alpha}{d_{\text{NW}}}, \tag{2.2}$$

where $\Delta\mu_0$ is the chemical potential difference of the Si compound in the vapor phase and Si in the solid phase in the NW at a plane boundary ($d_{\text{NW}} \rightarrow \infty$), Ω is the atomic volume of Si, and α is the surface free energy of the NW [44, 47–50]. Since the individual silica NWs beneath the catalyst have variable diameters, they have corresponding different growth rates.

The Au–Si catalyst shape is not well-defined in the early stages of SNS formation. It can range from an asymmetric bar or ribbon shape, as seen in Figure 2.7, to an asymmetrical spheroid shape, as shown in Figures 2.5, 2.6 and 2.9. Figure 2.9(a) shows an SEM image of SNSs with asymmetrically-shaped spheroid catalyst tips. The SNS growth time for the sample shown in Figure 2.9(a) was 105 s and the temperature inside the tube furnace at the termination of the 105 s growth cycle was 300 °C ± 5 °C. In the case of an asymmetrical spheroid Au–Si catalyst shape, the individual NWs are bundled beneath the catalyst in the configuration schematically represented in Figure 2.9(b). In this case, the NW bundle consists of tightly packed NWs surrounded by an outer group of NWs, which define the outer boundary of the SNS. We postulate that diffusion of O_2 to the inner NWs is hindered by the outer layer of NWs. Since the presence of O_2 is the driving force for SNS growth, a

lack of O_2 will inhibit growth on the inner NWs of a given bundle, thereby producing an additional anisotropy in the growth rate of the individual NWs.
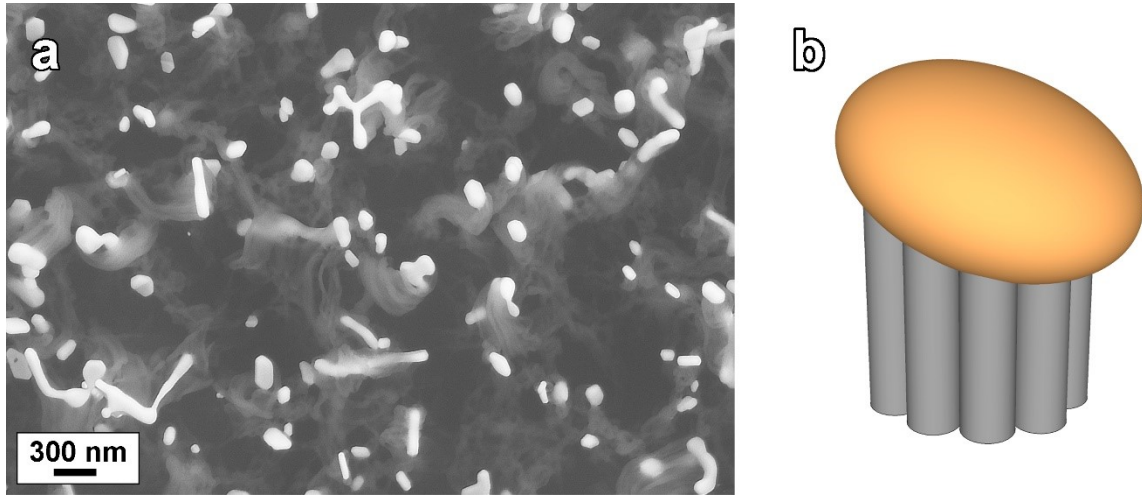
Figure 2.9 (**a**) SEM image of SNSs with asymmetrical spheroid-shaped catalyst tips. (**b**) Schematic representation of a SNS composed of a bundle of NWs connected to an asymmetrical spheroid-shaped catalyst tip.

2.4.5 Effective Contact Angle Anisotropy

Our initial study on the growth of boron carbide nanosprings proposed a modified VLS mechanism that identified contact angle anisotropy (CAA) as the mechanism responsible for the helical trajectory of nano- and micron-sized amorphous springs [16]. These boron carbide nanosprings consisted of a single amorphous boron carbide NW and a spherical Fe catalyst droplet, where the center of mass of the droplet was offset from the center of mass (axis) of the NW as shown in Figure 2.10(a). The CAA mechanism is directly related to the work of adhesion (W_A) of the NW catalyst droplet. The work of adhesion can be written as,

$$
\begin{aligned}
W_A &= \gamma_{SV} + \gamma_{SL} - \gamma_{LV} \\
&= \gamma_{SV} + \gamma_{SL} - (\gamma_{SL} + \gamma_{SV} \cos\theta) \\
&= \gamma_{SV}(1 - \cos\theta)
\end{aligned}
\tag{2.3}
$$

where γ_{SV}, γ_{SL}, and γ_{LV} are the interfacial surface tensions between the solid–vapor, solid–liquid, and liquid–vapor phases, respectively, and θ is the angle between the solid–vapor and

solid–liquid interfacial surface tensions. The probability of an atom diffusing through the liquid Fe to the droplet–NW interface and subsequently bonding at the liquid–solid interface is inversely proportional to the work of adhesion, i.e., the growth rate at a point of low work of adhesion (wetting interaction at interface B) is higher than the growth rate at a point of high work of adhesion (non-wetting interaction at interface A). Therefore, the offset Fe droplet creates an asymmetry in the growth rate at the liquid–solid interface that produces a helical precession of the catalyst droplet, and subsequently, the helical morphology of the NW.
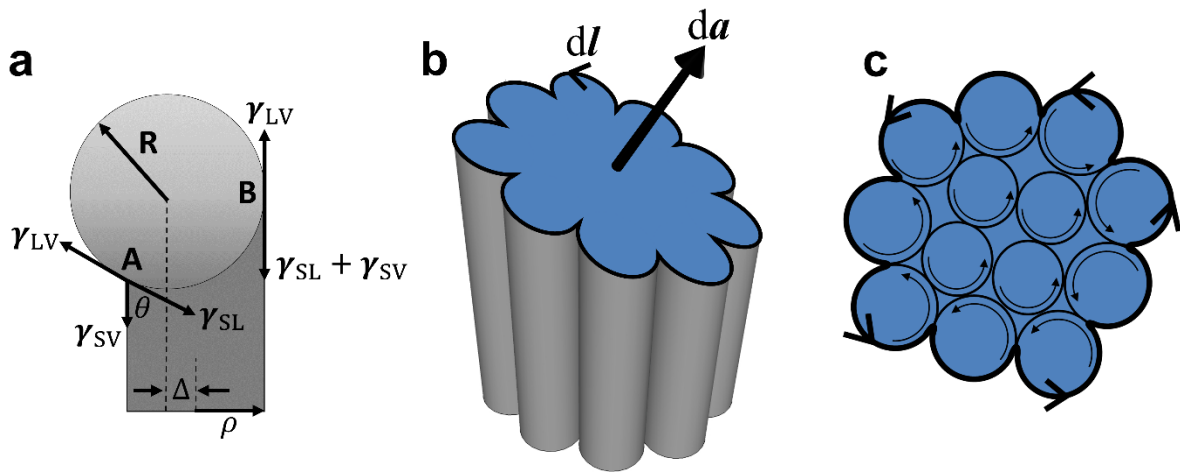
Figure 2.10 (**a**) Schematic diagram showing a spherical Fe catalyst droplet of radius, R, offset from the center of mass of a boron carbide NW by distance, Δ. (**b**) A schematic diagram of a SNS composed of 13 individual NWs. The surface, a, is the cross-sectional area of the catalyst–NWs interface, and l is the outer boundary of the catalyst–NWs interface, where $d\boldsymbol{a}$ and $d\boldsymbol{l}$ are differential elements of area, a, and outer boundary, l, respectively. (**c**) A top-down view of the cross-sectional area of the catalyst–NWs interface.

Since the individual NWs within a SNS are connected via a common catalyst and have different growth rates, there are variations in the work of adhesion (contact angle) around the perimeter of the individual NWs, as well as around the outer boundary of the NW bundle at the catalyst–NWs interface. Figure 2.10(b) shows a schematic diagram of a SNS that is composed of 13 individual NWs. The surface, a, is the cross-sectional area of the catalyst–NWs interface and l is the outer boundary of the SNS catalyst–NWs interface, where $d\boldsymbol{a}$ and $d\boldsymbol{l}$ are differential elements of area, a, that points normal to the interface and line, l, that encloses the area, respectively. The interfacial surface tension can be represented by vector

field, $\boldsymbol{\gamma}$. Figure 2.10(c) is a normal view of the catalyst–NWs interface shown in Figure 2.10(b). The arrows around the boundary of each NW represent the interfacial surface tension, $\boldsymbol{\gamma}$, and the dark outer line is the line that encloses the catalyst–NWs interface. According to Stokes' theorem,

$$\int (\boldsymbol{\nabla} \times \boldsymbol{\gamma}) \cdot d\boldsymbol{a} = \oint \boldsymbol{\gamma} \cdot d\boldsymbol{l}, \tag{2.4}$$

where the integral of the curl of the vector field, $\boldsymbol{\gamma}$, over surface, a, can be written as the line integral of $\boldsymbol{\gamma}$ about the boundary, l. Applying Stokes' theorem to this system demonstrates that the interfacial surface tension can be approximated by the interfacial surface tension about the boundary of the NW bundle of the SNS. The interfacial surface tension about the boundary can be used to calculate the work of adhesion. This leads to the conclusion that a modified version of the CAA model for a nanospring formed from a single NW can be applied to a SNS composed of a bundle of NWs.

The variable work of adhesion along the outer boundary of the catalyst–NWs bundle produces the asymmetry necessary for the helical precession of the catalyst and the subsequent helical morphology of the SNS. The net effect of the bundle of amorphous silica NWs beneath the catalyst is the creation of an effective CAA that produces the same asymmetric growth observed for a single amorphous nanospring [16, 18]. Note that the effective CAA mechanism can be applied to any Au–Si catalyst shape and NW configuration, provided that the nanospring is composed of several individual NWs connected by a common Au–Si catalyst.

Figure 2.11 shows SEM images of the initial twisting stages of SNSs. The SNS growth time for the sample shown in Figure 2.11 was 150 s and the temperature inside the tube furnace at the termination of the 150 s growth cycle was 310 °C ± 5 °C. Upon examination of Figure 2.11, it is clear that the SNSs are composed of many individual NWs connected via a common asymmetrically-shaped Au–Si catalyst. This is consistent with the TEM and SEM images of SNSs in Figures 2.6 and 2.7. The deformation and subsequent necking of the Au–Si catalyst is indicative of variations in the surface tension along the catalyst–NWs interface, which we argue gives rise to a variable work of adhesion, and ultimately leads to

the helical trajectory of the SNS. Bifurcation of the Au–Si catalyst is rarely observed, i.e., one or more of the NWs forming the SNS breaking away from the Au–Si catalyst droplet to form multiple SNSs. The energy necessary to shear a single silica NW or a group of individual silica NWs from the main Au–Si catalyst tip must be more than the energy required to rotate the system. This suggests that twisting of the NW bundle minimizes the energy of the SNS and that bifurcation is more energetically expensive.
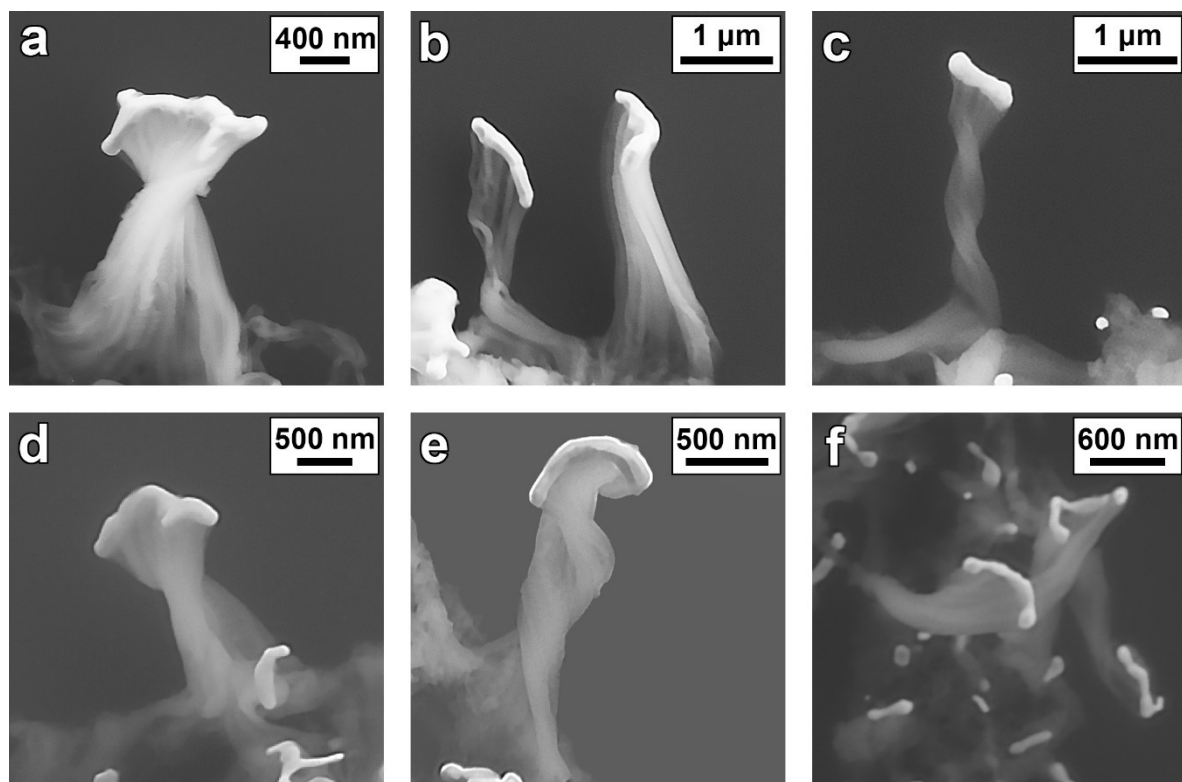
Figure 2.11 SEM images showing the initial twisting stages of SNSs. The white areas at the terminal location of each SNS are the Au–Si catalyst droplets.

2.5   Conclusion

The initial phases of SNS growth via a VLS mechanism at atmospheric pressure and relatively low temperature have been investigated. These conditions facilitate the formation of an asymmetrically-shaped Au–Si catalyst droplet. As solid silica is formed beneath the Au–Si catalyst, the silica structure lowers its surface free energy by forming individual silica NWs. Variations in the growth rates of individual NWs beneath a common Au–Si catalyst create an asymmetry in the interfacial surface tension about the boundary of the catalyst–

NWs interface of a SNS. The CAA mechanism responsible for the helical trajectory of boron carbide nanosprings formed from a single NW can be applied to the formation of SNSs from bundles of amorphous silica NWs connected via a common Au–Si catalyst. In this case, the bundle of NWs creates an effective CAA due to variations of the growth rates of individual NWs within the bundle. As was the case with the original CAA model, the effective CAA model can be applied to similar systems consisting of bundles of amorphous NWs and bundles of carbon nanotubes.

2.6   Acknowledgements

References

1.   Wojcik, P.M.; Bakharev, P.V.; Corti, G.; McIlroy, D.N. Nucleation, evolution, and growth dynamics of amorphous silica nanosprings. *Materials Research Express* **2017**, *4*, 015004.

2.   Cui, Y. Nanowire Nanosensors for Highly Sensitive and Selective Detection of Biological and Chemical Species. *Science* **2001**, *293*, 1289–1292.

3.   Kim, J.S.; Park, W.I.; Lee, C.-H.; Yi, G.-C. ZnO nanorod biosensor for highly sensitive detection of specific protein binding. *Journal of the Korean Physical Society* **2006**, *49*, 1635–1639.

4.   Timalsina, Y.P.; Branen, J.; Aston, D.E.; Noren, K.; Corti, G.; Schumacher, R.; McIlroy, D.N. Alternating current impedance spectroscopic analysis of biofunctionalized vertically-aligned silica nanospring surface for biosensor applications. *Journal of Applied Physics* **2011**, *110*, 014901.

5.   Sorgenfrei, S.; Shepard, K. Single-molecule electronic detection using nanoscale field-effect devices. In Proceedings of the DAC '11: Proceedings of the 48th Design Automation Conference; Association for Computing Machinery: New York, NY, USA, 2011; pp. 712–717.

6.   Liu, X.; Lin, P.; Yan, X.; Kang, Z.; Zhao, Y.; Lei, Y.; Li, C.; Du, H.; Zhang, Y. Enzyme-coated single ZnO nanowire FET biosensor for detection of uric acid. *Sensors and Actuators B: Chemical* **2013**, *176*, 22–27.

7.   Saltzgaber, G.; Wojcik, P.; Sharf, T.; Leyden, M.R.; Wardini, J.L.; Heist, C.A.; Adenuga, A.A.; Remcho, V.T.; Minot, E.D. Scalable graphene field-effect sensors for specific protein detection. *Nanotechnology* **2013**, *24*, 355502.

8. Leyden, M.R.; Messinger, R.J.; Schuman, C.; Sharf, T.; Remcho, V.T.; Squires, T.M.; Minot, E.D. Increasing the detection speed of an all-electronic real-time biosensor. *Lab on a Chip* **2012**, *12*, 954.

9. Panyam, J.; Labhasetwar, V. Biodegradable nanoparticles for drug and gene delivery to cells and tissue. *Advanced Drug Delivery Reviews* **2003**, *55*, 329–347.

10. Chan, C.K.; Peng, H.; Liu, G.; McIlwrath, K.; Zhang, X.F.; Huggins, R.A.; Cui, Y. High-performance lithium battery anodes using silicon nanowires. *Nature Nanotechnology* **2008**, *3*, 31–35.

11. Hsu, Y.-K.; Chen, Y.-C.; Lin, Y.-G.; Chen, L.-C.; Chen, K.-H. High-cell-voltage supercapacitor of carbon nanotube/carbon cloth operating in neutral aqueous solution. *Journal of Materials Chemistry* **2012**, *22*, 3383.

12. Yoo, J.J.; Balakrishnan, K.; Huang, J.; Meunier, V.; Sumpter, B.G.; Srivastava, A.; Conway, M.; Mohana Reddy, A.L.; Yu, J.; Vajtai, R.; et al. Ultrathin Planar Graphene Supercapacitors. *Nano Letters* **2011**, *11*, 1423–1427.

13. Tian, B.; Zheng, X.; Kempa, T.J.; Fang, Y.; Yu, N.; Yu, G.; Huang, J.; Lieber, C.M. Coaxial silicon nanowires as solar cells and nanoelectronic power sources. *Nature* **2007**, *449*, 885–889.

14. Garnett, E.C.; Brongersma, M.L.; Cui, Y.; McGehee, M.D. Nanowire Solar Cells. *Annual Review of Materials Research* **2011**, *41*, 269–295.

15. Tsakalakos, L.; Balch, J.; Fronheiser, J.; Korevaar, B.A.; Sulima, O.; Rand, J. Silicon nanowire solar cells. *Applied Physics Letters* **2007**, *91*, 233117.

16. McIlroy, D.N.; Zhang, D.; Kranov, Y.; Norton, M.G. Nanosprings. *Applied Physics Letters* **2001**, *79*, 1540.

17. McIlroy, D.N.; Alkhateeb, A.; Zhang, D.; Aston, D.E.; Marcy, A.C.; Norton, M.G. Nanospring formation—unexpected catalyst mediated growth. *Journal of Physics: Condensed Matter* **2004**, *16*, R415.

18. Zhang, D.; Alkhateeb, A.; Han, H.; Mahmood, H.; McIlroy, D.N.; Norton, M.G. Silicon Carbide Nanosprings. *Nano Letters* **2003**, *3*, 983–987.

19. Wang, L.; Major, D.; Paga, P.; Zhang, D.; Norton, M.G.; McIlroy, D.N. High yield synthesis and lithography of silica-based nanospring mats. *Nanotechnology* **2006**, *17*, S298–S303.

20. Fujii, M.; Matsui, M.; Motojima, S.; Hishikawa, Y. Magnetoresistance in carbon micro-coils annealed at various temperatures. *Journal of Crystal Growth* **2002**, *237*, 1937–1941.

21. Amelinckx, S.; Zhang, X.B.; Bernaerts, D.; Zhang, X.F.; Ivanov, V.; Nagy, J.B. A Formation Mechanism for Catalytically Grown Helix-Shaped Graphite Nanotubes. *Science* **1994**, *265*, 635–639.

22. Kato, Y.; Adachi, N.; Okuda, T.; Yoshida, T.; Motojima, S.; Tsuda, T. Evaluation of Induced Electromotive Force of a Carbon Micro Coil. *Japanese Journal of Applied Physics* **2003**, *42*, 5035.

23. Chen, X.; Zhang, S.; Dikin, D.A.; Ding, W.; Ruoff, R.S.; Pan, L.; Nakayama, Y. Mechanics of a Carbon Nanocoil. *Nano Letters* **2003**, *3*, 1299–1304.

24. Motojima, S.; Chen, X.; Yang, S.; Hasegawa, M. Properties and potential applications of carbon microcoils/nanocoils. *Diamond and Related Materials* **2004**, *13*, 1989–1992.

25. Motojima, S.; Noda, Y.; Hoshiya, S.; Hishikawa, Y. Electromagnetic wave absorption property of carbon microcoils in 12–110 GHz region. *Journal of Applied Physics* **2003**, *94*, 2325.

26. Luo, G.; Fouetio Kengne, B.-A.; McIlroy, D.N.; McDonald, A.G. A novel nano fischer-tropsch catalyst for the production of hydrocarbons. *Environmental Progress & Sustainable Energy* **2014**, *33*, 693–698.

27. Bakharev, P.; Dobrokhotov, V.; McIlroy, D. A Method for Integrating ZnO Coated Nanosprings into a Low Cost Redox-Based Chemical Sensor and Catalytic Tool for Determining Gas Phase Reaction Kinetics. *Chemosensors* **2014**, *2*, 56–68.

28. Schilke, K.F.; Wilson, K.L.; Cantrell, T.; Corti, G.; McIlroy, D.N.; Kelly, C. A novel enzymatic microreactor with Aspergillus oryzae β-galactosidase immobilized on silicon dioxide nanosprings. *Biotechnology Progress* **2010**, *26*, 1597–1605.

29. Hass, J.L.; Garrison, E.M.; Wicher, S.A.; Knapp, B.; Bridges, N.; Mcllroy, D.; Arrizabalaga, G. Synthetic osteogenic extracellular matrix formed by coated silicon dioxide nanosprings. *Journal of Nanobiotechnology* **2012**, *10*, 6.

30. Bakharev, P.V.; McIlroy, D.N. The effect of the periodic boundary conditions of a ZnO-coated nanospring on its surface redox-induced electrical response. *Nanotechnology* **2014**, *25*, 475501.

31. Dobrokhotov, V.; Oakes, L.; Sowell, D.; Larin, A.; Hall, J.; Kengne, A.; Bakharev, P.; Corti, G.; Cantrell, T.; Prakash, T.; et al. ZnO coated nanospring-based chemiresistors. *Journal of Applied Physics* **2012**, *111*, 044311.

32. Dobrokhotov, V.; Oakes, L.; Sowell, D.; Larin, A.; Hall, J.; Barzilov, A.; Kengne, A.; Bakharev, P.; Corti, G.; Cantrell, T.; et al. Thermal and Optical Activation Mechanisms of Nanospring-Based Chemiresistors. *Sensors* **2012**, *12*, 5608–5622.

33. Dobrokhotov, V.; Oakes, L.; Sowell, D.; Larin, A.; Hall, J.; Kengne, A.; Bakharev, P.; Corti, G.; Cantrell, T.; Prakash, T.; et al. Toward the nanospring-based artificial olfactory system for trace-detection of flammable and explosive vapors. *Sensors and Actuators B: Chemical* **2012**, *168*, 138–148.

34. Corti, G.; Zhan, Y.; Wang, L.; Hare, B.; Cantrell, T.; Ii, M.B.; Prakash, T.; Ytreberg, F.M.; Miller, M.A.; McIlroy, D.N. The effects of nanoscale geometry and spillover on room temperature storage of hydrogen on silica nanosprings. *Journal of Physics D: Applied Physics* **2013**, *46*, 505307.

35. Cheng, I.F.; Xie, Y.; Allen Gonzales, R.; Brejna, P.R.; Sundararajan, J.P.; Fouetio Kengne, B.A.; Eric Aston, D.; McIlroy, D.N.; Foutch, J.D.; Griffiths, P.R. Synthesis of graphene paper from pyrolyzed asphalt. *Carbon* **2011**, *49*, 2852–2861.

36. Wagner, R.S.; Ellis, W.C. Vapor-liquid-solid mechanism of single crystal growth. *Applied Physics Letters* **1964**, *4*, 89–90.

37. Malinský, P.; Slepička, P.; Hnatowicz, V.; Švorčík, V. Early stages of growth of gold layers sputter deposited on glass and silicon substrates. *Nanoscale Research Letters* **2012**, *7*, 241.

38. Siegel, J.; Kvítek, O.; Slepička, P.; Náhlík, J.; Heitz, J.; Švorčík, V. Structural, electrical and optical studies of gold nanostructures formed by Ar plasma-assisted sputtering. *Nuclear Instruments and Methods in Physics Research Section B: Beam Interactions with Materials and Atoms* **2012**, *272*, 193–197.

39. Švorčík, V.; Kvítek, O.; Lyutakov, O.; Siegel, J.; Kolská, Z. Annealing of sputtered gold nano-structures. *Applied Physics A* **2011**, *102*, 747–751.

40. Doron-Mor, I.; Barkay, Z.; Filip-Granit, N.; Vaskevich, A.; Rubinstein, I. Ultrathin Gold Island Films on Silanized Glass. Morphology and Optical Properties. *Chemistry of Materials* **2004**, *16*, 3476–3483.

41. Bal, J.K.; Hazra, S. Interfacial role in room-temperature diffusion of Au into Si substrates. *Physical Review B* **2007**, *75*, 205411.

42. Okamoto, H.; Massalski, T.B. The Au−Si (Gold-Silicon) system. *Bulletin of Alloy Phase Diagrams* **1983**, *4*, 190–198.

43. Zhang, M.; Wen, J.G.; Efremov, M.Y.; Olson, E.A.; Zhang, Z.S.; Hu, L.; de la Rama, L.P.; Kummamuru, R.; Kavanagh, K.L.; Ma, Z.; et al. Metastable phase formation in the Au-Si system via ultrafast nanocalorimetry. *Journal of Applied Physics* **2012**, *111*, 093516.

44. Biswas, S.; O'Regan, C.; Petkov, N.; Morris, M.A.; Holmes, J.D. Manipulating the Growth Kinetics of Vapor–Liquid–Solid Propagated Ge Nanowires. *Nano Letters* **2013**, *13*, 4044–4052.

45. Givargizov, E.I. Chapter 2. In *Highly Anisotropic Crystals*; Springer: New York, NY, USA, 1987; ISBN 978-90-277-2172-3.

46. Givargizov, E.I. Fundamental aspects of VLS growth. *Journal of Crystal Growth* **1975**, *31*, 20–30.

47. Weyher, J. Some notes on the growth kinetics and morphology of VLS silicon crystals grown with platinum and gold as liquid-forming agents. *Journal of Crystal Growth* **1978**, *43*, 235–244.

48. Wu, Y.; Fan, R.; Yang, P. Block-by-Block Growth of Single-Crystalline Si/SiGe Superlattice Nanowires. *Nano Letters* **2002**, *2*, 83–86.

49. Kikkawa, J.; Ohno, Y.; Takeda, S. Growth rate of silicon nanowires. *Applied Physics Letters* **2005**, *86*, 123109.

50. Dhalluin, F.; Baron, T.; Ferret, P.; Salem, B.; Gentile, P.; Harmand, J.-C. Silicon nanowires: Diameter dependence of growth rate and delay in growth. *Applied Physics Letters* **2010**, *96*, 133109.

CHAPTER 3

Utilizing a Single Silica Nanospring as an Insulating Support to Characterize the Electrical Transport and Morphology of Nanocrystalline Graphite

Peter M. Wojcik, Negar Rajabi, Haoyu Zhu, David Estrada, Paul H. Davis, Twinkle Pandhi, I. Francis Cheng, and David N. McIlroy

A graphitic carbon, referred to as graphite from the University of Idaho thermolyzed asphalt reaction (GUITAR), was coated on silica nanosprings and silicon substrates via the pyrolysis of commercial roofing tar at 800 °C in an inert atmosphere. Scanning electron microscopy and transmission electron microscopy images indicate that GUITAR is an agglomeration of carbon nanospheres formed by the accretion of graphitic flakes into a ~100 nm thick layer. Raman spectroscopic analyses, in conjunction with scanning electron microscopy and transmission electron microscopy, indicate that GUITAR has a nanocrystalline structure consisting of ~1–5 nm graphitic flakes interconnected by amorphous sp^3 bonded carbon. The electrical resistivities of 11 single GUITAR-coated silica nanospring devices were measured over a temperature range of 10–80 °C. The average resistivity of all 11 devices at 20 °C was $4.3 \pm 1.3 \times 10^{-3}$ Ω m. The GUITAR-coated silica nanospring devices exhibited an average negative temperature coefficient of resistivity at 20 °C of -0.0017 ± 0.00044 °C^{-1}, which is consistent with the properties of nanocrystalline graphite.

3.1   Author's Note

Most of the material presented in this chapter has been published in *Materials* **2019**, *12*, 3794 [1]. Additional information that does not appear in the journal publication has been included in the main body of the text to provide a more thorough examination of the topic. If the reader would like to cite the work presented in this chapter, we refer them to the published journal article.

3.2   Introduction

The carbon material dubbed graphite from the University of Idaho thermolyzed asphalt reaction (GUITAR) was first observed as the carbonaceous residue from the combustion of oil shale. Previous scanning electron microscopy (SEM) and optical images of GUITAR are consistent with a typical graphitic material [2]. X-ray photoelectron spectra indicate that the C bonding in GUITAR is a combination of sp^2 and sp^3 hybridized carbon [2], further supporting the conclusion that it is a form of graphite. However, GUITAR exhibits unique electrochemical properties that deviate from those of typical graphitic materials. The basal plane of GUITAR has fast heterogeneous electron transfer kinetics and outperforms

graphene, graphites, carbon nanotubes, boron-doped diamond, and diamond-like carbon [3, 4]. The aqueous anodic and cathodic limits notably exceed those of other graphitic carbons, which results in better corrosion resistance relative to other graphitic materials [3, 5]. These features make GUITAR an excellent candidate for use in applications such as sensors [6], energy storage and conversion [7], and water purification [4].

The unique electrochemical properties of GUITAR suggest that it is not just another form of graphite; further investigation of its morphology and electrical properties is required to classify GUITAR within the spectrum of carbon materials. The electrical resistivity and the temperature dependence on the resistivity of carbon nanocoils (NCs), graphite, and other allotropes of carbon vary greatly from allotrope to allotrope [8–20], thereby assisting in their identification and classification. The Raman spectra of the different carbon allotropes is equally diverse [21–29]. When taken in conjunction with one another, the electrical characterization and the Raman spectroscopy of GUITAR should be sufficient to identify and classify it within the spectrum of carbon allotropes.

Herein, we report on a unique approach to producing a better understanding of the morphology and electrical properties of GUITAR. GUITAR was coated onto silica nanosprings (SNSs), which served as an insulating support. Then, a single GUITAR-coated SNS (G–SNS) electrical device was fabricated to determine the electrical properties of GUITAR. The use of SNSs allowed us to precisely characterize the morphology of GUITAR and correlate it with its electrical properties. While this approach is not well-suited to single crystal materials, it is ideal for characterizing the electrical properties of amorphous and polycrystalline materials such as GUITAR.

3.3   Experimental Methods

3.3.1   Silica Nanospring Growth

SNSs were grown on Si/SiO$_2$ (500 nm thermal oxide) substrates using a modified chemical vapor deposition process described in chapter 2, and by Wojcik et al. [30] and Wang et al. [31]. The SNS growth time for the samples used in this study was ~10–15 min. The growth of SNSs on a flat substrate produces a highly dense mat resulting in an area density of

~1.5 mg of SNSs per cm^2 [32]. Figure 3.1 shows an SEM image of a dense mat of SNSs. The SNS growth time for the sample shown in Figure 3.1 was 10 min.
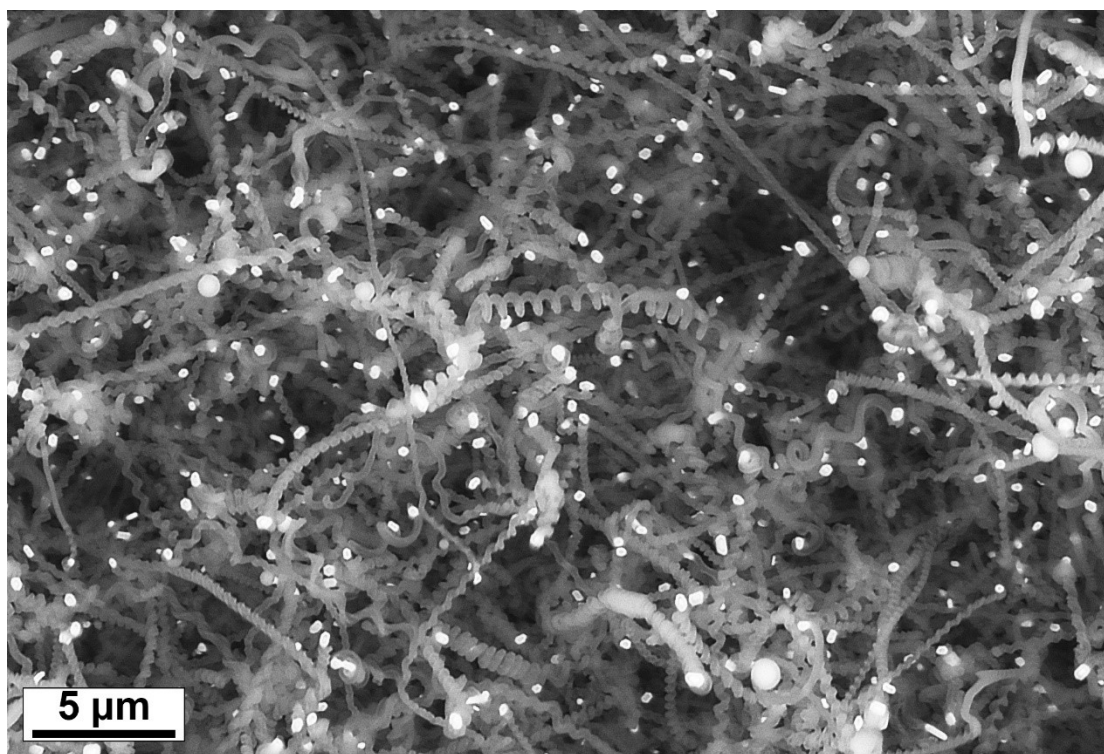
Figure 3.1 SEM image showing a dense mat of SNSs grown on a Si/SiO$_2$ substrate.

3.3.2   GUITAR Deposition

GUITAR was deposited onto the SNS surface via the pyrolysis of commercial roofing tar (asphalt) in a tube furnace operating at 800 °C under a continuous flow of N$_2$. The deposition of GUITAR has been previously described in detail [2, 5, 33]. This process was modified slightly to deposit a thin ~100 nm coating on the SNS surface. Figure 3.2 shows images of the GUITAR deposition process and experimental setup. Five grams of asphalt were wrapped in an alumina blanket and placed in the center of a hollow, 10 inch long by 3 inch diameter, steel cylindrical tube. The silicon substrate with a dense mat of SNSs was placed above the alumina blanket and the steel cylinder was placed in the center of the tube furnace. The furnace was ramped to 800 °C in 15 min while flowing N$_2$, then cooled slowly over five hours until the furnace temperature reached ~50 °C, at which point the sample was removed.
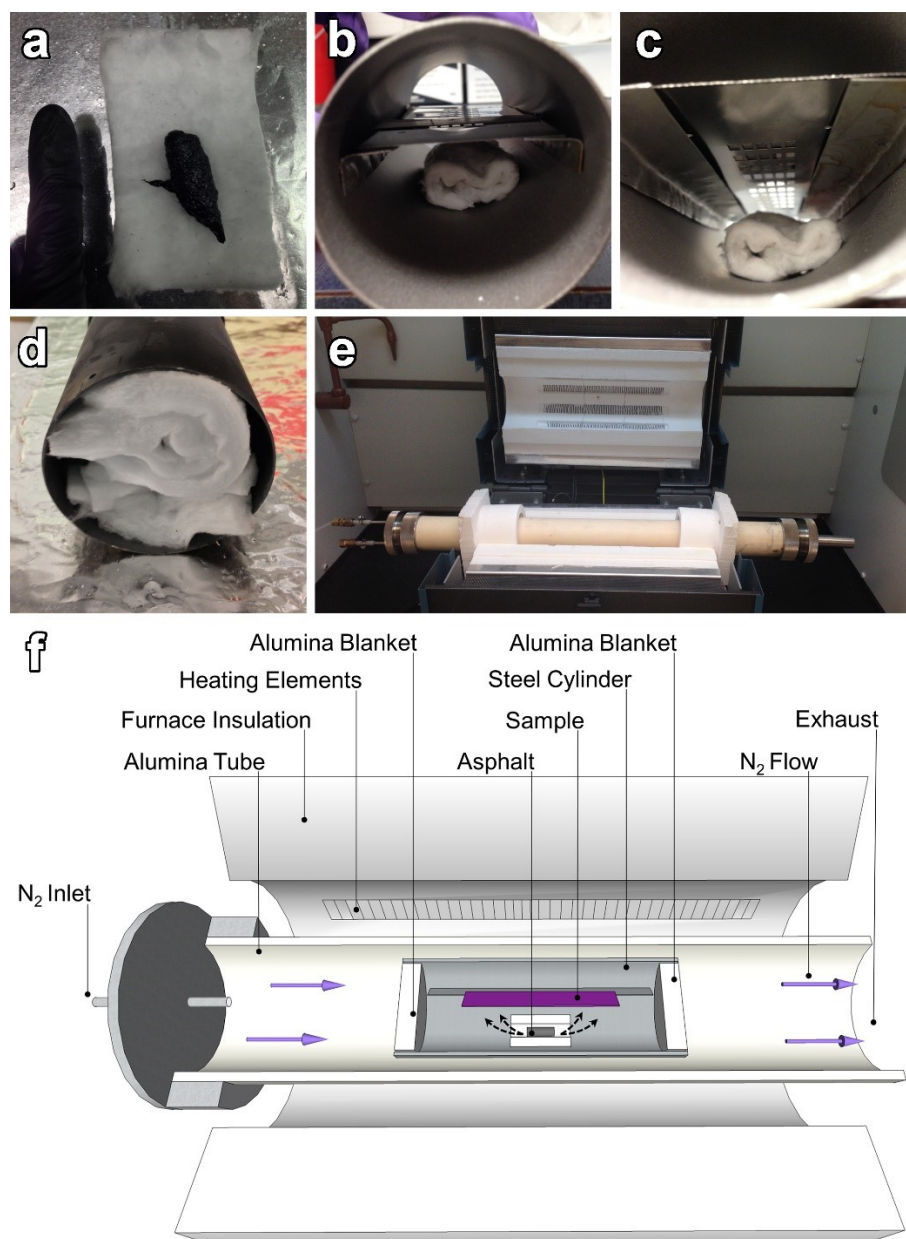
Figure 3.2 GUITAR deposition process and experimental setup. (**a**) Five grams of asphalt on an alumina blanket. (**b**) Alumina blanket with asphalt placed below a SNS sample inside a cylindrical steel tube. (**c**) SNS surface faces down toward the alumina blanket. (**d**) Endcaps of the cylindrical steel tube are capped with the alumina blanket (**e**) Tube furnace with the N_2 inlet on the left and open exhaust on the right. (**f**) Schematic diagram showing a sectional view of the experimental setup.

3.3.3   Device Fabrication

Figure 3.3 shows a schematic representation of the device fabrication process. Si/SiO$_2$ substrates with G–SNSs were placed in isopropanol (IPA) and vigorously agitated with a

submersed pipette to suspend the G–SNSs in IPA. 2.5×2.5 cm^2 Si/SiO$_2$ (500 nm thermal oxide) substrates (chips) were prepared for photolithography by cleaning sequentially with acetone, IPA, and deionized water, followed by drying with N$_2$. A drop-casting method was used to transfer the G–SNSs onto the chips by using a pipette to draw from the solution of G–SNSs/IPA and allowing the solution to evaporate on the chip surface. The drop-casting process was repeated until the desired amount of G–SNSs were deposited on the chip.
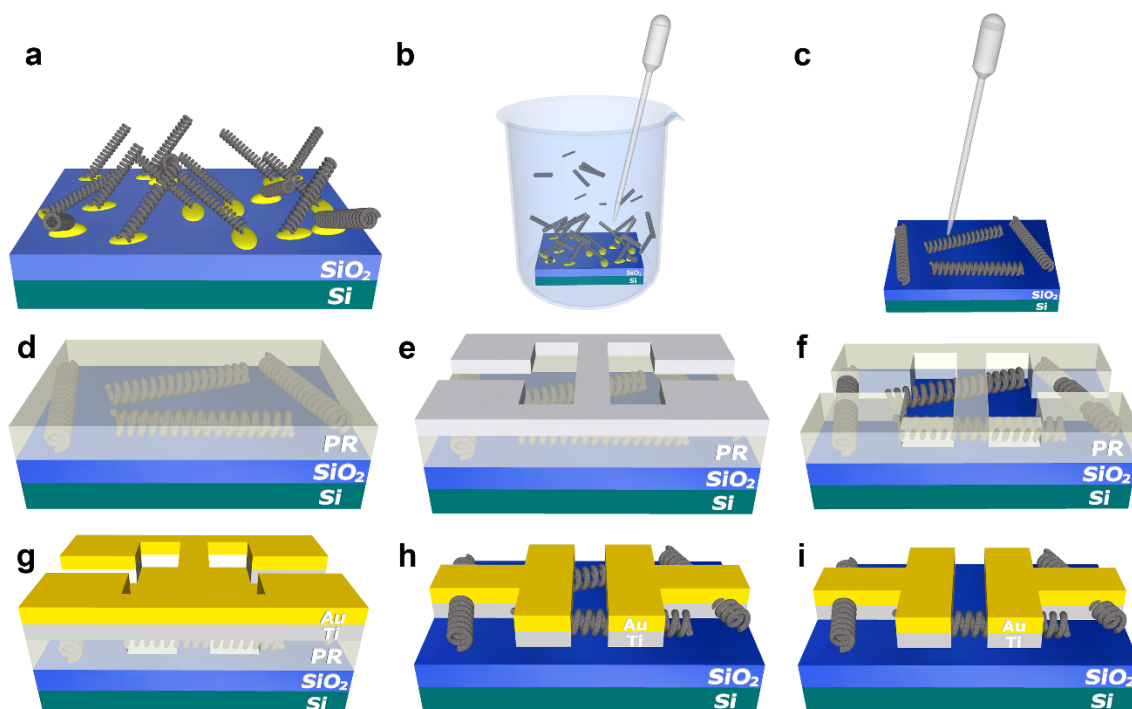
Figure 3.3 Schematic representation of the device fabrication process. (**a**) G–SNSs on Si/SiO$_2$ substrate. (**b**) G–SNSs released into IPA and (**c**) drop-cast onto the chip. (**d**) Photoresist is spun onto the chip. (**e**) UV light is exposed to photoresist with a chrome mask in place to create the electrode pattern. (**f**) The photoresist exposed to UV is removed with a developer. (**g**) Ti and Au are deposited via thermal evaporation and (**h**) the remaining photoresist and Ti/Au are removed in a solution of photoresist remover. (**i**) The electrode gap is cleared of G–SNSs with a micromanipulator until one G–SNS remains.

A standard bi-layer photolithography process, using LOR3A (lift-off resist) and SPR220-4.5 photoresist, was used to create a pattern of 27 interdigitated electrodes on the chip. Both resists were manufactured by MicroChem Corporation. The LOR3A provided an undercut layer beneath the SPR220-4.5, which facilitated the removal of the photoresist during the lift-off process. The patterned chips were coated sequentially with Ti (20 nm) and

Au (200 nm) via thermal evaporation to create electrical contacts; then the photoresist and Ti/Au were removed in photoresist remover. A micromanipulator (Micromanipulator Model 110 with a Model 7A probe tip, The Micromanipulator Co., Carson City, NV, USA) and an optical microscope were used to selectively remove the G–SNSs along the electrode gap until one G–SNS remained. Each interdigitated electrode had a ~12,000 μm long channel to increase the probability of making Ohmic contact with a single G–SNS. The yield for this design process was ~5 active devices per chip. Figure 3.4 shows a representation of the interdigitated electrode design and a false-color SEM image of a single G–SNS electrical device used in the experiments.
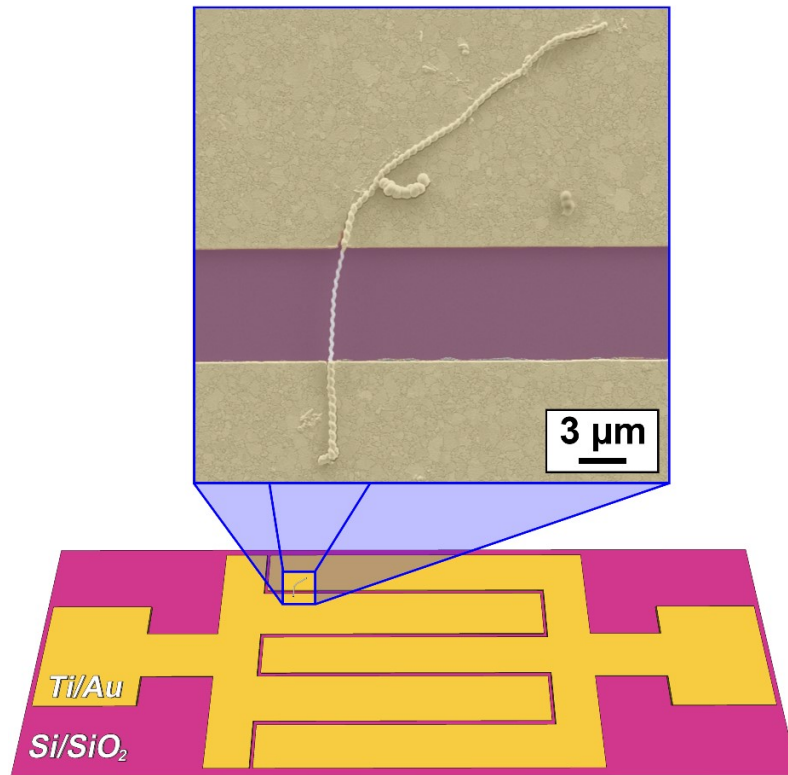
Figure 3.4 Interdigitated electrode design and false-color SEM image of a single G–SNS device.

3.3.4   Electrical Characterization

Figure 3.5 shows a schematic diagram of the experimental setup that was used for the electrical characterization of the single G–SNS devices. A two-point probe method was used to characterize the electrical properties of the single G–SNS devices. Electrical

measurements were acquired using a Keithley Model 2400 (Tektronix, Beaverton, OR, USA) and two micromanipulators (Micromanipulator Model 110 with Model 7A probe tips, The Micromanipulator Co., Carson City, NV, USA). The single G–SNS devices were heated/cooled by placing the devices on a single stage thermoelectric heater/cooler powered with an HP Model 6033A (Hewlett-Packard, Palo Alto, CA, USA) DC power supply. The device temperature was monitored with an Omega Model HH12 (Omega Engineering, Norwalk, CT, USA) digital thermometer.
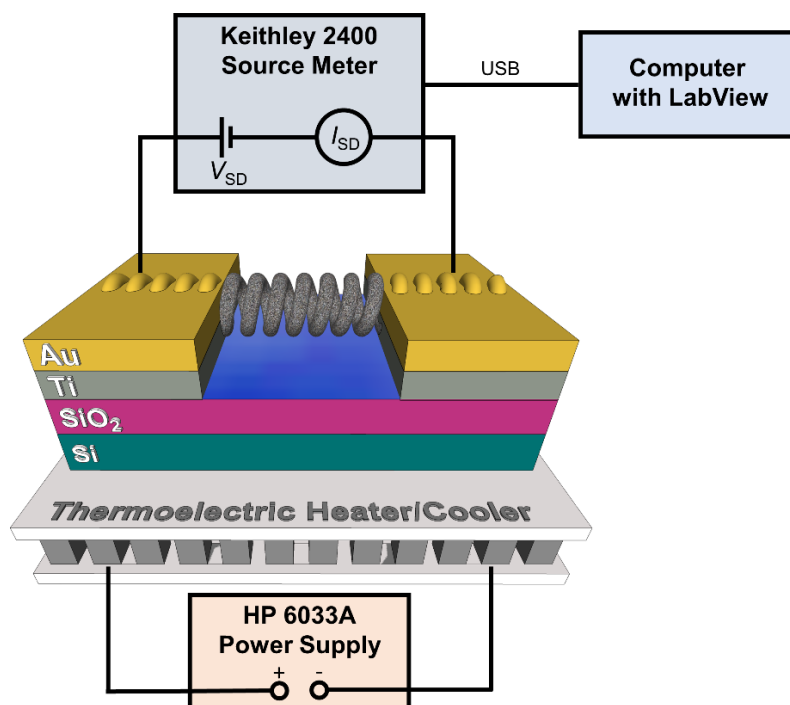
Figure 3.5 A schematic diagram of the experimental setup used for the electrical characterization of the single G–SNS devices.

3.3.5   *Microscopy Equipment*

Atomic force microscopy (AFM) images were obtained with a Veeco Autoprobe Di CP-II atomic force microscope (Veeco, Plainview, NY, USA) operating in non-contact mode with a 1 Hz scan rate. SEM images were obtained with a Zeiss Supra 35 scanning electron microscope (Zeiss, Peabody, MA, USA). Transmission electron microscopy (TEM) images were obtained with a JEOL-2010J transmission electron microscope (JEOL USA, Peabody, MA, USA) operating at 200 kV.

3.3.6   Raman Spectroscopy

In order to investigate the excitation wavelength dependence of GUITAR's Raman spectrum, Raman spectra of GUITAR thin films were collected using five different laser excitation wavelengths: 442 nm (HeCd), 488 nm and 514 nm (Ar ion), 532 nm (frequency doubled Nd:YAG), and 633 nm (HeNe). The Raman spectra at excitation wavelengths of 442 nm, 532 nm, and 633 nm were obtained with a LabRAM HR Evolution confocal Raman microscope (Horiba Scientific, Piscataway, NJ, USA) using a 100× 0.90 NA ultrashort (210 μm) working distance Olympus objective, which produced a spot size of ~600–900 nm at the sample surface depending on the excitation wavelength. Spectra were dispersed onto a thermoelectrically cooled CCD array detector using an 1800 line/mm grating blazed for visible wavelengths. Two 30 s accumulations were averaged to maximize signal to noise and enable removal of cosmic rays from the spectra. Neutral density filters were inserted into the excitation beam until no evidence of thermal (i.e., sample heating) or nonlinear (power) effects were seen in the resultant spectra. The system used for acquisition of Raman spectra at excitation wavelengths of 488 nm and 514 nm consisted of a Coherent Innova 90-3 argon ion laser (Coherent, Santa Clara, CA, USA) and a Horiba Jobin Yvon T64000 triple monochromator (Horiba Scientific, Piscataway, NJ, USA) equipped with a 2400 line/mm grating and a liquid nitrogen cooled CCD array detector. Spectra were collected at a laser power of 200 mW with a spot size of ~100 μm, corresponding to a power density ~2 orders of magnitude lower than the Raman microscope system and thus well below the threshold for any thermal or power effects. To ensure the Raman spectra obtained were representative, multiple locations across multiple samples were analyzed with both Raman systems.

3.4   Results and Discussion

3.4.1   Raman Spectroscopy

Figure 3.6(a) shows a Raman spectrum with a 532 nm excitation source of a GUITAR coating on a silicon substrate. The Raman spectrum in Figure 3.6(a) consists of two prominent peaks located at 1347 cm^{-1} and 1589 cm^{-1}, as well as a broad peak centered at ~2800 cm^{-1}. The peak at 1589 cm^{-1}, also known as the G peak, is attributed to a phonon with E_{2g} symmetry and is associated with in-plane bond stretching of pairs of sp^2 hybridized

carbon atoms [22, 34]. The wavenumber of the G peak falls in the range of 1500–1630 cm^{-1} and does not require the presence of six-fold rings, i.e., it is present for all sp^2 bonding [34]. The peak located at 1347 cm^{-1}, commonly denoted as the D peak, originates from a phonon with A$_{1g}$ symmetry [22]. The D peak, in conjunction with the G peak, is only observed in the presence of disorder and is not present in the Raman spectra of ideal graphite [22, 34]. A small, yet notable, feature is present on the shoulder of the D peak at ~1150 cm^{-1}. This peak is commonly used to characterize nanocrystalline diamond and attributed to sp^3 bonding [35–38]. However, Ferrari and Robertson argue that this peak must originate from an alternate chain of sp^2 carbon atoms formed by a single hydrogen bonded to each C [39]. A previous study of GUITAR using x-ray photoelectron spectroscopy showed that the material could possibly contain alternate chains of sp^2-bonded carbon atoms, such as C=N, which could account for the peak at ~1150 cm^{-1} [2].
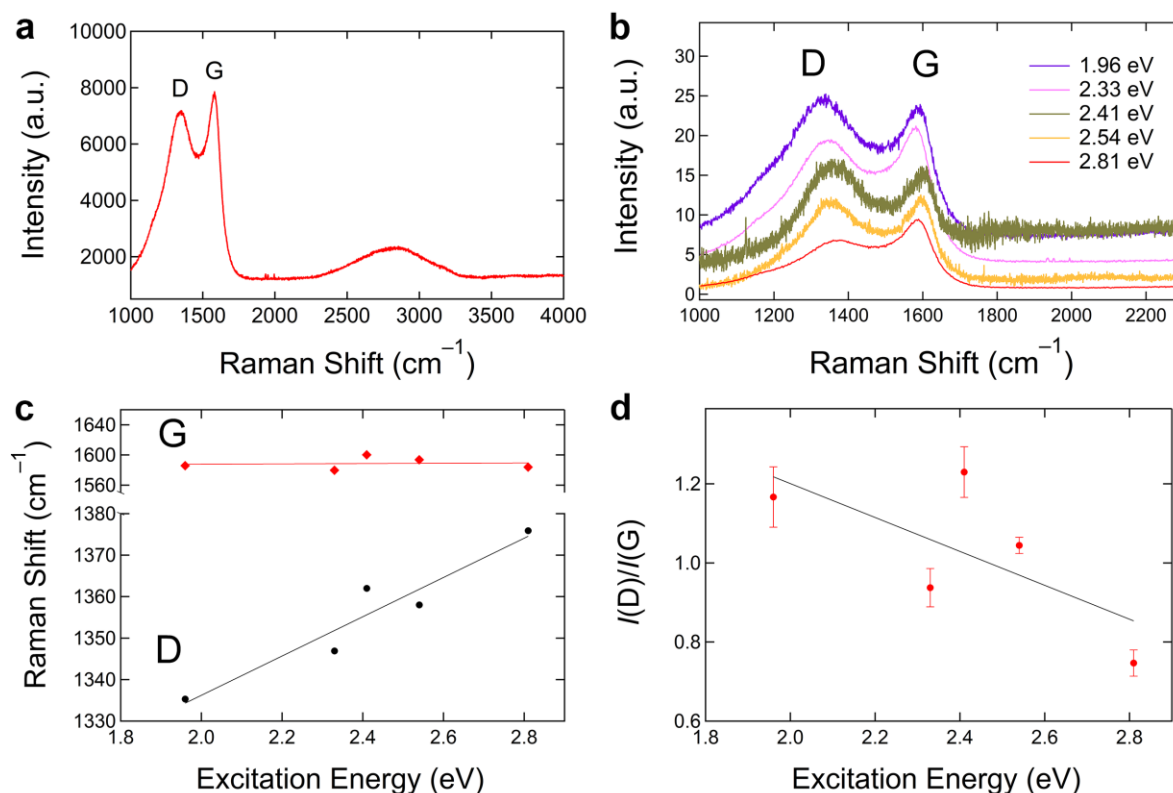
Figure 3.6 (**a**) Raman spectrum of GUITAR on a silicon substrate obtained with a 532 nm excitation source. (**b**) The Raman spectra of GUITAR for a variety of excitation energies showing the prominent D and G peaks. (**c**) The positions of the D and G peaks plotted as a function of excitation energy. (**d**) The ratio of the intensities of the D and G peaks as a function of excitation energy.

Ferrari and Robertson studied the visible Raman spectra of disordered carbons and presented a three stage model of disorder from graphite to amorphous carbon (a-C) that simplified the characterization of Raman spectra for all types of carbons [34]. The stages from ordered to disordered are as follows: Stage (1), graphite to nanocrystalline graphite; Stage (2), nanocrystalline graphite to a-C with a small sp^3 content; Stage (3), a-C to tetrahedral a-C with a high sp^3 content [34]. Each stage has unique features in its Raman spectra, which can be used to distinguish between the three stages. Most notable in the Raman spectrum of Figure 3.6(a) are the broad peak located at ~2800 cm^{-1} and the absence of well-defined second order G or D peaks. The span of the broad peak is from ~2300–3200 cm^{-1}. It is a feature that is only present in the evolution of Stage (2) of nanocrystalline graphite to a-C [34, 40] and is a combination of the 2D, D + D′, and 2D′ bands [34, 41].

The excitation energy dependence of GUITAR's Raman spectrum provides further evidence that GUITAR corresponds to Stage (2) carbon formation. Figure 3.6(b) shows the Raman spectra of GUITAR with 1.96 eV (633 nm), 2.33 eV (532 nm), 2.41 eV (514 nm), 2.54 eV (488 nm), and 2.81 eV (442 nm) excitation energies (wavelengths). The Raman spectrum for each excitation energy was fitted with a Lorentzian line shape for the D peak and a Breit–Wigner–Fano (BWF) line shape for the G peak. The BWF line shape function is,

$$I(\omega) = \frac{I_0[1 + 2(\omega - \omega_0)/Q\Gamma]^2}{1 + [2(\omega - \omega_0)/\Gamma]^2},$$

(3.1)

where I is the intensity, ω is the frequency, I_0 is the peak intensity, ω_0 is the peak position, Γ is the full width at half maximum, and Q is the BWF coupling coefficient. A Lorentzian shape is recovered in the limit $Q^{-1} \to 0$. The asymmetry of the BWF line can account for lower frequency Raman features at ~1100 cm^{-1} and 1400 cm^{-1} without the addition of two extra peaks [34], and the combination of the BWF and Lorentzian lines is a good fit for the Raman spectral features of all types of carbons and excitation energies [34]. We also define the G peak position as ω_{max} in Equation 3.2:

$$\omega_{max} = \omega_0 + \frac{\Gamma}{2Q}, \tag{3.2}$$

where ω_0 lies at higher frequencies because Q is negative and is the position of the undamped mode, and is therefore higher than the apparent G peak maximum [34]. We also define the ratio of the intensity of the D and G peaks ($I(D)/I(G)$) using the peak heights of the D and G bands rather than the peak areas, which is common when using two Gaussian fits for the D and G peaks. The positions of the D and G peak are plotted as a function of excitation energy in Figure 3.6(c). The vertical error bars in Figure 3.6(c) are smaller than the markers on the plot. The dispersion of the D peak as a function of excitation energy is ~48 cm^{-1}/eV and is consistent with the dispersion of the Raman D peak of microcrystalline graphite [42]. The dispersion of the D peak is present in the Raman spectra of all types of carbons and has been observed to have an inverse relationship with the degree of disorder [43]. We observe that the G peak position has little to no dependence with excitation energy and remains roughly flat at ~1580 cm^{-1}, as shown in Figure 3.6(c). These results are consistent with studies of the dispersion of the Raman G band of microcrystalline graphite, where Póscik et al. observed the G peak position to be independent of excitation energies ranging from ~1 eV to 4.5 eV and at a band position of ~1580 cm^{-1} [42]. In disordered carbons, the position of the G peak is positively correlated with excitation energy, and the degree of its dispersion increases with disorder [43]. For Stage (2) carbon, the position of the G peak decreases from ~1600 cm^{-1} to 1510 cm^{-1} for nanocrystalline graphite to a-C [34]. Additionally, the G peak does not disperse in nanocrystalline graphite [43], which suggests that GUITAR lies somewhere near the beginning of Stage (2) carbon formation, characteristic of nanocrystalline graphite with a low sp^3 content.

The $I(D)/I(G)$ ratio alone cannot be used to accurately estimate the sp^3 fraction of Stage (2) carbon. Ferrari and Robertson studied the Raman spectra of both an amorphization trajectory and an ordering trajectory with independent measures of the sp^3 fractions for each stage. They found a hysteresis cycle that shows no relationship between the $I(D)/I(G)$ ratio or the position of the G peak and the sp^3 fraction [34]. The $I(D)/I(G)$ ratio can, however, be used to estimate the crystalline size, L_a [22]. Tuinstra and Koenig showed that the $I(D)/I(G)$ ratio is inversely proportional to the average crystal size using the relationship,

$I(D)/I(G) = C(\lambda)/L_a$, where $C(514 \text{ nm}) \sim 4.4 \text{ nm}$ [21, 22, 44]. In the evolution of Stage (2) carbon, the $I(D)/I(G)$ ratio approaches zero and the Tuinstra–Koenig relation is no longer valid. Ferrari and Robertson proposed the following new relationship for a carbon nearing the end of Stage (2) and approaching that of a-C and the regime of $L_a < 2 \text{ nm}$: $I(D)/I(G) = C'(\lambda)/L_a^2$, where $C'(514 \text{ nm}) \sim 0.0055$ [34]. Figure 3.6(d) shows the ratio of the intensities of the D and G peaks plotted as a function of excitation energy. The features of the Raman spectra to this point are characteristic of nanocrystalline graphite with a low sp^3 content, which in Ferrari's three stage disorder spectrum lies somewhere in the beginning of Stage (2), yet its exact location in the evolution of Stage (2) is undetermined. We therefore estimated the crystal size using both the Tuinstra–Koenig and the Ferrari–Robertson relationship. We found that for a 514 nm source, the GUITAR crystal size was ~1.5 nm using the Ferrari–Robertson relationship and ~3.6 nm using the Tuinstra–Koenig relationship, setting limits on the crystal size of $1.5 \text{ nm} \le L_a \le 3.6 \text{ nm}$.

3.4.2   GUITAR Surface Morphology

Figure 3.7(a) is an SEM image of the G–SNS surface that exhibits a pattern of smooth hemispheres ~50–100 nm in diameter. Figure 3.7(b) is a TEM image of a single G–SNS. The TEM image in Figure 3.7(c) is a lateral view of the surface of a single G–SNS, showing the GUITAR/SNS interface. Figure 3.7(d) shows a detailed view of an individual carbon nanosphere in the GUITAR coating. The TEM images in Figure 3.7(b),(c) show the inner core of the SNS, which is comprised of several individual silica nanowires bundled together to form a larger, helical structure ~1 μm in diameter. The GUITAR coating is visible on the outer edge of the SNS and the GUITAR/SNS interface is well-defined. Bare silicon substrates were placed alongside the bulk SNS samples during the deposition of GUITAR to compare the surface morphology of GUITAR on SNSs and on a flat surface. The surface morphology of GUITAR on a flat silicon substrate, as shown in the AFM images in Figure 3.8, resembles that of a GUITAR coating on a SNS and confirms the presence of an agglomeration of hemispheres ~50–100 nm in diameter. TEM images of eight individual G–SNSs were used to calculate the average thickness of the GUITAR coating. For each of the eight G–SNSs, ~5–10 locations were chosen to measure the thickness of the coating. The total average thickness of the GUITAR coating was 87 ± 32 nm. The AFM images in

Figure 3.8 are consistent with both the SEM and TEM images in Figure 3.7, and these images together show that the GUITAR coating is a ~100 nm thick layer comprised of an agglomeration of irregularly shaped carbon nanospheres with diameters ranging from ~50 to 100 nm.
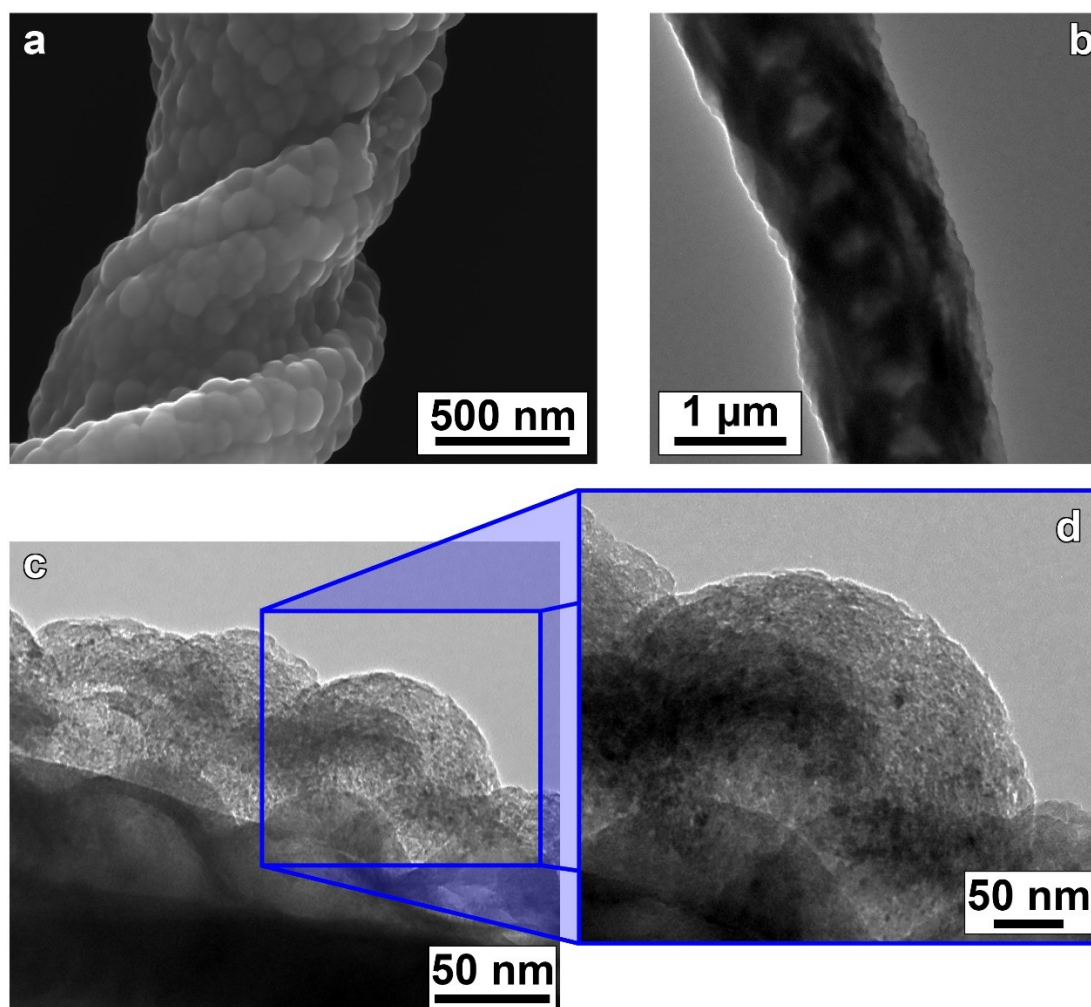
Figure 3.7 (a) SEM image of the surface of a G–SNS. (**b**) TEM image of a single G–SNS showing the GUITAR coating and the inner core of a SNS. (**c**) TEM image of a single G–SNS showing the interface of the SNS and the GUITAR coating. (**d**) TEM image showing a detailed view of an individual carbon nanosphere in the GUITAR coating.

Micrometer-sized and nanometer-sized carbon-shaped spheres have been produced via a plethora of methods, and a comprehensive study of the variety of morphologies has been conducted. Inagaki et al. proposed that spherical carbon bodies could be classified into three categories based on their nanometric texture, e.g., the concentric, radial, and random

arrangement of the carbon layers [45]. Serp et al. further classified spherical carbons with three additional categories based on their size: carbon onions and the C_n family, with diameters ranging from 2–20 nm; carbon nanospheres that exhibit a small degree of graphitization, with diameters ranging from 50 nm to 1 µm; and carbon beads that range in diameter from one to several microns [46]. Inagaki classified carbon nanospheres produced from the thermal decomposition of hydrocarbon gases as carbon blacks and proposed a concentric arrangement of carbon layers [45]. This concentric texture has been observed with TEM and shows that carbon nanospheres are composed of graphitic layers with unclosed graphitic flakes on their surfaces [47, 48]. Carbon nanospheres are also generally observed as an agglomeration of carbon spheres with varying diameters [47, 49–52]. The coalescence and accretion of carbon nanospheres was observed by Nieto-Marquez et al. via a catalytic growth method [51], Kang and Wang via catalytic carbonization after treatment in acetone [47], and by Jin et al. via the pyrolysis of a variety of hydrocarbons in the absence of a catalyst [50]. The accretion of carbon nanospheres can be attributed to the high surface reactivity resulting from dangling bonds on the unclosed graphitic flakes residing on the surface of the spheres [47, 48, 51].
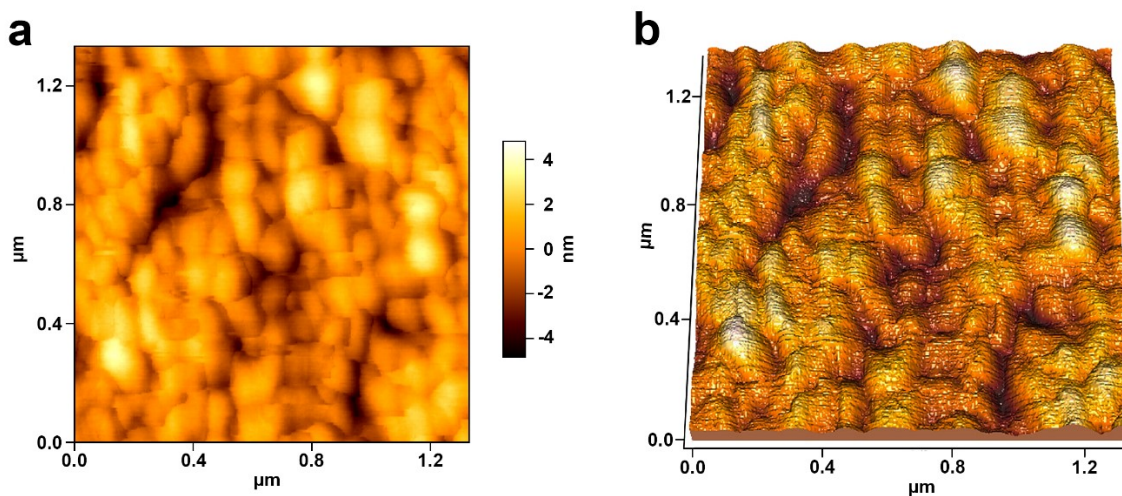
Figure 3.8 (**a**) Two-dimensional and (**b**) three-dimensional AFM images of a GUITAR coating on a silicon substrate.

Figure 3.7(d) shows a detailed view of an individual carbon nanosphere in the GUITAR coating. The morphology of its outer surface is nonuniform and shows that the sphere's

surface is comprised of unclosed graphitic flakes. Upon further inspection of the surface of the individual carbon nanosphere, we found that the flakes are nonuniform disks, which vary in diameter from ~1–5 nm. The sizes of these flakes are consistent with estimations of crystal size according to an analysis of GUITAR's Raman spectra, which showed that 1.5 nm $\leq L_a \leq$ 3.6 nm, and the $I(D)/I(G)$ ratio (Figure 3.6(d)), which also shows that GUITAR is characteristic of a material with a low degree of graphitization. All these features demonstrate that the building block of the GUITAR coating is a carbon nanosphere, per the description by Serp et al. and Inagaki et al., which agglomerate to form a film or coating in the case of the SNSs.

3.4.3   Electrical Characteristics

Figure 3.9(a) shows a false-color SEM image of a typical single G–SNS device spanning a ~6 µm gap between two Ti/Au source–drain electrodes. Figure 3.9(b) shows a typical two-point probe source–drain current–voltage (I_{SD}–V_{SD}) curve for a single G–SNS device at room temperature and atmospheric pressure. The inset in Figure 3.9(b) shows a three-dimensional schematic and electrical diagram of the single G–SNS device. The I_{SD}–V_{SD} curve is linear and indicative of Ohmic contacts. All of the devices tested in this work displayed Ohmic behavior. The total resistance (R_T) obtained from the two-point I_{SD}–V_{SD} measurement is the sum of the resistance of the single G–SNS (R_{G-SNS}) and of the two contact resistances (R_C) at the GUITAR–Ti/Au interface on each end: $R_T = R_{G-SNS} + 2R_C$. Previous studies on the contact resistance of single- and multi-layered graphene to Ti/Au metal contacts have reported contact resistances of <250 Ω for multi-layered graphene (~50 layers) [53], and ~165 Ω for single-layered graphene [54]. A comparison of the contact resistances for Ni contacts on graphene and highly ordered pyrolytic graphite (HOPG) has shown that the measurements are approximately two orders of magnitude higher for Ni contacts on graphene than on HOPG. This greater contact resistance is attributed to the higher charge density in HOPG [53]. Additionally, Venugopal et al. have shown that the contact resistance for metal contacts on multilayered graphene decreases as the number of graphene layers increases [53]; this is because increasing the number of graphene layers results in increased carrier concentration, until the structure approaches that of HOPG, i.e., becomes more metallic. Since the GUITAR coating is characteristic of a disordered

multilayered graphitic material, it must have a high charge density, representative of multi-layered graphene and HOPG. Therefore, the contact resistance of the GUITAR–Ti/Au is small (<250 Ω), or ~3 orders of magnitude smaller than the total resistance of a single G–SNS (~500 kΩ), and therefore can be neglected.
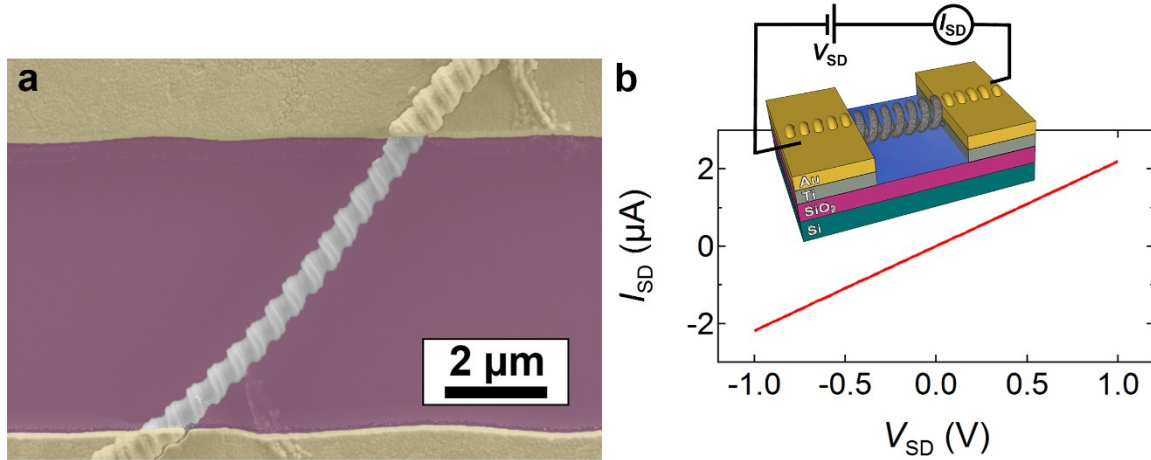
Figure 3.9 (**a**) False-color SEM image of a single G–SNS between two source–drain Ti/Au electrodes. (**b**) The Ohmic I_{SD}–V_{SD} curve of a typical G–SNS device and an inset showing a three-dimensional representation of the device and the corresponding electrical diagram.

The single G–SNS devices failed when the magnitude of I_{SD} exceeded ~10 μA. Care was taken to avoid applying a large current by keeping the magnitude of V_{SD} below 3 V. A gate voltage was applied to the G–SNS via a back-gate. I_{SD}–V_{SD} curves were measured while the back-gate voltage was held constant. There was no observable change in the resistance for back-gate voltages ranging from –20 V to 20 V, suggesting that the device did not exhibit a field effect, and therefore confirming that it is not semiconducting.

Eleven single G–SNS devices were used to determine the average resistivity and conductivity of the GUITAR coating. The resistivity (ρ) of each device was calculated using Equation 3.3:

$$\rho = R\frac{A}{L},$$
(3.3)

where R is the average resistance of the device, A is the cross-sectional area of the GUITAR coating on the SNS, and L is the length of the G–SNS. For each single G–SNS device, the slopes of five I_{SD}–V_{SD} curves from ±1 V were taken at 20 °C and used to calculate the average resistance for each device. The cross-sectional area of the GUITAR coating was determined from the average thickness of the GUITAR coating calculated from the TEM images, as described in section 3.4.2. SEM images of each device were used to determine the radius and length of the G–SNS. The helical pitch of an individual SNS is random and uncontrollable during the growth process. Therefore, the helical pitches of the single G–SNS devices are also random. However, the helical pitch of the single G–SNS devices in this study were well-defined and constant along the entire span of the electrode gap, meaning the G–SNS can be represented as a helix with constant radius in the active region of each device, which allowed for the calculation of the wire diameter and length of each G–SNS. In some instances, the pitch of the G–SNS was small, so that adjacent coils are in contact with one another, creating a closed coil along the entire length of its active area in the device. In this case, the G–SNS was treated as a wire and an average diameter was calculated over the pitch of two adjacent coils. The average resistivity calculated from the slopes of five I_{SD}–V_{SD} curves at 20 °C for each device is shown in Table 3.1. The total average resistivity of the 11 single G–SNS devices at 20 °C is $4.3 \pm 1.3 \times 10^{-3}$ Ω m.

Table 3.1 The average resistivity of the 11 single G–SNS devices calculated from the slopes of five I_{SD}–V_{SD} curves at 20 °C for each device.

Device	Average Resistivity (Ω m) at 20 °C
1	$3.1 \pm 0.62 \times 10^{-3}$
2	$20 \pm 3.8 \times 10^{-3}$
3	$7.4 \pm 1.4 \times 10^{-3}$
4	$3.6 \pm 0.75 \times 10^{-3}$
5	$2.1 \pm 0.62 \times 10^{-3}$
6	$4.9 \pm 1.1 \times 10^{-3}$
7	$1.6 \pm 0.18 \times 10^{-3}$
8	$1.3 \pm 0.25 \times 10^{-3}$
9	$1.2 \pm 0.19 \times 10^{-3}$
10	$1.6 \pm 0.34 \times 10^{-3}$
11	$0.92 \pm 0.16 \times 10^{-3}$

The temperature-dependent I_{SD}–V_{SD} curves of a single G–SNS device (device 3) from 10–80 °C in increments of 10 °C are displayed in Figure 3.10(a). The inset in Figure 3.10(a) shows the upper range of the I_{SD}–V_{SD} plot and the device's linear change in resistance as a function of temperature. Note that the I_{SD}–V_{SD} curve remains Ohmic across the entire temperature range. The slopes of five I_{SD}–V_{SD} curves were used to calculate the average resistivity at each temperature, which are presented in Figure 3.10(b). The vertical error bars are smaller than the markers used in the plot. The resistivity of the device is linear with respect to temperature and decreases at $\sim -1.8 \times 10^{-5}$ Ω m/°C, i.e., has a negative slope.
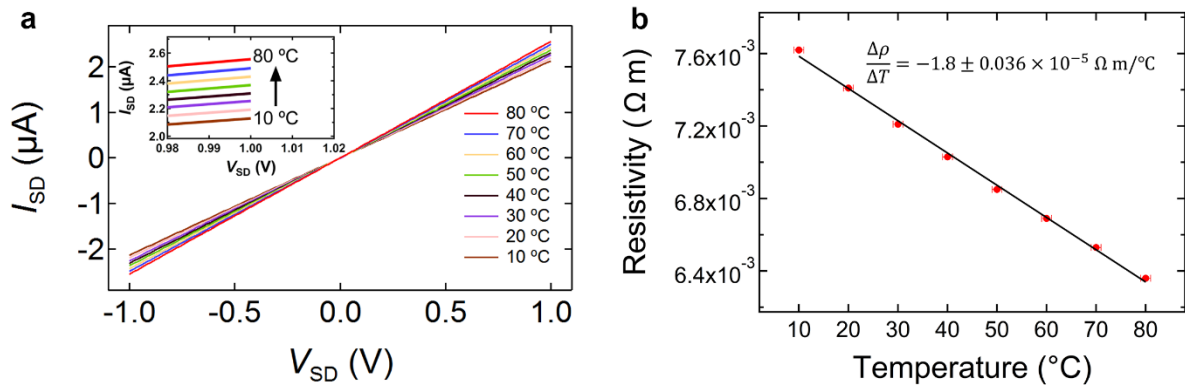
Figure 3.10 (**a**) Temperature-dependent I_{SD}–V_{SD} curves of a single G–SNS device (device 3) from 10–80 °C, where the inset is an expanded view of the upper range of I_{SD}–V_{SD}. (**b**) The resistivity vs. temperature profile for the same single G–SNS device, which displays a negative linear slope.

The linear relationship between resistivity and temperature was used to calculate the negative temperature coefficient of resistivity (TCOR) at 20 °C. The resistivity of the G–SNS can be expressed as a function of the temperature (T) as:

$$\rho(T) = \rho_0 \left[1 + \alpha_0 (T - T_0)\right], \tag{3.4}$$

where T_0 is the reference temperature at 20 °C, ρ_0 is the resistivity at the reference temperature, and α_0 is the TCOR at 20 °C. For each of the 11 single G–SNS devices, the slope of the resistivity vs. temperature profile ($\Delta\rho/\Delta T$) was obtained from a linear fit of the

data, as shown in Figure 3.10(b). The resistivity at the reference temperature of 20 °C for each device (Table 3.1) and $\Delta\rho/\Delta T$ were used to calculate α_0 with Equation 3.5:

$$\alpha_0 = (\Delta\rho/\Delta T)\rho_0{}^{-1}. \qquad (3.5)$$

All the single G–SNS devices displayed equivalent temperature dependence, as shown in Figure 3.10(b), Table 3.2, and appendix A. Appendix A shows the resistivity vs. temperature profiles and false-color SEM images of all 11 G–SNS devices. The slope of the resistivity vs. temperature profile, the resistivity at the reference temperature (ρ_0), and the calculated TCOR for each device are shown in Table 3.2. The average TCOR of the 11 single G–SNS devices at 20 °C was -0.0017 ± 0.00044 °C^{-1}.

Table 3.2 The slope of the resistivity vs. temperature profile ($\Delta\rho/\Delta T$), the resistivity at the reference temperature (ρ_0), and the calculated TCOR for each device.

Device	$\Delta\rho/\Delta T$ (Ω m/°C)	ρ_0 (Ω m)	TCOR (°C^{-1})
1	$-8.9 \pm 1.2 \times 10^{-6}$	$3.1 \pm 0.62 \times 10^{-3}$	$-2.9 \pm 0.69 \times 10^{-3}$
2	$-5.0 \pm 1.5 \times 10^{-5}$	$20 \pm 3.8 \times 10^{-3}$	$-2.5 \pm 0.88 \times 10^{-3}$
3	$-1.8 \pm 0.036 \times 10^{-5}$	$7.4 \pm 1.4 \times 10^{-3}$	$-2.4 \pm 0.46 \times 10^{-3}$
4	$-3.1 \pm 0.32 \times 10^{-6}$	$3.6 \pm 0.75 \times 10^{-3}$	$-0.87 \pm 0.20 \times 10^{-3}$
5	$-3.7 \pm 0.097 \times 10^{-6}$	$2.1 \pm 0.62 \times 10^{-3}$	$-1.8 \pm 0.52 \times 10^{-3}$
6	$-7.9 \pm 0.36 \times 10^{-6}$	$4.9 \pm 1.1 \times 10^{-3}$	$-1.6 \pm 0.37 \times 10^{-3}$
7	$-2.3 \pm 0.032 \times 10^{-6}$	$1.6 \pm 0.18 \times 10^{-3}$	$-1.4 \pm 0.17 \times 10^{-3}$
8	$-1.6 \pm 0.043 \times 10^{-6}$	$1.3 \pm 0.25 \times 10^{-3}$	$-1.2 \pm 0.24 \times 10^{-3}$
9	$-1.3 \pm 0.056 \times 10^{-6}$	$1.2 \pm 0.19 \times 10^{-3}$	$-1.0 \pm 0.17 \times 10^{-3}$
10	$-2.2 \pm 0.049 \times 10^{-6}$	$1.6 \pm 0.34 \times 10^{-3}$	$-1.4 \pm 0.29 \times 10^{-3}$
11	$-1.2 \pm 0.069 \times 10^{-6}$	$0.92 \pm 0.16 \times 10^{-3}$	$-1.3 \pm 0.24 \times 10^{-3}$

The electrical resistivity and, in particular, the temperature dependency of the resistivity of carbon NCs, graphite, and other allotropes of carbon are well-known and have been studied extensively [8–20]. At and near room temperature, the temperature dependence of the resistivity for conductive carbons is linear and the TCOR can be calculated using Equation 3.5. The calculated TCOR values of various conductive carbons are summarized in Table 3.3. Many authors have reported the temperature dependent resistivities for large temperature ranges (~0 K to 2000 K), but they did not specifically calculate the TCOR in the room temperature regime. All the TCOR values listed in Table 3.3, except for GUITAR,

were extrapolated from the linear regime of the resistivity vs. temperature plots near room temperature and for ΔT ~100 °C.

Table 3.3 Comparison of the resistivities, conductivities, and TCOR values for a variety of materials, including GUITAR.

Material	Resistivity ρ (Ω m) at 20 °C	Conductivity σ (S/m) at 20 °C	Temperature Coefficient at 20 °C (°C^{-1})	Reference
GUITAR	4.3×10^{-3}	2.3×10^2	-0.0017	This Study
Carbon Onions	2.5×10^{-3}	4.0×10^2	N/A	[55]
Carbon Black	1.7×10^{-3}	6.1×10^2	-0.00094	[10]
a-C (70 nm thick)	1.0×10^{-3}	1.0×10^3	N/A	[8]
Graphitized Soot	3.3×10^{-4}	3.0×10^3	-0.0014	[10]
Carbon NC	1.9×10^{-4}	5.3×10^3	-0.0012	[18]
POCO Graphite AF	9.6×10^{-5}	1.1×10^4	-0.0023	[10]
Lampblack Graphite	5.5×10^{-5}	1.8×10^4	-0.0013	[20]
Carbon	4.5×10^{-5}	2.2×10^4	-0.00040	[12]
Grade AGOT Graphite	1.0×10^{-5}	9.7×10^4	-0.0016	[20]
Natural Graphite	9.8×10^{-6}	1.0×10^5	-0.0010	[20]
Grade CS Graphite	7.7×10^{-6}	1.3×10^5	-0.0017	[20]
Acheson Graphite	6.3×10^{-6}	1.6×10^5	-0.0011	[12]
Carbon NC (as grown)	3.6×10^{-6}	2.8×10^5	-0.0015	[19]
Carbon NC (annealed)	4.1×10^{-7}	2.4×10^6	-0.00072	[19]

The negative temperature dependent resistivity of G–SNS is consistent with GUITAR being a graphitic form of carbon. The measured resistivity of GUITAR corresponds with measurements of the resistivity of similarly highly disordered carbon allotropes at room temperature, and it is on the order of the resistivities of an a-C thin film (70 nm) [8], nanodiamond-derived carbon onion electrodes [55], and carbon black [10]. The resistivity of GUITAR is also within an order of magnitude of the resistivities of graphitized soot [10] and carbon NCs [18] (Table 3.3). The TEM images of GUITAR in Figure 3.7 are similar to TEM images of carbon black [56] and graphitized soot [57, 58], which is indicative of similar morphologies and chemical compositions, i.e., a low degree of graphitization. The higher conductivities of the remainder of the carbon materials in Table 3.3 scale with their degree of graphitization.

Using the TCOR alone from Table 3.3, it is difficult to distinguish a pure graphite from more disordered allotropes of carbon, such as a-C. It is therefore important to consider both the resistivity and the TCOR of GUITAR when classifying it within the spectrum of

graphitic materials. GUITAR's negative TCOR near room temperature corresponds with all the carbon allotropes listed in Table 3.3 and confirms its classification as a graphitic semimetal material. The Raman spectra; AFM, SEM and TEM images; the negative TCOR at and near room temperature; and the resistivity of GUITAR confirm that it is a graphitic semimetal composed of nanocrystalline graphite.

3.5 Conclusion

We used a combination of Raman spectroscopy, AFM, SEM, and TEM images, and the electrical characterization of 11 single G–SNS devices to study the nanostructure, surface morphology, electrical resistivity, and negative TCOR of GUITAR in order to classify GUITAR within the spectrum of carbon materials. The Raman spectra of GUITAR were consistent with nanocrystalline graphite, in that it had low sp^3 content with an estimated crystalline size of ~1.5–3.6 nm. AFM, SEM, and TEM images show that GUITAR is an agglomeration of carbon nanospheres, where their surface is comprised of unclosed graphitic flakes ~1–5 nm in size. The electrical properties of GUITAR, as determined from the electrical measurements of 11 single G–SNS devices, demonstrate that it is a semimetal and that it has properties consistent with those of nanocrystalline graphite. With this study, we have definitively identified GUITAR as a nanocrystalline form of graphite where the sp^2 bonded graphite nanocrystals are connected via sp^3 bonding. Finally, we have demonstrated the utility of SNSs as an insulating support for measuring the electrical properties of amorphous and polycrystalline materials, or in this case, GUITAR.

3.6 Acknowledgments

References

1. Wojcik, P.M.; Rajabi, N.; Zhu, H.; Estrada, D.; Davis, P.H.; Pandhi, T.; Cheng, I.F.; McIlroy, D.N. Utilizing a Single Silica Nanospring as an Insulating Support to Characterize the Electrical Transport and Morphology of Nanocrystalline Graphite. *Materials* **2019**, *12*, 3794.

2. Cheng, I.F.; Xie, Y.; Allen Gonzales, R.; Brejna, P.R.; Sundararajan, J.P.; Fouetio Kengne, B.A.; Eric Aston, D.; McIlroy, D.N.; Foutch, J.D.; Griffiths, P.R. Synthesis of graphene paper from pyrolyzed asphalt. *Carbon* **2011**, *49*, 2852–2861.

3. Gyan, I.O.; Wojcik, P.M.; Aston, D.E.; McIlroy, D.N.; Cheng, I.F. A Study of the Electrochemical Properties of a New Graphitic Material: GUITAR. *ChemElectroChem* **2015**, *2*, 700–706.

4. Villarreal, C.C.; Pham, T.; Ramnani, P.; Mulchandani, A. Carbon allotropes as sensors for environmental monitoring. *Current Opinion in Electrochemistry* **2017**, *3*, 106–113.

5. Cheng, I.F.; Xie, Y.; Gyan, I.O.; Nicholas, N.W. Highest measured anodic stability in aqueous solutions: graphenic electrodes from the thermolyzed asphalt reaction. *RSC Advances* **2013**, *3*, 2379.

6. Gyan, I.O.; Cheng, I.F. Electrochemical study of biologically relevant molecules at electrodes constructed from GUITAR, a new carbon allotrope. *Microchemical Journal* **2015**, *122*, 39–44.

7. Kabir, H.; Gyan, I.; Foutch, J.; Zhu, H.; Cheng, I. Application of GUITAR on the Negative Electrode of the Vanadium Redox Flow Battery: Improved V3+/2+ Heterogeneous Electron Transfer with Reduced Hydrogen Gassing. *Journal of Carbon Research* **2016**, *2*, 13.

8. Morgan, M. Electrical conduction in amorphous carbon films. *Thin Solid Films* **1971**, *7*, 313–323.

9. Hauser, J.J. Hopping conductivity in amorphous carbon films. *Solid State Communications* **1975**, *17*, 1577–1580.

10. Romanenko, A.I.; Anikeeva, O.B.; Okotrub, A.V.; Kuznetsov, V.L.; Butenko, Y.V.; Chuvilin, A.L.; Dong, C.; Ni, Y. Temperature Dependence of Electroresistivity, Negative and Positive Magnetoresistivity of Graphite/Diamond Nanocomposites and Onion-Like Carbon. *MRS Proceedings* **2001**, *703*, 259–264.

11. Powell, R.W.; Schofield, F.H. The thermal and electrical conductivities of carbon and graphite to high temperatures. *Proceedings of the Physical Society* **1939**, *51*, 153–172.

12. Buerschaper, R.A. Thermal and Electrical Conductivity of Graphite and Carbon at Low Temperatures. *Journal of Applied Physics* **1944**, *15*, 452–454.

13. Smith, A.W.; Rasor, N.S. Observed Dependence of the Low-Temperature Thermal and Electrical Conductivity of Graphite on Temperature, Type, Neutron Irradiation, and Bromination. *Physical Review* **1956**, *104*, 885–891.

14. Mal'tseva, L.F.; Marmer, É.N. Determination of the electrical properties of graphite at high temperatures. *Soviet Powder Metallurgy and Metal Ceramics* **1962**, *1*, 34–38.

15. Adkins, C.J.; Freake, S.M.; Hamilton, E.M. Electrical conduction in amorphous carbon. *Philosophical Magazine* **1970**, *22*, 183–188.

16. Matsubara, K.; Sugihara, K.; Tsuzuku, T. Electrical resistance in the *c* direction of graphite. *Physical Review B* **1990**, *41*, 969–974.

17. Sun, Y.; Wang, C.; Pan, L.; Fu, X.; Yin, P.; Zou, H. Electrical conductivity of single polycrystalline-amorphous carbon nanocoils. *Carbon* **2016**, *98*, 285–290.

18. Ma, H.; Nakata, K.; Pan, L.; Hirahara, K.; Nakayama, Y. Relationship between the structure of carbon nanocoils and their electrical property. *Carbon* **2014**, *73*, 71–77.

19. Fujii, M.; Matsui, M.; Motojima, S.; Hishikawa, Y. Magnetoresistance in carbon micro-coils annealed at various temperatures. *Journal of Crystal Growth* **2002**, *237*, 1937–1941.

20. Tyler, W.W.; Wilson, A.C. Thermal Conductivity, Electrical Resistivity, and Thermoelectric Power of Graphite. *Physical Review* **1953**, *89*, 870–875.

21. Knight, D.S.; White, W.B. Characterization of diamond films by Raman spectroscopy. *Journal of Materials Research* **1989**, *4*, 385–393.

22. Tuinstra, F.; Koenig, J.L. Raman Spectrum of Graphite. *The Journal of Chemical Physics* **1970**, *53*, 1126–1130.

23. Nemanich, R.J.; Solin, S.A. First-and second-order Raman scattering from finite-size crystals of graphite. *Physical Review B* **1979**, *20*, 392.

24. Lespade, P.; Al-Jishi, R.; Dresselhaus, M.S. Model for Raman scattering from incompletely graphitized carbons. *Carbon* **1982**, *20*, 427–431.

25. Wada, N.; Gaczi, P.J.; Solin, S.A. "Diamond-like" 3-fold coordinated amorphous carbon. *Journal of Non-Crystalline Solids* **1980**, *35*, 543–548.

26. Dillon, R.O.; Woollam, J.A.; Katkanant, V. Use of Raman scattering to investigate disorder and crystallite formation in as-deposited and annealed carbon films. *Physical Review B* **1984**, *29*, 3482.

27. Yoshikawa, M.; Nagai, N.; Matsuki, M.; Fukuda, H.; Katagiri, G.; Ishida, H.; Ishitani, A.; Nagai, I. Raman scattering from sp2 carbon clusters. *Physical Review B* **1992**, *46*, 7169.

28. Wagner, J.; Ramsteiner, M.; Wild, C.; Koidl, P. Resonant Raman scattering of amorphous carbon and polycrystalline diamond films. *Physical Review B* **1989**, *40*, 1817.

29. Schwan, J.; Ulrich, S.; Batori, V.; Ehrhardt, H.; Silva, S.R.P. Raman spectroscopy on amorphous carbon films. *Journal of Applied Physics* **1996**, *80*, 440–447.

30. Wojcik, P.M.; Bakharev, P.V.; Corti, G.; McIlroy, D.N. Nucleation, evolution, and growth dynamics of amorphous silica nanosprings. *Materials Research Express* **2017**, *4*, 015004.

31. Wang, L.; Major, D.; Paga, P.; Zhang, D.; Norton, M.G.; McIlroy, D.N. High yield synthesis and lithography of silica-based nanospring mats. *Nanotechnology* **2006**, *17*, S298–S303.

32. Corti, G.; Brown, J.; Rajabi, N.; McIlroy, D.N. Threefold growth efficiency improvement of silica nanosprings by using silica nanosprings as a substrate. *Nanotechnology* **2018**, *29*, 115604.

33. Xie, Y.; McAllister, S.D.; Hyde, S.A.; Sundararajan, J.P.; FouetioKengne, B.A.; McIlroy, D.N.; Cheng, I.F. Sulfur as an important co-factor in the formation of multilayer graphene in the thermolyzed asphalt reaction. *Journal of Materials Chemistry* **2012**, *22*, 5723.

34. Ferrari, A.C.; Robertson, J. Interpretation of Raman spectra of disordered and amorphous carbon. *Physical review B* **2000**, *61*, 14095.

35. Gruen, D.M. Nanocrystalline diamond films. *Annual Review of Materials Science* **1999**, *29*, 211–259.

36. Zhou, D.; Gruen, D.M.; Qin, L.C.; McCauley, T.G.; Krauss, A.R. Control of diamond film microstructure by Ar additions to CH4/H2 microwave plasmas. *Journal of Applied Physics* **1998**, *84*, 1981–1989.

37. Nemanich, R.J.; Glass, J.T.; Lucovsky, G.; Shroder, R.E. Raman scattering characterization of carbon bonding in diamond and diamondlike thin films. *Journal of Vacuum Science & Technology A: Vacuum, Surfaces, and Films* **1988**, *6*, 1783–1787.

38. Shroder, R.E.; Nemanich, R.J.; Glass, J.T. Analysis of the composite structures in diamond thin films by Raman spectroscopy. *Physical Review B* **1990**, *41*, 3738.

39. Ferrari, A.C.; Robertson, J. Origin of the 1150 cm−1 Raman mode in nanocrystalline diamond. *Physical Review B* **2001**, *63*, 121405.

40. Ferrari, A.C.; Basko, D.M. Raman spectroscopy as a versatile tool for studying the properties of graphene. *Nature Nanotechnology* **2013**, *8*, 235–246.

41. Martins Ferreira, E.H.; Moutinho, M.V.O.; Stavale, F.; Lucchese, M.M.; Capaz, R.B.; Achete, C.A.; Jorio, A. Evolution of the Raman spectra from single-, few-, and many-layer graphene with increasing disorder. *Physical Review B* **2010**, *82*, 125429.

42. Pócsik, I.; Hundhausen, M.; Koós, M.; Ley, L. Origin of the D peak in the Raman spectrum of microcrystalline graphite. *Journal of Non-Crystalline Solids* **1998**, *227–230*, 1083–1086.

43. Ferrari, A.C.; Robertson, J. Resonant Raman spectroscopy of disordered, amorphous, and diamondlike carbon. *Physical Review B* **2001**, *64*, 075414.

44. Matthews, M.J.; Pimenta, M.A.; Dresselhaus, G.; Dresselhaus, M.S.; Endo, M. Origin of dispersive effects of the Raman D band in carbon materials. *Physical Review B* **1999**, *59*, R6585.

45. Inagaki, M. Discussion of the formation of nanometric texture in spherical carbon bodies. *Carbon* **1997**, *35*, 711–713.

46. Serp, P.; Feurer, R.; Kalck, P.; Kihn, Y.; Faria, J.L.; Figueiredo, J.L. A chemical vapour deposition process for the production of carbon nanospheres. *Carbon* **2001**, *39*, 621–626.

47. Kang, Z.C.; Wang, Z.L. On accretion of nanosize carbon spheres. *The Journal of Physical Chemistry* **1996**, *100*, 5163–5165.

48. Kang, Z.C.; Wang, Z.L. Chemical activities of graphitic carbon spheres. *Journal of molecular catalysis A: Chemical* **1997**, *118*, 215–222.

49. Qian, H.; Han, F.; Zhang, B.; Guo, Y.; Yue, J.; Peng, B. Non-catalytic CVD preparation of carbon spheres with a specific size. *Carbon* **2004**, *42*, 761–766.

50. Jin, Y.Z.; Gao, C.; Hsu, W.K.; Zhu, Y.; Huczko, A.; Bystrzejewski, M.; Roe, M.; Lee, C.Y.; Acquah, S.; Kroto, H.; et al. Large-scale synthesis and characterization of carbon spheres prepared by direct pyrolysis of hydrocarbons. *Carbon* **2005**, *43*, 1944–1953.

51. Nieto-Márquez, A.; Valverde, J.L.; Keane, M.A. Selective low temperature synthesis of carbon nanospheres via the catalytic decomposition of trichloroethylene. *Applied Catalysis A: General* **2009**, *352*, 159–170.

52. Zhang, Y.; Yang, W.; Luo, R.; Shang, H. Preparation of carbon nanospheres by non-catalytic chemical vapor deposition and their formation mechanism. *New Carbon Materials* **2016**, *31*, 467–474.

53. Venugopal, A.; Pirkle, A.; Wallace, R.M.; Colombo, L.; Vogel, E.M.; Secula, E.M.; Seiler, D.G.; Khosla, R.P.; Herr, D.; Michael Garner, C.; et al. Contact Resistance Studies of Metal on HOPG and Graphene Stacks.; AIP Conference Proceedings, 2009; Vol. 1173, pp. 324–327.

54. Anteroinen, J.; Kim, W.; Stadius, K.; Riikonen, J.; Lipsanen, H.; Ryynanen, J. Extraction of graphene-titanium contact resistances using transfer length measurement and a curve-fit method. *International Journal of Materials and Metallurgical Engineering* **2012**, *6*, 801–804.

55. Zeiger, M.; Jäckel, N.; Mochalin, V.N.; Presser, V. Review: carbon onions for electrochemical energy storage. *Journal of Materials Chemistry A* **2016**, *4*, 3172–3196.

56. Liu, M. Coating Technology of Nuclear Fuel Kernels: A Multiscale View. In *Modern Surface Engineering Treatments*; Aliofkhazraei, M., Ed.; IntechOpen: London, UK, 2013; ISBN 978-953-51-1149-8.

57. Pawlyta, M.; Hercman, H. Transmission electron microscopy (TEM) as a tool for identification of combustion products: application to black layers in speleothems. *Annales Societatis Geologorum Poloniae* **2016**, *86*, 237–248.

58. Buseck, P.R.; Adachi, K.; Gelencsér, A.; Tompa, É.; Pósfai, M. Ns-Soot: A Material-Based Term for Strongly Light-Absorbing Carbonaceous Particles. *Aerosol Science and Technology* **2014**, *48*, 777–788.

CHAPTER 4

The Effects of Sub-Bandgap Transitions and the Defect Density of States on the Photocurrent Response of a Single ZnO-Coated Silica Nanospring

Peter M. Wojcik, Lyndon D. Bastatas, Negar Rajabi, Pavel V. Bakharev,
and David N. McIlroy

The electrical and optoelectronic properties of nanometer-sized ZnO structures are highly influenced by its native point defects. Understanding and controlling these defects are essential for the development of high-performance ZnO-based devices. Here, an electrical device consisting of a polycrystalline ZnO-coated silica nanospring was fabricated and used to characterize the electrical and photoconductive properties of the ZnO layer using near-ultraviolet (405 nm) and sub-bandgap (532 and 633 nm) excitation sources. We observe a photocurrent response with all three wavelengths and notably with 532 nm green illumination, which is the energy associated with deep oxygen vacancies. The polycrystalline ZnO-coated silica nanospring exhibits a high responsivity of 1740 A W^{-1} with the 405 nm excitation source. Physical models are presented to describe the photocurrent rise and decay behavior of each excitation source where we suggest that the rise and decay characteristics are highly dependent on the energy of the excitation source and the trapping of electrons and holes in intermediate defect levels in the bandgap. The energy levels of the trap depths were determined from the photoconductive decay data and are matched to the reported energy levels of singly and doubly ionized oxygen vacancies. A phenomenological model to describe the dependence of the saturation photocurrent on excitation intensity is presented in order to understand the characteristics of the observed breaks in the slopes of the saturation photocurrent versus excitation intensity profile.

4.1 Author's Note

Most of the material presented in this chapter has been published in *Nanotechnology* **2021**, *32*, 035202 [1]. Additional information that does not appear in the journal publication has been included in the main body of the text to provide a more thorough examination of the topic. If the reader would like to cite the work presented in this chapter, we refer them to the published journal article.

4.2 Introduction

ZnO has a direct wide bandgap (3.37 eV) and a large exciton binding energy at room temperature (60 meV), which make it an excellent semiconducting candidate for a variety of applications, including ultraviolet (UV) photodetection [2–6], solar energy conversion [7, 8],

chemical sensing [9–12], light emitting diodes [13, 14], and piezoelectric nanogenerators [15]. ZnO is also one of the most promising metal oxide semiconducting materials for photodetection applications due to its non-toxicity, low cost, ability to be easily synthesized [16], and high electron mobility [8]. Many of the aforementioned studies link ZnO's wide bandgap with UV applications; however, applications such as those used for solar energy conversion require a wide spectral response with photodetection sensitivity in the visible light region. Tuning a pristine one-dimensional ZnO nanowire (NW) photodetector to the visible spectrum has been achieved by surface functionalization with gold nanoparticles [17] and carbon nanodots [18], by doping with Cu [19] and Mn [20], and by creating a core–shell structure consisting of a ZnO NW core and Zn-rich ZnO shell [21]. A visible response has also been observed in ZnO epilayers [22], polycrystalline ZnO [23], ZnO nanocones [24], and thin-film ZnO [5], all of which include a variety of native point defects (NPDs) in the bandgap such as oxygen and zinc vacancies, and zinc interstitials. Successful control of the NPD density in ZnO nanostructures has been achieved through doping, modifying growth conditions [25], and annealing [23, 24]. The high surface-area-to-volume ratio of ZnO-based nano-architectures, which is vital to the performance of the many applications of ZnO, is also greatly affected by a strong sensitivity to these NPDs. Understanding and controlling of NPDs and how they affect the electrical and optoelectronic properties of ZnO nanostructures is therefore paramount for the optimization of ZnO-based device architectures.

NPDs have been extensively studied via photoluminescence, which has given evidence for an abundance of deep and shallow defect levels arising from several prominent emissions in the red, orange, green, and violet [5, 24, 26–30]. The green emission has been thoroughly reported [24, 26–29], however its origins are still controversial due to the complexity of the analyzation of the photoluminescence spectra arising from the multiple possible donor–acceptor combinations that can match experimental photoluminescence energies. Identifying the origin of the green emission energy level is further complicated by variations in the theoretically calculated depths of the NPD energy levels [31, 32]. The sub-bandgap photocurrent response of a variety of unmodified ZnO structures has been reported [5, 22–24, 28, 33–40]; however, only approximately half of these studies have reported a photocurrent response with green light [5, 24, 28, 33, 36, 38, 39], and even fewer present models for photocurrent generation and recombination from green and other

sub-bandgap illumination sources. The dependence of the saturation photocurrent on excitation intensity has also been reported for ZnO-based materials [2, 3, 20, 34, 41–43]. However, to the best of our knowledge, no phenomenological model exists to explain the observed breaks in the slope of the saturation photocurrent versus excitation intensity profile for ZnO.

Here, we report on the electrical and photoconductive properties of a thin ~70 nm polycrystalline ZnO coating on a silica nanospring (SNS) to study how near-UV (405 nm) and sub-bandgap (532 and 633 nm) excitation affects the photocurrent rise and decay response, responsivity, and the excitation intensity dependence of the saturation photocurrent. We observe that the polycrystalline ZnO-coated SNS (ZnO–SNS) exhibits a typical two-step fast and slow rise and decay photocurrent behavior. Despite the two-step rise and decay processes having been well documented in previous literature, there is much debate concerning the predominant underlying physical processes used to describe the rise and decay photocurrent behavior observed for ZnO-based photodetectors [5, 22, 33, 36, 37, 39, 44–50]. It is well known, however, that these photoconductive properties are highly dependent on NPDs and their corresponding energy levels within the bandgap [5, 22–24, 33, 37, 46, 48]. We first provide a review of these NPDs and their interactions with external atmospheric conditions, their behavior as electron (hole) traps, and their sources of sub-bandgap photocurrent generation. We then present physical models to describe the near-UV and sub-bandgap photocurrent rise and decay behavior observed in our experiments. The physical models show that the observed differences in the rate of change in the rise and decay of the photocurrent for each excitation source is highly dependent on the excitation wavelength and the trapping of carriers within the bandgap. Finally, we present a phenomenological model to explain the observed breaks in the slope of the saturation photocurrent versus excitation intensity profile. These results provide a better understanding of the visible photocurrent response in ZnO, which is critical for the advancement of ZnO-based devices and applications that require them to have a wide spectral response.

4.3   Experimental Methods

4.3.1   Silica Nanospring Growth

SNSs were grown on Si/SiO$_2$ (500 nm thermal oxide) substrates using a modified chemical vapor deposition process described in chapter 2, and by Wojcik et al. [51] and Wang et al. [52]. The SNS growth time for the samples used in this study was ~10–15 min.

4.3.2   ZnO Deposition

Following SNS growth, a thin ~70 nm coating of ZnO was applied to the SNS surface using a custom-built atomic layer deposition (ALD) system [10, 11, 53]. The system consisted of a tube furnace acting as the reaction chamber, which was operated at 170 °C and used the precursors diethyl zinc (DEZn) and deionized water (DI) as sources of zinc and oxygen, respectively. The ALD cycle began with the system under vacuum at a base pressure of ~400 mTorr. A 250 ms pulse of DEZn into a 6 sccm flow of Ar pressurized the system to ~2 Torr. The system was then purged for 2 s with Ar and subsequently returned to the base pressure. An identical cycle was repeated, except for DI in lieu of DEZn, completing the full ALD cycle. The pressurization of the reaction chamber during the DEZn and DI pulses facilitates diffusion into the mat of SNSs. A typical ALD process consisted of 150 cycles and produced an average ZnO thickness of ~70 nm [10, 53].

4.3.3   Device Fabrication

The single ZnO–SNS electrical device fabrication process was the same as described in section 3.3.3 of chapter 3, except ZnO–SNSs were used in lieu of GUITAR-coated SNSs. Figure 4.1 shows a representation of the interdigitated electrode design and a false-color scanning electron microscopy (SEM) image of the single ZnO–SNS device used in the experiments. The single ZnO–SNS device was annealed in a tube furnace at temperatures of 300 °C and 400 °C while continually flowing Ar at a rate of 50 sccm to improve the electrical conductivity between the ZnO–SNS and the contacts. The furnace was ramped to the final anneal temperature in 15 min then shut off and allowed to cool for several hours to ~50 °C. The un-annealed and annealed device at 300 °C both displayed current–voltage

curves in the dark that were characteristic of a Schottky barrier. Annealing at 400 °C produced an Ohmic response, which is discussed in section 4.6.1.
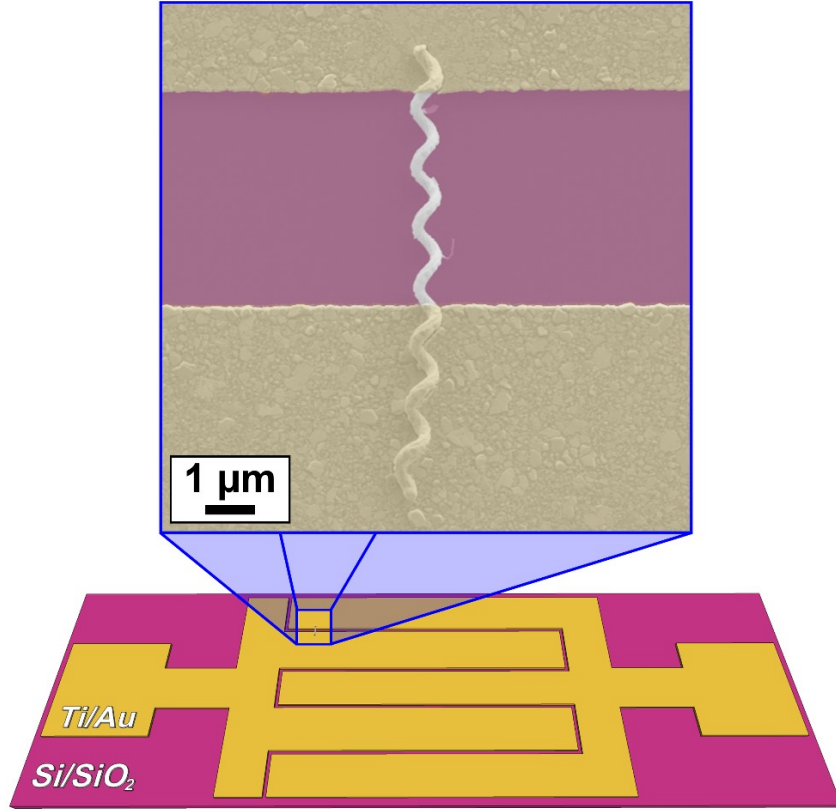
Figure 4.1 Interdigitated electrode design and false-color SEM image of the single ZnO–SNS device used in the experiments.

4.3.4 Electrical and Optoelectronic Characterization

Figure 4.2 shows a schematic diagram of the experimental setup that was used for the electrical and optoelectronic characterization of the single ZnO–SNS device. Electrical measurements were acquired with a Keithley Model 2400 (Tektronix, Beaverton, OR, USA) using a two-point probe method with two micromanipulators (Micromanipulator Model 110 with Model 7A probe tip, The Micromanipulator Co., Carson City, NV, USA). The single ZnO–SNS device was placed on an Olympus BX51 (Olympus Corp., Center Valley, PA, USA) microscope stage and illuminated with 633 nm HeNe (Melles Griot Model 05-LHR-927, IDEX Health and Sciences, Rochester, NY, USA), 532 nm (AixiZ Model AD-532-25ADJ, AixiZ, Houston, TX, USA), and 405 nm (AixiZ Model AH405-201230,

AixiZ, Houston, TX, USA) excitation sources, which were focused on the ZnO–SNS with a 10× microscope objective producing a spot size of ~300 μm. The laser intensity was controlled with a circular linear variable neutral density filter (Newport Model 50FS04DV.4, Newport Corp., Irvine, CA, USA) and measured at the sample with a Si photodetector (Thorlabs Model PDA36A, Thorlabs, Newton, NJ, USA). All electrical and optoelectronic measurements were performed at room temperature and atmospheric pressure.
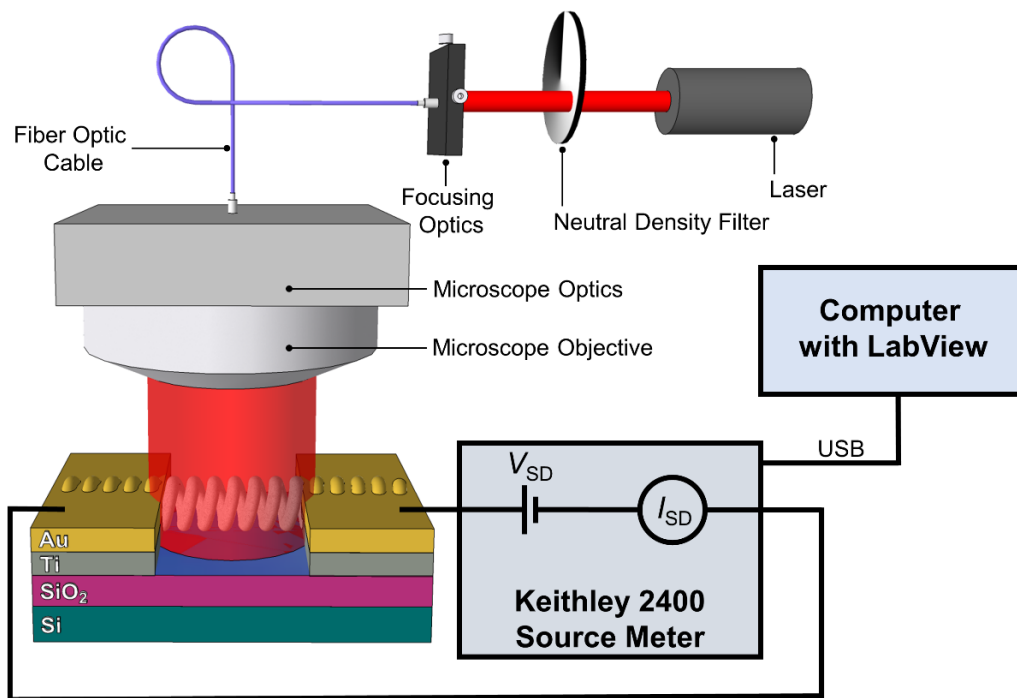
Figure 4.2 Schematic diagram of the experimental setup used for the electrical and optoelectronic characterization of the single ZnO–SNS device.

4.3.5 Microscopy Equipment

SEM images were obtained with a Zeiss Supra 35 scanning electron microscope (Zeiss, Peabody, MA, USA).

4.3.6 ZnO Structural Characterization

The crystal structure of the polycrystalline ZnO coating was characterized with a Siemens x-ray diffractometer D5000 (Siemens, Munich, Germany) using the Cu K_α line and 2° steps ($\lambda = 1.54$ Å).

4.4 Background on Defects, and Photoconduction and Recombination Mechanisms in ZnO

The UV and sub-bandgap photocurrent response of ZnO is more complex than a typical band-to-band photocurrent response because of the characteristic long rise and decay behavior which are indicative of long electron lifetimes arising from photocurrent generation and recombination processes due to the various NPD types and their corresponding energy levels within the bandgap of ZnO. Typically, a two-step fast and slow rise and decay photocurrent behavior is observed for ZnO; however, there is still much debate concerning the predominant underlying physical processes used to describe these photocurrent behaviors that have been well documented in previous literature [5, 22, 33, 36, 37, 39, 44–50]. Furthermore, the literature remains a tangled web of information regarding these photocurrent behaviors. Therefore, we present the following review of NPDs, and photoconduction and recombination mechanisms in ZnO to elucidate the many photoconduction and recombination mechanisms which have been documented in literature, and to provide a foundation for understanding how NPD interactions with external atmospheric conditions, behavior as electron or hole traps, and sources of photocurrent generation can be used to describe the fast and slow rise and decay photoconductive behavior in our proposed physical models.

There are four main types of NPDs in ZnO: oxygen vacancies (V_o), zinc vacancies (V_{Zn}), zinc and oxygen interstitials (Zn_i, O_i), and antisites [24, 54]. Oxygen vacancies and zinc interstitials create donor levels, and the zinc vacancy is an acceptor level [24, 55]. Oxygen and zinc vacancies are considered to be the most predominant defects in ZnO [24, 56]. Theoretical studies have shown that the oxygen vacancy is actually a deep double donor, contrary to the notion that it created an abundant free-electron density and was responsible for the dominant n-type conductivity observed for ZnO [57]. Photoluminescence, electroluminescence, and density functional theory studies have shown that the neutral oxygen vacancy (V_o^0) lies ~0.9–1.65 eV above the valence band (VB) edge [31, 58, 59], while its singly (V_o^+) and doubly (V_o^{++}) charged oxidation states have been reported to lie ~0.9–2.5 eV [5, 26–28] and ~2.25 eV [24] above the VB edge, respectively. The zinc vacancy has three possible charge states: V_{Zn}^0, V_{Zn}^-, and V_{Zn}^{--} [32, 55], which are reported to

lie ~0.3 eV [60], ~0.7 eV [30], and ~2.8 eV [30] above the VB edge, respectively. The zinc interstitial is a shallow double donor which lies ~3.18 eV (~0.22 eV) above the VB (below the conduction band (CB)) [29, 59], and the oxygen interstitial has been reported to lie ~0.9 eV above the VB [28, 61]. The reported energy levels for a variety of NPDs in ZnO are shown in Figure 4.3(a). The distances in eV from the CB (VB) are shown above their respective NPD type as reported from literature. The wide range in reported values of the various NPD energy levels is due, in part, to the complexity of the analyzation of photoluminescence spectra arising from the numerous acceptor–donor combinations that can match experimental photoluminescence energies, and is exacerbated by the variations of the theoretically calculated defect energy levels as shown in Figure 4.3(a) and in the band diagram included in an article by Tam et al. [62].
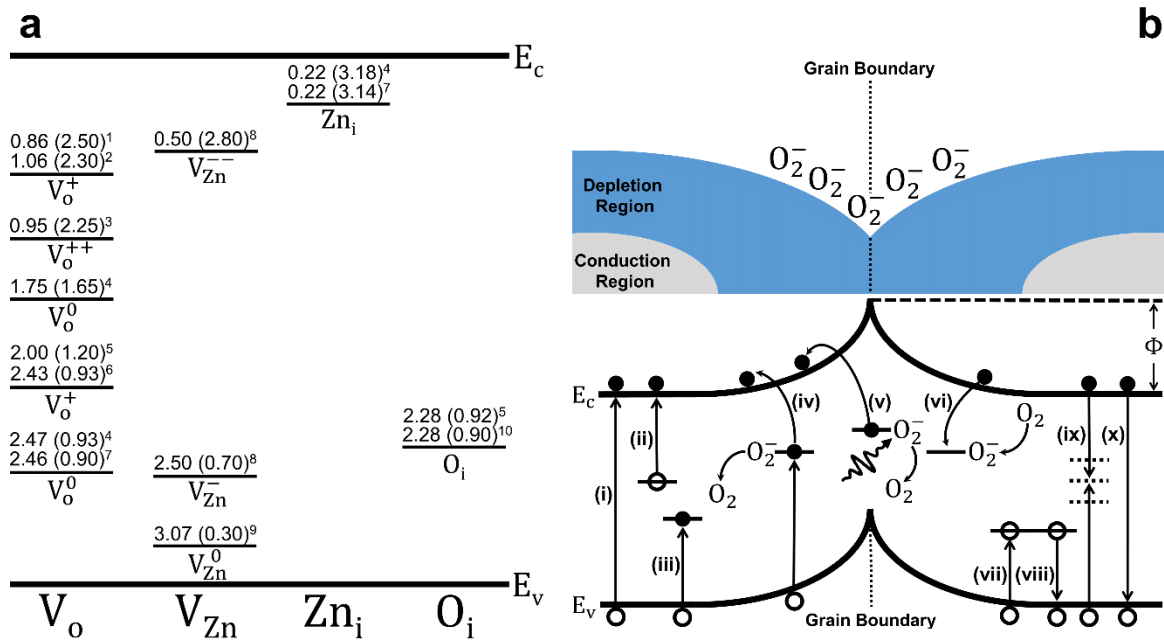
Figure 4.3 (**a**) The reported energy levels of various NPDs in ZnO: (1) [26], (2) [27], (3) [24], (4) [59], (5) [28], (6) [5], (7) [29], (8) [30], (9) [60], (10) [61]. (**b**) A schematic representation of two adjacent ZnO crystals showing the conduction and depletion regions, and the high density of adsorbed oxygen near the grain boundary. Below is the matching band diagram showing the photoconduction and recombination mechanisms in polycrystalline ZnO: electron–hole pair generation via (i) band-to-band, (ii) defect level to CB, and (iii) VB to defect level. Oxygen desorption via (iv) hole capture, and (v) a photon-assisted molecule desorption mechanism. (vi) Oxygen adsorption. Hole (vii) capture and (viii) release to and from a defect state. Electron–hole recombination (ix) at a recombination center and (x) via band-to-band recombination.

It is well known that in the dark, free electrons from ZnO are captured by the adsorption of oxygen on the ZnO surface, which induces an upward band bending, forming a low conductivity depletion region on the surface of a NW [36, 37, 44, 46–48]. In the case of polycrystalline ZnO, a depletion region is formed at the grain boundary between two adjacent crystals. Grain boundaries of polycrystalline ZnO have been shown to contain a higher density of defects compared to grain centers, and grain boundaries host the numerous defect sites that are responsible for the adsorption of oxygen molecules [33]. According to density functional theory, a dissociative chemisorption of atmospheric oxygen occurs at the oxygen vacancy defect site of ZnO by filling the vacant oxygen site with one atomic oxygen [63]. Physisorption was also found to occur on the surface of defect-free ZnO, however, because of the abundance of oxygen vacancies in ZnO, oxygen vacancy defect sites were found to be the more favored adsorption sites for oxygen [63]. These results suggest that chemisorption is preferred over physisorption, and that chemisorption of atmospheric oxygen occurs at oxygen vacancy defect sites that are abundant on the structurally disordered grain boundaries of polycrystalline ZnO.

Figure 4.3(b) is a schematic representation showing two adjacent ZnO nanocrystals displaying the grain boundary, with a corresponding band diagram and upward band bending induced by the adsorption of atmospheric oxygen to the high density of oxygen vacancy defect sites on the structurally disordered grain boundary. The potential barrier formed by the adsorption of atmospheric oxygen on the grain boundary gives rise to a conduction and depletion region allowing for the separation of electrons and/or holes during illumination with UV and sub-bandgap excitation sources. Typically, the initial rapid rise in ZnO photocurrent is attributed to band-to-band excitations of electron–hole pairs in the case of UV excitation [4, 46, 64], and to excitations of electron–hole pairs arising from optical transitions between defect states and the CB in the case of sub-bandgap illumination [22, 24, 65]. In the former case, holes are swept to the grain boundary via the built-in potential; in the latter, holes are trapped in defect levels lying within the bandgap. In both cases, the separation of photogenerated holes and electrons increases the electron lifetime, as they are unlikely to recombine with holes. The result is a rapid increase in photocurrent. Sub-bandgap illumination can also excite electrons from the VB to a defect level lying within the bandgap [24, 33]. Here, holes are created in the VB, and the excited electrons that

are confined to the defect level do not significantly contribute to the total conductivity. In this case, an increase in conductivity is attributed to a mechanism by which holes swept to the surface via the potential gradient release adsorbed oxygen through an electron–hole recombination mechanism to remove oxygen from the surface (oxygen desorption), thereby releasing trapped electrons which are then able to contribute to the conductivity [33]. These three electron–hole pair generation mechanisms for UV and sub-bandgap excitation are shown in Figure 4.3(b) and labeled as processes (i)–(iii). The oxygen desorption mechanism is labeled as process (iv) in Figure 4.3(b). A significant photocurrent response is also suggested to occur via a photon-assisted molecule desorption (PAMD) mechanism, where surface adsorbed oxygen is desorbed via sub-bandgap excitation on the surface of ZnO NWs [36, 37] and V_2O_5 NWs [66]. It is well known that the activation energy for the desorption of chemically adsorbed oxygen from ZnO is ~1.0 eV [67]. In the PAMD mechanism, oxygen is desorbed from the surface via an excitation energy greater than the activation energy for oxygen desorption, thereby releasing trapped electrons into the CB. The PAMD mechanism is labeled as process (v) in Figure 4.3(b). In all the aforementioned photocurrent generation mechanisms, the accumulation of holes on the grain boundary and the removal of oxygen from the surface reduce the barrier height, which further increases conductivity and contributes to the observed initial fast rise in photocurrent.

Following the rapid rise is a slow rise in photocurrent which has been attributed to the competition between the oxygen-related adsorption and desorption mechanisms [37, 47, 48]. Oxygen can be desorbed via the hole-release mechanism and/or the PAMD mechanism. In both desorption mechanisms, trapped electrons are released, contributing to the conductivity. Competing with the oxygen desorption processes is the adsorption of oxygen that traps electrons from the CB and the recombination of electrons and holes at recombination centers, where both processes decrease the conductivity. Ultimately, the combination of these processes results in a slow increase in photocurrent that eventually saturates when the generation and recombination rates reach a steady state. The rate of the slow rise in photocurrent is affected by the concentration of atmospheric oxygen [36, 37, 48, 68], further suggesting that the slow photocurrent rise response is dominated by the competition between the oxygen related adsorption and desorption mechanisms.

The initial rapid decay of photocurrent following termination of illumination has been attributed to the recombination of electrons and holes via band-to-band recombination [22, 44, 45], and via trap-assisted (Shockley–Read–Hall) recombination [22, 69]. The radiative portion of these recombination processes can be examined with photoluminescence spectra and time-resolved photoluminescence transients that occur on the order of ~ns following termination of illumination [22]. The initial rapid decay of the photocurrent has also been attributed to a process by which photo-desorbed oxygen in the bulk of polycrystalline ZnO is quickly re-chemisorbed after termination of the illumination source [43]. In this case, the majority of the chemisorbed oxygen is assumed to be in the bulk of the material, where it is not able to be heavily influenced by external oxygen concentrations [43]. The low barrier height at the termination of illumination also facilitates the re-adsorption of oxygen on the surface where electrons in the CB can more easily overcome a relatively low energy barrier, resulting in a quick reduction of the photocurrent.

There are two primary models that have been used to describe the slow photocurrent decay process, which can exhibit a long decay on the order of hours or days and is typically referred to as a persistent photoconductivity [22, 34–37, 39, 41, 46–49, 70–73]. The first model attributes the slow portion of the photocurrent decay to the competition between the oxygen adsorption and desorption mechanisms [36, 46, 48, 68]. The other model attributes this slow decay to a process by which oxygen vacancies are excited to a metastable state following a lattice relaxation where the recapture of electrons in the metastable state is prohibited via a thermally activated barrier [74]. In the former case involving the competition between the oxygen adsorption and desorption mechanisms, band bending at the grain boundary is increased as oxygen is re-adsorbed on the surface, which decreases the probability for an electron to overcome the increased energy barrier. Simultaneously, holes swept to the grain boundary via the potential gradient release adsorbed oxygen on the surface, freeing electrons that then contribute to the conductivity. The competition of the oxygen adsorption and desorption mechanisms results in the slow decrease in the photocurrent. The rate of decay for the slow portion of the photocurrent has been shown to be highly dependent on atmospheric conditions, namely oxygen concentration, suggesting that the surface-related oxygen adsorption and desorption mechanisms are the dominant processes responsible for the slow photocurrent decay [36, 37, 47, 48, 68, 71]. The effects of

the slow surface-related oxygen adsorption and desorption mechanisms on the photocurrent decay are also confirmed with studies of photocurrent decay of ZnO with passivated samples [22, 46, 75]. Here, the surface passivation of ZnO inhibits the oxygen-related adsorption and desorption mechanisms, leading to an increased rate of photocurrent relaxation. An additional mechanism giving rise to the slow decay of photocurrent involves the trapping and subsequent emission of electrons and/or holes to and from deep defect levels within the bandgap [22]. A NPD behaving as a hole trap repels electrons and has a small electron capture cross section resulting from a negative charge when the hole trap is filled with a hole [22]. Therefore, in contrast to recombination centers, NPDs exhibit slow electron–hole recombination because holes are typically thermally emitted into the VB before recombination with an electron to desorb oxygen, recombination at a recombination center, or re-trapped in another NPD hole trap. These hole trapping and photocurrent generation and recombination mechanisms, and how they affect the photocurrent rise and decay will be further discussed in detail in the following sections, which present physical models to describe the near-UV and sub-bandgap photocurrent rise and decay responses observed in our experiments.

4.5 Single ZnO-Coated Silica Nanospring Device and ZnO Structure

Figure 4.4(a) shows a false-color SEM image of the single ZnO–SNS device that was used in our experiments. The single ZnO–SNS spans a ~5 μm long gap between two Ti/Au electrical contacts forming the source–drain electrodes. The inset in Figure 4.4(a) is an SEM image of the ZnO–SNS surface and shows the uniformly distributed polycrystalline ZnO coating which has an average particle size of ~20 nm. The ZnO ALD process used to coat the SNS produces a uniform ~70 nm thick ZnO layer on the surface of the SNS [11, 53] and has been demonstrated to be advantageous over other deposition methods, such as chemical vapor deposition, as it allows the user to control the thickness of the coating, the size of the ZnO nanocrystals, and the ability to coat intricate three-dimensional (3D) shapes [10, 12]. Control of the ZnO nanocrystalline size is particularly important in the application of ZnO–SNSs used as redox chemical sensors where the ZnO nanocrystalline size was shown to be a significant factor in the response of the sensors when exposed to explosive compounds [12]. The platform for the ZnO coating is a non-conducting SNS. The helical SNS structure

serving as a platform for the ZnO is particularly interesting because of its high surface area compared to a NW of similar dimensions. For example, the SNS with a ~70 nm thick coating of ZnO and 5 μm free length as shown in Figure 4.4(a) has ~5 times more surface area than a 70 nm diameter, 5 μm long ZnO NW.
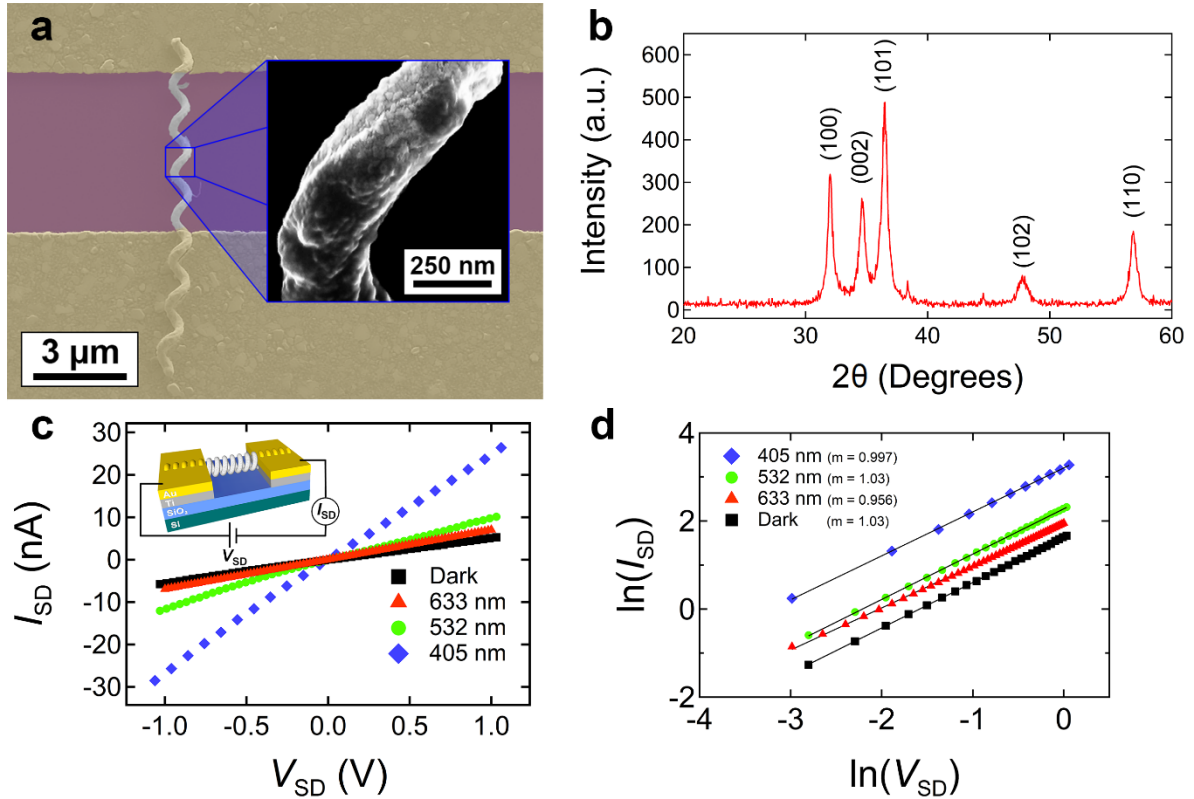
Figure 4.4 (a) False-color SEM image of the single ZnO–SNS device and inset showing the surface morphology of the polycrystalline ZnO coating. (**b**) Powder x-ray diffraction 2θ pattern of ZnO–SNSs. (**c**) Source–drain current–voltage curves of the ZnO–SNS device in the dark and when illuminated with 405, 532, and 633 nm excitation sources. The inset shows a 3D representation of the device with an electrical diagram. (**d**) A ln–ln plot showing the Ohmic behavior of the source–drain current–voltage curves.

The crystalline structure of the ZnO coating was characterized with x-ray diffraction (XRD). Figure 4.4(b) shows the powder XRD pattern of an ensemble of nanocrystalline ZnO–SNS structures collected in the 2θ range of 20°–60°. The diffraction peaks observed at $2\theta = 32.02, 34.55, 36.50, 47.81,$ and 56.87 correspond to lattice planes (100), (002), (101), (102), and (110), respectively, indicating the polycrystalline hexagonal Wurtzite structure of the ZnO [53].

4.6 Photoconductivity

4.6.1 Voltage Dependence of the Photocurrent and ZnO Resistivity

Figure 4.4(c) shows the source–drain current–voltage (I_{SD}–V_{SD}) characteristics of the single ZnO–SNS device under dark conditions and when illuminated with 405, 532, and 633 nm excitation sources. The inset in Figure 4.4(c) shows a 3D representation of the device with an electrical diagram. The excitation intensity measured at the sample was 2 mW cm^{-2} for each illuminated I_{SD}–V_{SD} measurement. Figure 4.4(d) shows a ln–ln plot of the dark and illuminated I_{SD}–V_{SD} characteristics which exhibit an Ohmic response (unity slope), suggesting that there is unimpeded transfer of the majority carriers (electrons) between the Ti/Au–ZnO interface.

The total resistance (R_T) of the single ZnO–SNS device is the sum of the resistance of the ZnO–SNS ($R_{ZnO-SNS}$) and of the two contact resistances attributed to the Ti-Au/ZnO–SNS contacts on each end of the device ($2R_C$): $R_T = R_{ZnO-SNS} + 2R_C$. The specific contact resistance of Ti/Au contacts to ZnO has been studied extensively and reported to be in the range of ~10^{-3} to 10^{-8} Ω cm^2 [76–79]. The estimated contact resistance of our device is small (~20 kΩ), ~4 orders of magnitude lower than the total resistance of the device (~200 MΩ), and therefore can be neglected. The resistivity, ρ, of the device was calculated using

$$\rho = R_{ZnO-SNS}\frac{A}{L}, \qquad (4.1)$$

where A is the cross sectional area of the ZnO coating on the SNS, and L is the length of the ZnO–SNS. The cross sectional area of the ZnO layer was calculated by measuring the wire diameter of the ZnO–SNS via an SEM image and using an estimation of the ZnO thickness (~70 nm) based on previous measurements of the thickness of a ZnO coating deposited on a Si substrate under similar ALD conditions [11, 53]. The helical pitch of individual SNSs are random and varied during the growth process; however, are usually well-defined for micron-long sections of its free length. The well-defined and constant helical pitch of the SNS across the electrode gap was exploited to calculate the length, L, of the ZnO–SNS device. The resistivity of the single ZnO–SNS in the dark was 166 Ω cm, and is in

agreement with previous measurements of the resistivity of thin-film ZnO (~1–1000 Ω cm) [80, 81]. The illuminated resistivities for $\lambda =$ (405, 532, 633) nm were $\rho =$ (34, 83, 125) Ω cm. The largest change in conductance occurs under illumination with the 405 nm excitation source, which is increased by a factor of ~5 compared to the dark conductance.

4.6.2 *Photocurrent Rise and Decay Response*

Figure 4.5 shows the normalized photocurrent response of the single ZnO–SNS device when illuminated with near-UV (405 nm) and sub-bandgap (532 and 633 nm) excitation sources. The inset in Figure 4.5 shows the details of the on/off behavior for the 532 and 633 nm excitation sources. The photocurrent (I_{pc}) was determined by subtracting the dark current (I_d) from the total illuminated current, and we define the normalized photocurrent as the ratio of the photocurrent to the dark current (I_{pc}/I_d). The shaded area represents the 15 min period when the device was illuminated with the respective excitation source. The applied bias was +0.5 V and the intensity of the excitation source was 2 mW cm^{-2} for each photocurrent response measurement. The single ZnO–SNS device was held at a +0.5 V applied bias for ~2 h in the dark to achieve a steady state dark current prior to illumination with each respective excitation source. The photocurrent responses of each excitation source display a typical two-step fast and slow rise and decay behavior. First, there is an initial fast increase followed by a slow increase in photocurrent which takes minutes to hours to saturate; when the illumination source is terminated there is an initial fast decrease followed by a slow decrease in photocurrent which takes hours to return to its initial steady state dark current value.
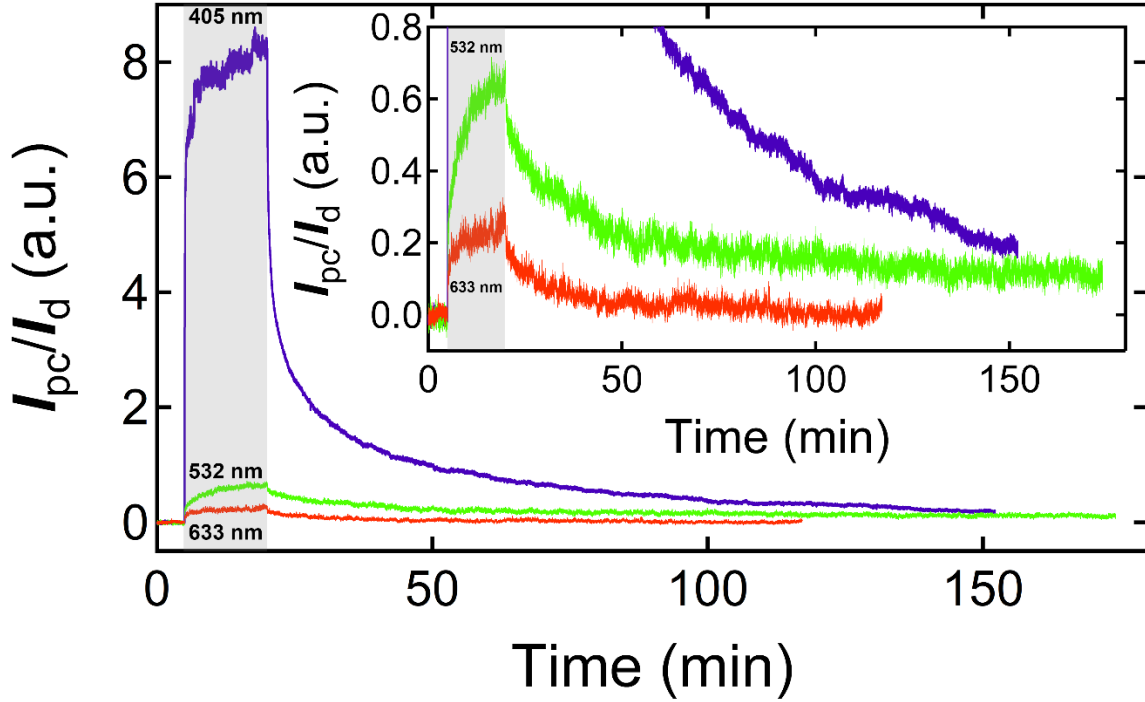
Figure 4.5 The normalized photocurrent response of the single ZnO–SNS device when illuminated with 405, 532, and 633 nm excitation sources and inset showing the details of the on/off behavior for the 532 and 633 nm excitation sources. The shaded area represents the 15 min period when the device was illuminated with the respective excitation source.

4.6.3 Photocurrent Rise Response Analysis

Figure 4.6 shows the details of the fast and slow normalized photocurrent rise response of each excitation source and the corresponding fits and time constants attained with a double exponential function that was used to separately analyze and compare the two-step photocurrent rise response of each excitation source. The shaded area represents the 15 min period when the device was illuminated with the respective excitation source. The normalized photocurrent growth for all three wavelengths was fitted with a double exponential equation of the following form:

$$I_n(t) = A_0 - B_1 e^{-\frac{t-t_0}{\tau_1}} - B_2 e^{-\frac{t-t_0}{\tau_2}}, \tag{4.2}$$

where I_n is the normalized photocurrent (I_{pc}/I_d), A_0, B_1, and B_2 are positive constants, t_0 is the time when the illumination source was turned on, and τ_1 and τ_2 are the fast and slow

time constants, respectively. The time constants attained from the double exponential fits are $\tau_1 = (4.8, 5.5, 12)$ s and $\tau_2 = (300, 251, 2550)$ s for $\lambda = (405, 532, 633)$ nm.
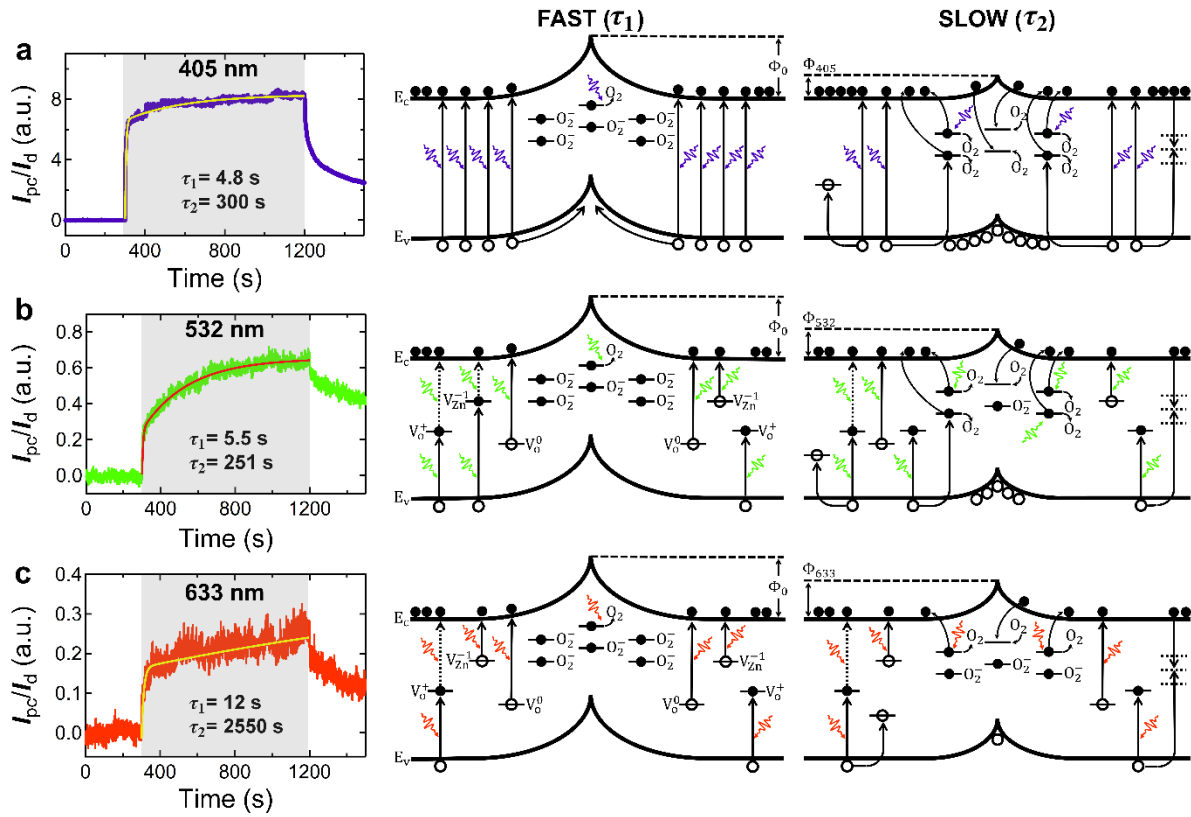
Figure 4.6 The normalized photocurrent rise characteristics of the (**a**) 405 nm, (**b**) 532 nm, and (**c**) 633 nm excitation sources showing double exponential fits and corresponding time constants for photocurrent growth. The shaded areas represent the 15 min period when the device was illuminated with the respective source. Displayed to the right of each photocurrent rise response are the corresponding band diagrams which show the dominant photocurrent generation and recombination mechanisms for the fast and slow photocurrent rise response of each respective excitation source.

There is a strong response to the 405 nm (3.06 eV) near-UV excitation source and the photocurrent increases from I_d by a factor of ~6 in 10 s then slowly increases by an additional factor of ~2 after 15 min. The observed sub-bandgap photocurrent response for the 532 and 633 nm excitation sources suggests that there are an abundance of NPDs in the polycrystalline ZnO [33]. It is well known that the bandgap of bulk defect free ZnO is 3.37 eV; however, a reduction in the bandgap can be achieved with the introduction of oxygen vacancies [82]. Calculations of the density of states for ZnO with an ideal

defect-free Wurtzite structure and for a Wurtzite structure containing 6.25% oxygen vacancies have shown that the bandgaps of these two structures are 3.22 eV and 2.91 eV [82], respectively, and lower than that of bulk defect-free ZnO. The 405 nm photocurrent response is ~13× greater than the photocurrent response of the 532 nm excitation source and ~30× greater than the photocurrent response of the 633 nm excitation source 15 min after illumination. The strong photocurrent response of the 405 nm source cannot be attributed solely to excitations occurring between defect states and the CB. In our photoconductivity measurements, the number of excited carriers is proportional to the excitation energy of the respective source using a constant illumination intensity (2 mW cm^{-2}); therefore, we would expect a proportional increase in the saturation current for the 405, 532, and 633 nm excitation sources if they are exciting transitions from similar defect levels. We observe this proportional increase with the 532 and 633 nm excitation sources, but not with the 405 nm excitation source. A similar proportional increase in photocurrent was observed by Lee et al., who observed a proportional increase of the photocurrent response of ZnO to red, green, and blue illumination sources, and a large disproportionate photocurrent response to UV [83]. Additionally, the non-negligible spectral bandwidth of the 405 nm excitation source may allow for band-to-band transitions greater than 3.06 eV. We therefore attribute the dominant mechanism for the initial strong and rapid response of the photocurrent for the 405 nm excitation source to band-to-band excitations of electron–hole pairs, which is consistent with a reduction of the bandgap from the confirmed Wurtzite structure and presence of defects in the material, and the non-negligible spectral bandwidth of the 405 nm excitation source. During the fast photocurrent response, the initial band bending present before illumination quickly separates photogenerated electrons and holes with electrons confined to the conduction region and holes swept to the grain boundary, increasing the electron lifetime and resulting in the observed quick increase in the photocurrent. The PAMD mechanism also removes adsorbed oxygen from the surface and lowers the potential barrier. The slow rise in photocurrent can be understood in terms of the surface-related oxygen adsorption and desorption mechanisms. Oxygen desorption occurs due to the PAMD mechanism and the hole-assisted recombination mechanism with adsorbed oxygen. The large accumulation of holes on the grain boundary and the oxygen desorption mechanisms lower the potential barrier and increase the probability for electrons in the conduction region

to overcome the barrier and re-adsorb oxygen on the surface. The competition between the surface-related oxygen desorption mechanisms and the oxygen adsorption mechanism results in a slow increase in the current that saturates when the rates of these two processes reach a steady state.

The photocurrent for the 532 nm (2.33 eV) excitation source initially increases from I_d by ~20% in 10 s, then slowly increases by an additional ~45% after 15 min. In this case, the fast response can be attributed to the generation of electron–hole pairs due to optical transitions between the VB and intermediate defect levels, and between intermediate defect levels and the CB. Possible transitions from the VB to intermediate defect levels include VB $\rightarrow V_o^+$ [33] and VB $\rightarrow V_{Zn}^{-1}$ [24], and possible transitions from intermediate defect levels to the CB include $V_{Zn}^{-1} \rightarrow$ CB [24, 65] and $V_o^0 \rightarrow$ CB [74]. A second transition from an excited state in the intermediate defect level to the CB is possible if the energy level of the excited state lies less than 2.33 eV below the CB edge [24]. Significant hole trapping occurs due to transitions from intermediate defect levels to the CB, and fewer holes are swept to the grain boundary as compared to the 405 nm excitation source. The holes that form a bound exciton with an electron excited from an intermediate defect level into the CB are likely to be deeply trapped and unable to thermally relax back to the VB, while holes trapped closer to the VB thermalize back to the VB to then be re-trapped, recombine with a trapped electron on the surface to desorb oxygen, or recombine with an electron at a recombination center. Additionally, holes created due to excitation from intermediate defect states to the CB may become deeply trapped as a result of the subsequent distortion of the surrounding lattice [84]. For example, Penfold et al. have shown using simulations and x-ray absorption spectroscopy combined with a dispersive x-ray emission spectrometer, that photoexcited holes in ZnO nanoparticles become trapped at V_o^+ sites where, after the outward displacement of the surrounding zinc atoms, becomes a V_o^{++} site [84]. Significant hole trapping results in a reduced oxygen desorption rate relative to that with the 405 nm excitation source, resulting in a slow rise of the photocurrent. Note that the initial barrier height should be the same for all three excitation sources, as the device was held in the dark for ~2 h to achieve a steady state dark current prior to illumination. We postulate that the dominant process which acts to desorb surface oxygen and reduce the barrier height for the 532 nm excitation source is due to the PAMD mechanism. The change in the height of the

barrier for the 532 nm excitation source is much less than with the 405 nm excitation source as a consequence of greater hole trapping, which results in fewer surface oxygen being desorbed. The higher barrier height with 532 nm, as compared to the 405 nm excitation source, in conjunction with significant hole trapping, increases the rate of rise for the slow portion of the 532 nm photocurrent rise response, as the two effects lower the probability for electrons to overcome the barrier and adsorb surface oxygen.

The photocurrent for the 633 nm (1.96 eV) excitation source initially increases from I_d by ~10% in 10 s and then very slowly increases by an additional ~15% after 15 min. Similar to the 532 nm excitation source, the fast rise response is attributed to the generation of electron–hole pairs due to optical transitions between the VB and intermediate defect levels, and between intermediate defect levels and the CB. A possible transition from the VB to an intermediate defect level is VB $\rightarrow$ V_o^+ [33] for V_o^+ lying less than 1.96 eV above the VB edge, and possible transitions from intermediate defect levels to the CB include $V_{Zn}^{-1} \rightarrow$ CB [24, 65] and $V_o^0 \rightarrow$ CB [74]. The broad range of reported energy levels as displayed in Figure 4.3(a) makes it difficult to determine if the VB $\rightarrow$ V_o^+ transition is possible for the 633 nm excitation source. If the V_o^+ level lies more than 1.96 eV above the VB edge, the VB $\rightarrow$ V_o^+ transition is not possible. A second transition from V_o^+ to the CB is possible if the energy level is less than 1.96 eV below the CB or if, after a lattice distortion, the energy level changes and allows the transition [24, 84]. Nevertheless, we postulate that the majority of the transitions occur from intermediate defect states to the CB, resulting in the vast majority of holes created during illumination being trapped in deep intermediate defect states and unable to desorb surface oxygen at a rate comparable to the 532 and 405 nm excitation sources. This results in the smallest change in the potential barrier height, as compared to the 532 and 405 nm excitation sources. The slow photocurrent rise time constant is the greatest of all three excitation sources ($\tau_2 = 2550$ s). We attribute the very slow photocurrent rise characteristics to a combination of the PAMD mechanism and the aforementioned hole trapping resulting from photoexcitation of carriers from intermediate defect states to the CB. Here, oxygen is desorbed via the PAMD mechanism; however, the high potential barrier and trapped holes means that oxygen cannot be sufficiently re-adsorbed at a rate comparable to the 405 and 532 nm excitation sources. The result is a slow rise in the photocurrent that does not saturate and an abundance of oxygen left on the surface, as compared to the 405 and

532 nm excitation sources, which is attributed to significant hole trapping. Similar very slow photocurrent rise characteristics have been observed for a single ZnO NW device under vacuum, where the re-adsorption of oxygen was inhibited, resulting in a slow photocurrent rise response due to the rate of oxygen desorption being faster than the rate of adsorption [48].

4.6.4 Photocurrent Decay Response Analysis

Displayed in Figure 4.7 are the normalized fast and slow photocurrent decay responses for each excitation source and the corresponding fits and parameters attained with a Kohlrausch stretched exponential function. The insets are expanded views of the initial fast decay behavior of the device within the first 20 s after termination of illumination. The shaded areas represent the period when the device was illuminated with the respective source. The photocurrent decay curves are best fit with a Kohlrausch stretched exponential function and a double exponential function, regardless of the excitation source. The Kohlrausch stretched exponential function is generally used to describe decay in systems that exhibit multiple energy transfer mechanisms [39, 41, 68, 70, 85] and is of the form

$$I_n(t) = Ce^{-(t/\tau)^\gamma}, \tag{4.3}$$

where I_n is the normalized photocurrent (I_{pc}/I_d), C is a positive constant, τ is the relaxation time constant, and γ is a stretching parameter in the range $0 < \gamma \leq 1$. The Kohlrausch stretched exponential function becomes a classical single exponential function in the limit $\gamma \rightarrow 1$, at which point the differences in energy transfer mechanisms are indistinguishable [41]. The fitting parameters for the Kohlrausch stretched exponential function in Figure 4.7 are $\tau = (202, 1780, 528)$ s and $\gamma = (0.34, 0.38, 0.51)$ for $\lambda = (405, 532, 633)$ nm. The Kohlrausch stretched exponential function is a convenient model to describe systems that deviate slightly from classical single exponential behavior; however, because there is such a large spread in reported values of γ and τ in the literature for ZnO photocurrent decay, it is difficult to distinguish and associate the parameters with an underlying physical process [39, 41, 68]. Therefore, we have also provided the parameters attained with a fit of a double

exponential function. The double exponential function for the photocurrent decay has the form

$$I_\text{n}(t) = D_0 + F_1 e^{-\frac{t-t_1}{\tau_3}} + F_2 e^{-\frac{t-t_1}{\tau_4}}, \tag{4.4}$$

where I_n is the normalized photocurrent (I_pc/I_d), D_0, F_1, and F_2 are constants, t_1 is the time at termination of illumination, and τ_3 and τ_4 are the fast and slow relaxation time constants, respectively. The time constants attained with the double-exponential fits are $\tau_3 = (107, 711, 425)$ s and $\tau_4 = (1676, 4655, 5571)$ s for $\lambda = (405, 532, 633)$ nm.
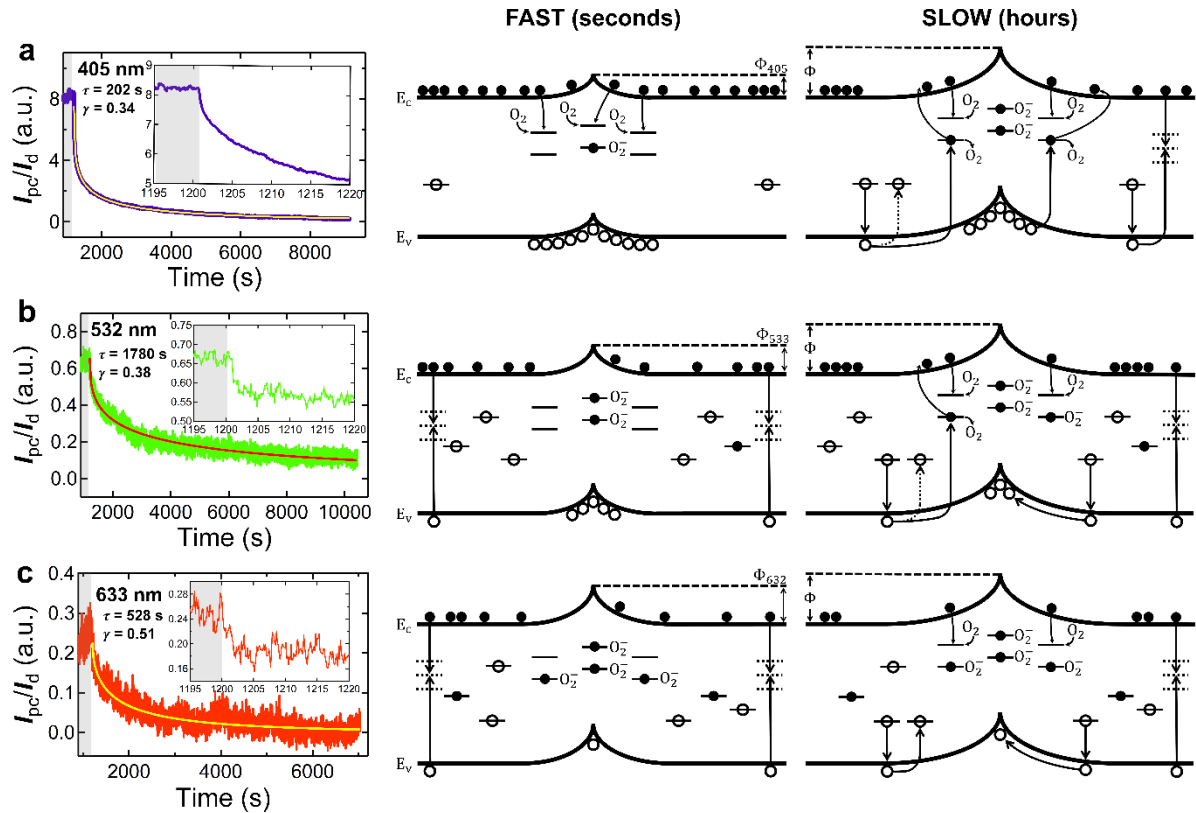
Figure 4.7 The normalized photocurrent decay characteristics of the (**a**) 405 nm, (**b**) 532 nm, and (**c**) 633 nm excitation sources, where the solid lines are fits obtained using the Kohlrausch stretched exponential function. The insets in each photocurrent decay plot show the initial fast decay behavior within the first 20 s after termination of illumination. The shaded areas represent the periods when the device was under illumination with the respective excitation source. Displayed to the right of each decay curve are the corresponding band diagrams showing the dominant photocurrent relaxation mechanisms for the fast and slow decay responses.

When the 405 nm excitation source is turned off, there is an initial sharp decay of the photocurrent that decreases by ~19% of its value at termination of illumination ($I_{t_{off}}$) within 2 s, followed by a slow decay that decreases by ~97% of $I_{t_{off}}$ after 2 h. As discussed earlier, the radiative portion of the recombination processes occurs on the order of ~ns upon termination of illumination [22]. Therefore, the observed photocurrent decay and the corresponding recombination mechanisms on the order of seconds–hours are non-radiative recombination processes. The initial rapid decay of the photocurrent is likely due to the quick re-adsorption of oxygen at grain boundaries or near the surface. The low potential barrier immediately following termination of illumination facilitates the re-adsorption of oxygen on the surface due to the high probability of an electron in the CB overcoming the low barrier to re-adsorb oxygen at grain boundaries or near the surface. Also, with 405 nm excitation there is much less hole trapping and more holes are accumulated on the grain boundary, as compared to the 532 and 633 nm excitation sources. This allows for a faster rate of the desorption of oxygen from the surface, keeping the potential barrier lower and allowing for a quicker recovery of the current during the fast decay process compared to the 532 and 633 nm excitation sources. As the oxygen adsorption and desorption processes continue, there is a gradual accumulation of negative charge at the surface that increases the band bending, and in turn slows the rate of photocurrent decay as the probability for an electron to overcome the potential barrier and re-adsorb oxygen decreases. Ultimately, it is then the competition between the surface-related oxygen desorption mechanism, recombination, and oxygen re-adsorption mechanism that are responsible for the slow decay of the current, which eventually saturates when the oxygen desorption and recombination rates reach a steady state.

With 532 nm illumination, there is a small, but notable, initial rapid decay of the photocurrent that decreases by ~12% of $I_{t_{off}}$ within 2 s, as shown in the inset of Figure 4.7(b). The initial rapid decay of the photocurrent can be attributed to trap-assisted recombination and/or the quick re-adsorption of oxygen at grain boundaries or near the surface. The high potential barrier immediately following the termination of illumination decreases the probability for electrons in the CB to overcome the barrier to quickly facilitate the re-adsorption of oxygen. Therefore, we attribute the initial rapid decay in the first 2 s to trap-assisted recombination of electrons and holes. The slow decay of the photocurrent with

532 nm illumination is the slowest of the illumination sources used in this study, where the photocurrent only decreases by ~80% of $I_{t_{off}}$ after 2 h. We attribute this very slow decay of the photocurrent to the oxygen adsorption and desorption mechanisms, where the oxygen desorption mechanism is considerably hindered as a result of the significant hole trapping. Here, very few holes are swept to the grain boundaries because they are in deep traps. Alternatively, holes are thermally emitted back to the VB where they can desorb surface oxygen to free electrons, be re-trapped, or combine with an electron at a recombination center. The combination of deep hole trapping associated with sub-bandgap excitation and the corresponding high potential barrier leads to increased carrier lifetimes and an extreme persistence in the photocurrent.

Like the 532 nm decay response, the 633 nm decay response exhibits an initial rapid decay of the photocurrent that decreases by ~25% of $I_{t_{off}}$ within 2 s and is attributed to trap-assisted recombination of electrons and holes. Unlike 405 and 532 nm illumination, the 633 nm photocurrent decays back to the dark current value and does so in only 1.5 h following termination of illumination, which is the quickest recovery of all the illumination sources. We postulate that immediately following termination of illumination, a very small number of holes diffuse to the grain boundary, as compared to the 405 and 532 nm excitation sources. This is attributed to holes trapped in deep defect levels associated with 633 nm illumination, which primarily excited electron–hole pairs from mid-gap defect levels to the CB. Significant hole trapping in deep defect levels results in the lowest rate of the desorption of surface oxygen following termination of illumination, as compared to 405 and 532 nm excitation. Finally, based on the low photocurrent with 633 nm excitation relative to 405 and 532 nm excitation, the density of carriers in the CB is accordingly less. The low density of carriers combined with fewer surface oxygen sites available to re-adsorb oxygen results in a quicker recovery of the photocurrent, as compared to 405 and 532 nm excitation, because there are only a small number of carriers that recombine at recombination centers or assist with the re-adsorption of oxygen at the very few surface oxygen sites available. Hence, the recovery of the dark current for the 633 nm excitation source is the fastest of all three illumination sources.

4.6.5   Trap Depth

The depths of the traps can be estimated from the photocurrent decay curves. The Bube model for photocurrent decay is given by the relationship, $I = I_0 \exp(-Pt)$, where I is the current at any time t, I_0 is the current at the moment of termination of illumination, and P is the probability rate of an electron (hole) escaping from a trap [86]. Since the electrons (holes) have a Maxwellian distribution of thermal energies, the probability rate that an electron (hole) will escape from a trap with a depth of energy E at a temperature T is $P = s \exp(-E/kT)$, where k is the Boltzmann constant (1.381×10^{-23} J K^{-1}), T is the absolute temperature, and s is the attempt to escape frequency [87]. The attempt to escape frequency is the product of the frequency at which phonons attempt to remove electrons (holes) from traps and the probability of transition from the trap to the conduction (valence) band [40, 87]. The attempt to escape frequency for ZnO has been found to lie between ~10^9 and 10^{11} Hz at room temperature [22, 87]. Combining the two relations, the energy of the trap depth at any time t along the photocurrent decay curve can be expressed as

$$E = kT \left[\ln(s) - \ln \left(\frac{\ln(I_0/I)}{t} \right) \right]. \tag{4.5}$$

The trap depths calculated from the photocurrent decay curves for each respective excitation source at 1, 10, and 100 min after termination of illumination (t_{off}) are given in Table 4.1. The trap depths are given as a range using the low and high values of the attempt to escape frequency and vary from ~0.65 to 0.82 eV 1 min after t_{off} to ~0.74–0.91 eV 100 min after t_{off}. The trap depths in the slow portion of the photocurrent decay curves closely match the peak of the calculated hole trap density spectrum of ZnO epilayers of ~0.9 eV [22] and estimations of the depths of traps in the sub-bandgap photoconductive decay in polycrystalline ZnO [23]. Penfold et al. have shown using simulations and x-ray absorption spectroscopy combined with a dispersive x-ray emission spectrometer that photoexcited holes in ZnO nanoparticles are trapped at V_0^+ defect sites that subsequently become V_0^{++} defect sites following an outward displacement of the surrounding zinc atoms [84]. The V_0^+ defect site has also been proposed as a source of hole trapping based on

photoluminescence spectra and illumination of ZnO nanorods with a variety of sub-bandgap excitation sources [28]. The calculated trap depths for the slow portion of the photocurrent decay curves match the depth of the V_o^+ defect site lying ~0.93 eV above the VB edge [5] and are close to the estimated energy level of the V_o^{++} defect site lying ~1.18 eV above the VB edge [5].

Table 4.1 Calculated trap depths at 1, 10, and 100 min after t_{off} using Equation 4.5 and data from the photocurrent decay curves for each excitation source.

Wavelength (nm)	Trap Depth (eV) 1 min	Trap Depth (eV) 10 min	Trap Depth (eV) 100 min
405	0.65–0.77	0.70–0.82	0.74–0.86
532	0.70–0.82	0.74–0.86	0.78–0.90
633	0.70–0.82	0.75–0.87	0.79–0.91

4.6.6 Saturation Photocurrent Dependence on Excitation Intensity

The excitation intensity dependence of the saturation photocurrent (I_{sat}) on a ln–ln scale for the 405, 532, and 633 nm excitation sources is displayed in Figure 4.8. The data was acquired in the range of ~0.1–2.0 mW cm^{-2} for all three excitation sources, where the applied bias was held at a constant +0.5 V. The ln–ln plots of the saturation photocurrent versus excitation intensity for all three wavelengths consist of distinct linear regions that follow a power law of the form, $I_{sat} = CI^\alpha$, where C is a constant, I is the intensity of illumination, and α is an exponent that defines the photocurrent response to excitation intensity. For 405 nm, three linear regions are observed with corresponding exponents of 0.56, 0.38, and 0.15. Only two linear regions are observed with the 532 and 633 nm excitation sources. With all illumination sources, the value of α decreases for successive linear regions and with increasing excitation intensity. The values of the exponents for the 532 and 633 nm excitation sources are $\alpha = (0.80, 0.22)$ and $\alpha = (1.1, 0.49)$, respectively. Values of $\alpha < 1$, i.e., sublinear dependence of the photocurrent on excitation intensity, correspond to trapping, recombination, and electron–hole pair generation within ZnO [88]. The sublinear dependence indicates a continuous and exponential distribution of electron traps between the CB and the electron Fermi level [40, 88, 89]. According to a physical

model proposed by Rose [88] to describe the sublinear dependence of the photocurrent on excitation intensity, increasing the excitation intensity converts increasingly more of the electron trapping states to recombination states. The slow increase of the density of recombination states decreases the electron lifetime, resulting in the slow increase in the rise of the saturation photocurrent and observed sub-linearity [88]. Our results are in agreement with similar studies of ZnO NWs which also exhibit a sublinear dependence of the photocurrent on excitation intensity [2, 20, 34].
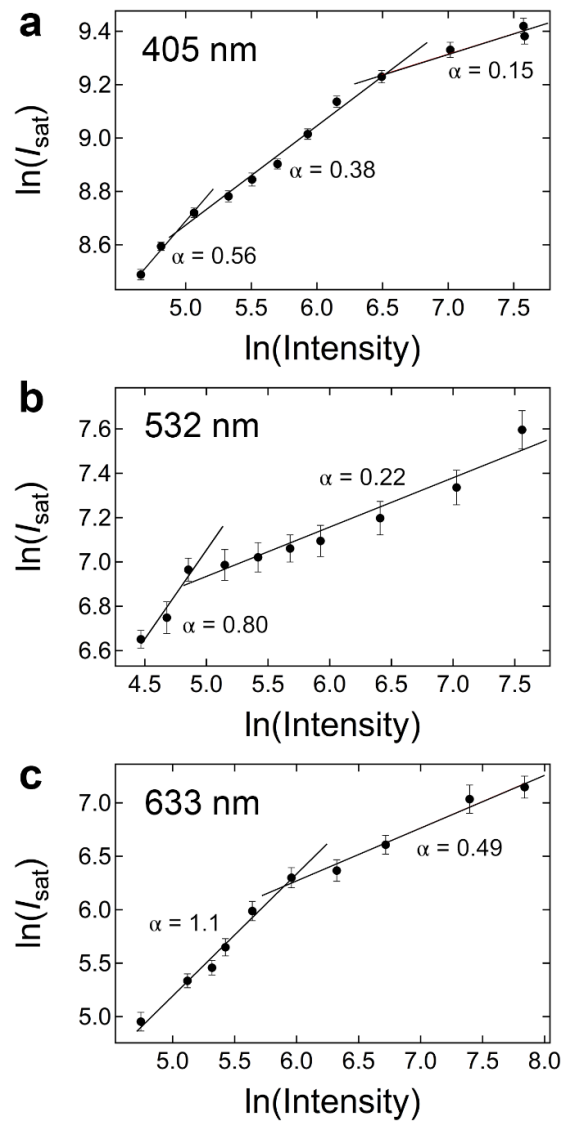

Figure 4.8 Saturation photocurrent as a function of excitation intensity on a ln–ln scale for (**a**) 405 nm (**b**) 532 nm and (**c**) 633 nm excitation sources. The applied bias was held constant at +0.5 V for each set of measurements.

The responsivity of the single ZnO–SNS device was calculated for each wavelength and at an excitation intensity of 0.1 mW cm^{-2}. The responsivity, R, is defined as the saturation photocurrent per unit of incident optical power and can be expressed as $R = I_{sat}/(IA)$, where I is the intensity of illumination and A is the irradiated area of the device. The responsivity was $R = (1740, 300, 28.9)$ A W^{-1} for $\lambda = (405, 532, 633)$ nm, and is on the order of the measured responsivity of ZnO-based photodetectors comprised of surface functionalized ZnO NWs [18] and ZnO nanoparticles [42].

We propose a simple model to explain the break in the slope of the saturation photocurrent versus excitation intensity profile observed in Figure 4.8 and Figure 4.9. Figure 4.9 shows the normalized saturation photocurrent density versus excitation intensity profile for the 405 nm excitation source. The photocurrent density (J_{pc}) was determined by subtracting the dark current density (J_d) from the total illuminated current density, and we define the normalized saturation photocurrent density (J_{sat}) as the ratio of the photocurrent density to the dark current density (J_{pc}/J_d). We noted earlier that in the case of illumination with the 405 nm excitation source, the dominant photoconductive mechanism is the generation of band-to-band electron–hole pairs; however, photocurrent can be generated via multiple photoconductive mechanisms, including band-to-band electron–hole pair generation, a PAMD mechanism, and excitation of electron–hole pairs from the VB to intermediate defect states and from intermediate defect states to the CB. Recalling that the saturation photocurrent is taken as the photocurrent when the generation and recombination processes reach a steady state, as the intensity of the excitation source is increased the number of photons exciting electrons in the bandgap also increases, resulting in a higher saturation photocurrent. However, the rate of increase of the saturation photocurrent changes and tends to decrease, as shown in Figure 4.9. Competing against the photogeneration of electron–hole pairs are processes that limit the total density of excited states and subsequently impede conduction, including the recombination of electron–hole pairs via direct recombination or at recombination centers, which becomes more significant as the intensity increases. As noted earlier, the rate of change of the saturation photocurrent with excitation intensity is due to the recombination rate arising from the increase in electron trapping states becoming recombination states as the excitation intensity is increased [40, 88]. In line with this, it is understood that the rate of recombination increases as more

electrons and holes are generated. Furthermore, we propose that the rate of increase in saturation photocurrent depends on the number of energy states that the electrons (holes) can access in the conduction (valence) band which depend on the photon energy that they absorbed and the energy level of the defect states in the bandgap where the electrons (holes) are initially trapped.
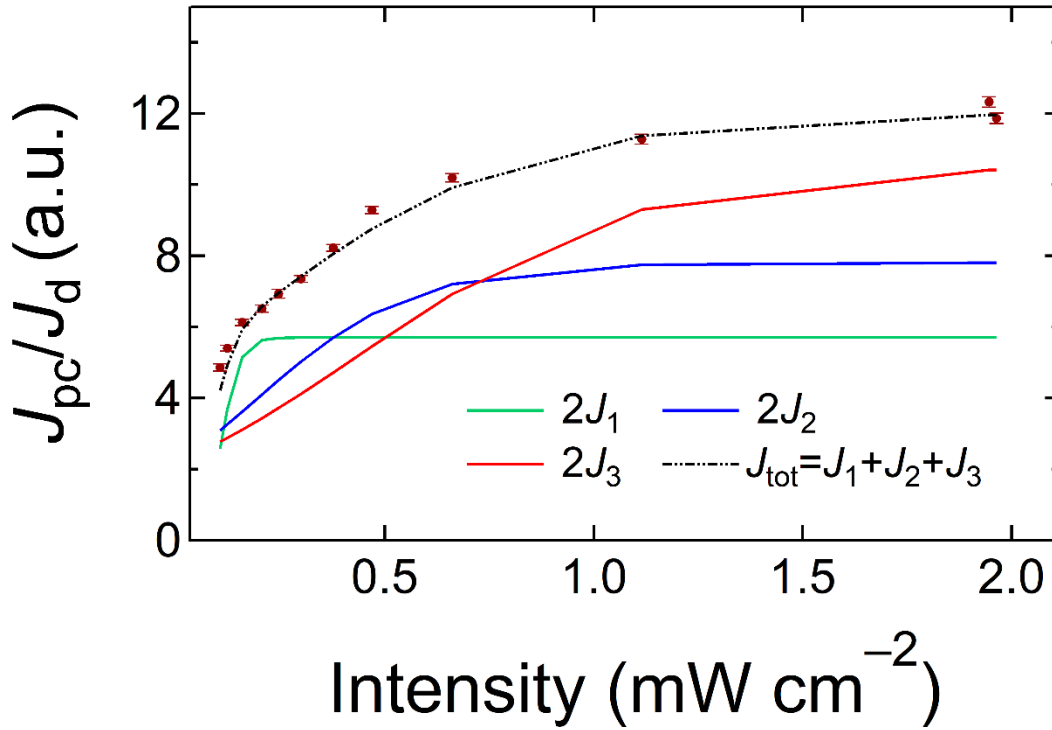

Figure 4.9 The normalized saturation photocurrent density versus excitation intensity profile of the single ZnO–SNS device when illuminated with the 405 nm excitation source and fitted with a function given by Equation 4.8. In the figure, the values of J_1, J_2, and J_3 are doubled to magnify the profile of each curve. Each curve shows a distinct rise and plateau that we attribute to different transition levels and rate of recombination processes.

To capture the net effect of these competing mechanisms, a logistic equation was used to model the impact of excitation intensity on the saturation photocurrent in a single ZnO–SNS at steady state, i.e.,

$$\frac{dJ_{sat}}{dI} = aJ_{sat} - bJ_{sat}^{2}. \tag{4.6}$$

The first term in the right-hand side of Equation 4.6 accounts for the generation of electron–hole pairs, while the second term limits the concentration of electrons (holes) in populating the conduction (valence) band. The ratio of a and b is the steady state value of the saturated photocurrent with respect to the excitation intensity. The general solution of Equation 4.6 is

$$J_{sat}(I) = \frac{a}{b + J_o e^{-r(I-I_o)}},$$ (4.7)

where I_o is the initial intensity of the light source, $J_o=J(I_o)$ is the initial photocurrent density, and r is the rate of rise of the saturation photocurrent with intensity, I. Note that Equation 4.7 will plateau at a specific illumination intensity. One can understand the saturation in terms of the density of initial states that the energy of the illumination source can access and excite into the CB, and because the number density of electrons in a given state is finite, the contribution to the current density from any given initial state will saturate. Note that the density of electrons in different initial states varies from state to state. While recombination, traps, etc. affect the saturation current, we can safely assume that the density of initial states accessible with a given illumination source sets the upper limit on the saturation current density, J_{sat}. Consequently, the contribution of individual initial states or bands of states to the current density will saturate at different intensities of the illumination source. When this happens, a break in the photocurrent density is observed. In the case of 532 and 633 nm excitation, a single break is observed within the range of the excitation intensity used in this study. This suggests that at a minimum, there are two bands of states that these sources access and excite to the CB. Because the probability of a transition is a function of the scattering cross section, which depends on the wavelength of light, and the initial and final state bands of the transition, we must assume that two bands of initial states accessed with 532 and 633 nm excitation are not necessarily the same. In fact, it is to be expected given that the 532 nm excitation source can access a larger energy range of initial states compared to 633 nm excitation, which is evident from the larger photocurrent with 532 nm excitation in Figure 4.5.

In contrast to 532 and 633 nm excitation, two breaks are observed in the normalized saturation photocurrent density versus intensity profile with 405 nm excitation, as shown in

Figure 4.8(a). This is to be expected given that the energy of the photons is 3.06 eV and nearly spans the ZnO bandgap of 3.37 eV. Clearly, a large range of initial states are accessed using the 405 nm excitation source, which is supported by the largest photocurrent (Figure 4.5) of the three excitation sources used in this study. Consequently, the saturation photocurrent versus excitation intensity curve for 405 nm of the single ZnO–SNS can be fitted with the sum of three different logistic functions of the form of Equation 4.7:

$$J_{tot} = J_1 + J_2 + J_3 = \sum_i \frac{a_i}{b_i + J_{o,i}e^{-r_i(I-I_o)}}. \tag{4.8}$$

The results of the fit with Equation 4.8 is displayed in Figure 4.9. The extracted parameters for the 405 nm excitation source are a_i = (3.5, 5.1, 7.1), b_i = (1.2, 1.3, 1.4), $J_{o,i}$ = (1.9, 2.0, 3.9), and r_i = (46, 5.2, 3.0) for J_1, J_2, and J_3, respectively. The fit indicates that each ratio of a_i and b_i pertains to the different transition levels of electrons (holes) from a given defect state in the bandgap to the conduction (valence) band. Here, $J_{o,i}$ is a function of the number of electrons (holes) that are involved in the transition to populate the conduction (valence) band, and r_i relates to the recombination rate of electrons and holes, where higher r may be an indication of slower recombination rates.

4.7   Conclusion

The electrical and photoconductive properties of a single ZnO–SNS were analyzed with near-UV and sub-bandgap excitation sources and display a typical two-step fast and slow rise and decay photocurrent behavior, similarly observed in other ZnO materials. The physical models used to describe the two-step rise and decay photocurrent characteristics show that these behaviors are highly dependent upon the excitation energy, the depths of the NPDs, and the subsequent trapping of electrons and holes during and after excitation. Significant hole trapping with the 532 nm excitation source is attributed as the source of the observed long photocurrent rise time during illumination and the strong persistence in the photocurrent following termination of illumination, where trapped holes are unable to facilitate desorption of surface oxygen and the corresponding high potential barrier increases the electron lifetime in the CB. The energy levels of the trap depths for each excitation

source were estimated from the photoconductive decay data and show that shallow level traps are vacated before deep level traps, and that the depth of the deep level traps during the slow portion of photoconductive decay at ~0.9 eV closely matches the reported energy levels of singly and doubly ionized oxygen vacancies, which have previously been shown to be responsible for hole trapping in ZnO. Use of a phenomenological model shows that the saturation photocurrent versus excitation intensity profile can be fit with a sum of logistic functions with each curve representing different recombination rates and transitions from different defect states in the bandgap. We find that the slopes of the saturation photocurrent versus excitation intensity dependence profile are a function of the transition probabilities of defect states, the number of carriers available to populate the conduction (valence) band, and the rate at which electrons and holes recombine. This work demonstrates the utility of a ZnO–SNS for obtaining detailed information about defect states in ZnO. Finally, this study demonstrates the value of constructing similar core–shell nanostructured devices with other materials to uncover detailed electronic properties of materials.

4.8   Acknowledgements

References

1.   Wojcik, P.M.; Bastatas, L.D.; Rajabi, N.; Bakharev, P.V.; McIlroy, D.N. The effects of sub-bandgap transitions and the defect density of states on the photocurrent response of a single ZnO-coated silica nanospring. *Nanotechnology* **2021**, *32*, 035202.

2.   Soci, C.; Zhang, A.; Xiang, B.; Dayeh, S.A.; Aplin, D.P.R.; Park, J.; Bao, X.Y.; Lo, Y.H.; Wang, D. ZnO Nanowire UV Photodetectors with High Internal Gain. *Nano Letters* **2007**, *7*, 1003–1009.

3.   Kind, H.; Yan, H.; Messer, B.; Law, M.; Yang, P. Nanowire Ultraviolet Photodetectors and Optical Switches. *Advanced Materials* **2002**, *14*, 158–160.

4.   Yuan, J.; Hu, L.; Xu, Z.; Zhang, Y.; Li, H.; Cao, X.; Liang, H.; Ruan, S.; Zeng, Y.-J. Concurrent Improvement of Photocarrier Separation and Extraction in ZnO Nanocrystal Ultraviolet Photodetectors. *The Journal of Physical Chemistry C* **2019**, *123*, 14766–14773.

5. Khokhra, R.; Bharti, B.; Lee, H.-N.; Kumar, R. Visible and UV photo-detection in ZnO nanostructured thin films via simple tuning of solution method. *Scientific Reports* **2017**, *7*, 15032.

6. Deka Boruah, B. Zinc oxide ultraviolet photodetectors: rapid progress from conventional to self-powered photodetectors. *Nanoscale Advances* **2019**, *1*, 2059–2085.

7. Chou, J.-C.; Ko, C.-C.; Kuo, P.-Y.; Lai, C.-H.; Nien, Y.-H.; Chang, J.-X. Fabrication of Dye-Sensitized Solar Cells Using Zinc Oxide Nanorod-Modified Titanium Dioxide Photoanode. *IEEE Transactions on Nanotechnology* **2019**, *18*, 553–561.

8. Tiwana, P.; Docampo, P.; Johnston, M.B.; Snaith, H.J.; Herz, L.M. Electron Mobility and Injection Dynamics in Mesoporous ZnO, SnO $_2$, and TiO $_2$ Films Used in Dye-Sensitized Solar Cells. *ACS Nano* **2011**, *5*, 5158–5166.

9. Bastatas, L.; Wagle, P.; Echeverria, E.; Austin, A.; McIlroy, D. The Effect of UV Illumination on the Room Temperature Detection of Vaporized Ammonium Nitrate by a ZnO Coated Nanospring-Based Sensor. *Materials* **2019**, *12*, 302.

10. Bakharev, P.; McIlroy, D. Signal-to-Noise Enhancement of a Nanospring Redox-Based Sensor by Lock-in Amplification. *Sensors* **2015**, *15*, 13110–13120.

11. Bakharev, P.V.; McIlroy, D.N. The effect of the periodic boundary conditions of a ZnO-coated nanospring on its surface redox-induced electrical response. *Nanotechnology* **2014**, *25*, 475501.

12. Dobrokhotov, V.; Oakes, L.; Sowell, D.; Larin, A.; Hall, J.; Kengne, A.; Bakharev, P.; Corti, G.; Cantrell, T.; Prakash, T.; et al. ZnO coated nanospring-based chemiresistors. *Journal of Applied Physics* **2012**, *111*, 044311.

13. Liang, H.; Feng, Q.; Xia, X.; Li, R.; Guo, H.; Xu, K.; Tao, P.; Chen, Y.; Du, G. Room temperature electroluminescence from arsenic doped p-type ZnO nanowires/n-ZnO thin film homojunction light-emitting diode. *Journal of Materials Science: Materials in Electronics* **2014**, *25*, 1955–1958.

14. Son, D.I.; Kwon, B.W.; Park, D.H.; Seo, W.-S.; Yi, Y.; Angadi, B.; Lee, C.-L.; Choi, W.K. Emissive ZnO–graphene quantum dots for white-light-emitting diodes. *Nature Nanotechnology* **2012**, *7*, 465–471.

15. Zhang, L.; Bai, S.; Su, C.; Zheng, Y.; Qin, Y.; Xu, C.; Wang, Z.L. A High-Reliability Kevlar Fiber-ZnO Nanowires Hybrid Nanogenerator and its Application on Self-Powered UV Detection. *Advanced Functional Materials* **2015**, *25*, 5794–5798.

16. Wang, J.; Chen, R.; Xiang, L.; Komarneni, S. Synthesis, properties and applications of ZnO nanomaterials with oxygen vacancies: A review. *Ceramics International* **2018**, *44*, 7357–7377.

17. Bora, T.; Zoepfl, D.; Dutta, J. Importance of Plasmonic Heating on Visible Light Driven Photocatalysis of Gold Nanoparticle Decorated Zinc Oxide Nanorods. *Scientific Reports* **2016**, *6*, 26913.

18. Cammi, D.; Zimmermann, K.; Gorny, R.; Vogt, A.; Dissinger, F.; Gad, A.; Markiewcz, N.; Waag, A.; Prades, J.D.; Ronning, C.; et al. Enhancement of the Sub-Band-Gap

Photoconductivity in ZnO Nanowires through Surface Functionalization with Carbon Nanodots. *The Journal of Physical Chemistry C* **2018**, *122*, 1852–1859.

19. Kouklin, N. Cu-Doped ZnO Nanowires for Efficient and Multispectral Photodetection Applications. *Advanced Materials* **2008**, *20*, 2190–2194.

20. Prabhakar, R.R.; Mathews, N.; Jinesh, K.B.; Karthik, K.R.G.; Pramana, S.S.; Varghese, B.; Sow, C.H.; Mhaisalkar, S. Efficient multispectral photodetection using Mn doped ZnO nanowires. *Journal of Materials Chemistry* **2012**, *22*, 9678.

21. Hu, L.; Liao, Q.; Xu, Z.; Yuan, J.; Ke, Y.; Zhang, Y.; Zhang, W.; Wang, G.P.; Ruan, S.; Zeng, Y.-J.; et al. Defect Reconstruction Triggered Full-Color Photodetection in Single Nanowire Phototransistor. *ACS Photonics* **2019**, *6*, 886–894.

22. Moazzami, K.; Murphy, T.E.; Phillips, J.D.; Cheung, M.C.-K.; Cartwright, A.N. Sub-bandgap photoconductivity in ZnO epilayers and extraction of trap density spectra. *Semiconductor Science and Technology* **2006**, *21*, 717–723.

23. Bastatas, L.D.; Wagle, P.; Echeverria, E.; Slinker, J.D.; McIlroy, D.N. Electrical characterization of ZnO-coated nanospring ensemble by impedance spectroscopy: probing the effect of thermal annealing. *Nanotechnology* **2019**, *30*, 234006.

24. Kavitha, M.K.; Jinesh, K.B.; Philip, R.; Gopinath, P.; John, H. Defect engineering in ZnO nanocones for visible photoconductivity and nonlinear absorption. *Physical Chemistry Chemical Physics* **2014**, *16*, 25093–25100.

25. Alenezi, M.R.; Henley, S.J.; Silva, S.R.P. On-chip Fabrication of High Performance Nanostructured ZnO UV Detectors. *Scientific Reports* **2015**, *5*, 8516.

26. Ye, J.D.; Gu, S.L.; Qin, F.; Zhu, S.M.; Liu, S.M.; Zhou, X.; Liu, W.; Hu, L.Q.; Zhang, R.; Shi, Y.; et al. Correlation between green luminescence and morphology evolution of ZnO films. *Applied Physics A* **2005**, *81*, 759–762.

27. Bandopadhyay, K.; Mitra, J. Zn interstitials and O vacancies responsible for n-type ZnO: what do the emission spectra reveal? *RSC Advances* **2015**, *5*, 23540–23547.

28. Sett, D.; Sarkar, S.; Basak, D. A successive photocurrent transient study to probe the sub-band gap electron and hole traps in ZnO nanorods. *RSC Advances* **2014**, *4*, 58553–58558.

29. Ahn, C.H.; Kim, Y.Y.; Kim, D.C.; Mohanta, S.K.; Cho, H.K. A comparative analysis of deep level emission in ZnO layers deposited by various methods. *Journal of Applied Physics* **2009**, *105*, 013502.

30. Lima, S.A.M.; Sigoli, F.A.; Jafelicci Jr, M.; Davolos, M.R. Luminescent properties and lattice defects correlation on zinc oxide. *International Journal of Inorganic Materials* **2001**, *3*, 749–754.

31. Clark, S.J.; Robertson, J.; Lany, S.; Zunger, A. Intrinsic defects in ZnO calculated by screened exchange and hybrid density functionals. *Physical Review B* **2010**, *81*, 115311.

32. Janotti, A.; Van de Walle, C.G. New insights into the role of native point defects in ZnO. *Journal of Crystal Growth* **2006**, *287*, 58–65.

33. Bandopadhyay, K.; Mitra, J. Spatially resolved photoresponse on individual ZnO nanorods: correlating morphology, defects and conductivity. *Scientific Reports* **2016**, *6*, 28468.

34. Fan, Z.; Chang, P.; Lu, J.G.; Walter, E.C.; Penner, R.M.; Lin, C.; Lee, H.P. Photoluminescence and polarized photodetection of single ZnO nanowires. *Applied Physics Letters* **2004**, *85*, 6128–6130.

35. Keem, K.; Kim, H.; Kim, G.-T.; Lee, J.S.; Min, B.; Cho, K.; Sung, M.-Y.; Kim, S. Photocurrent in ZnO nanowires grown from Au electrodes. *Applied Physics Letters* **2004**, *84*, 4376–4378.

36. Li, Q.H.; Gao, T.; Wang, Y.G.; Wang, T.H. Adsorption and desorption of oxygen probed from ZnO nanowire films by photocurrent measurements. *Applied Physics Letters* **2005**, *86*, 123117.

37. Liu, Y.; Zhang, Z.; Xu, H.; Zhang, L.; Wang, Z.; Li, W.; Ding, L.; Hu, Y.; Gao, M.; Li, Q.; et al. Visible Light Response of Unintentionally Doped ZnO Nanowire Field Effect Transistors. *The Journal of Physical Chemistry C* **2009**, *113*, 16796–16801.

38. Menzel, A.; Subannajui, K.; Güder, F.; Moser, D.; Paul, O.; Zacharias, M. Multifunctional ZnO-Nanowire-Based Sensor. *Advanced Functional Materials* **2011**, *21*, 4342–4348.

39. Reemts, J.; Kittel, A. Persistent photoconductivity in highly porous ZnO films. *Journal of Applied Physics* **2007**, *101*, 013709.

40. Mishra, S.K.; Srivastava, R.K.; Prakash, S.G.; Yadav, R.S.; Panday, A.C. Photoluminescence and photoconductive characteristics of hydrothermally synthesized ZnO nanoparticles. *Opto-Electronics Review* **2010**, *18*, 467–473.

41. Covington, L.R.; Moore, J.C. Photoconductivity and transient response of Al:ZnO:Al planar structures fabricated via a thermal oxidation process. *Thin Solid Films* **2013**, *540*, 106–111.

42. Jin, Y.; Wang, J.; Sun, B.; Blakesley, J.C.; Greenham, N.C. Solution-Processed Ultraviolet Photodetectors Based on Colloidal ZnO Nanoparticles. *Nano Letters* **2008**, *8*, 1649–1653.

43. Sharma, P.; Sreenivas, K.; Rao, K.V. Analysis of ultraviolet photoconductivity in ZnO films prepared by unbalanced magnetron sputtering. *Journal of Applied Physics* **2003**, *93*, 3963–3970.

44. Dhara, S.; Giri, P. Enhanced UV photosensitivity from rapid thermal annealed vertically aligned ZnO nanowires. *Nanoscale Research Letters* **2011**, *6*, 504.

45. Hasan Farooqi, M.M.; Srivastava, R.K. Structural, optical and photoconductivity study of ZnO nanoparticles synthesized by annealing of ZnS nanoparticles. *Journal of Alloys and Compounds* **2017**, *691*, 275–286.

46. Prades, J.D.; Hernandez-Ramirez, F.; Jimenez-Diaz, R.; Manzanares, M.; Andreu, T.; Cirera, A.; Romano-Rodriguez, A.; Morante, J.R. The effects of electron–hole separation on the photoconductivity of individual metal oxide nanowires. *Nanotechnology* **2008**, *19*, 465501.

47. Bao, J.; Shalish, I.; Su, Z.; Gurwitz, R.; Capasso, F.; Wang, X.; Ren, Z. Photoinduced oxygen release and persistent photoconductivity in ZnO nanowires. *Nanoscale Research Letters* **2011**, *6*, 404.

48. Cammi, D.; Ronning, C. Persistent Photoconductivity in ZnO Nanowires in Different Atmospheres. *Advances in Condensed Matter Physics* **2014**, *2014*, 1–5.

49. Wang, Y.; Liao, Z.; She, G.; Mu, L.; Chen, D.; Shi, W. Optical modulation of persistent photoconductivity in ZnO nanowires. *Applied Physics Letters* **2011**, *98*, 203108.

50. Zong, X.-L.; Zhu, R. Effects of surface adsorbed oxygen, applied voltage, and temperature on UV photoresponse of ZnO nanorods. *Chinese Physics B* **2015**, *24*, 107703.

51. Wojcik, P.M.; Bakharev, P.V.; Corti, G.; McIlroy, D.N. Nucleation, evolution, and growth dynamics of amorphous silica nanosprings. *Materials Research Express* **2017**, *4*, 015004.

52. Wang, L.; Major, D.; Paga, P.; Zhang, D.; Norton, M.G.; McIlroy, D.N. High yield synthesis and lithography of silica-based nanospring mats. *Nanotechnology* **2006**, *17*, S298–S303.

53. Rajabi, N.; Wojcik, P.M.; Khanal, L.R.; Qiang, Y.; McIlroy, D.N. A comparison of the morphological and electrical properties of sol-gel dip coating and atomic layer deposition of ZnO on 3D nanospring mats. *Materials Research Express* **2018**, *6*, 035902.

54. Schmidt-Mende, L.; MacManus-Driscoll, J.L. ZnO – nanostructures, defects, and devices. *Materials Today* **2007**, *10*, 40–48.

55. McCluskey, M.D. Defects in ZnO. In *Defects in Advanced Electronic Materials and Novel Low Dimensional Structures*; Woodhead Publishing: Cambridge, England, 2018; pp. 1–25; ISBN 978-0-08-102053-1.

56. Özgür, Ü.; Alivov, Ya.I.; Liu, C.; Teke, A.; Reshchikov, M.A.; Doğan, S.; Avrutin, V.; Cho, S.-J.; Morkoç, H. A comprehensive review of ZnO materials and devices. *Journal of Applied Physics* **2005**, *98*, 041301.

57. McCluskey, M.D.; Jokela, S.J. Defects in ZnO. *Journal of Applied Physics* **2009**, *106*, 071101.

58. Vlasenko, L.S.; Watkins, G.D. Optical detection of electron paramagnetic resonance in room-temperature electron-irradiated ZnO. *Physical Review B* **2005**, *71*, 125210.

59. Alvi, N.H.; ul Hasan, K.; Nur, O.; Willander, M. The origin of the red emission in n-ZnO nanotubes/p-GaN white light emitting diodes. *Nanoscale Research Letters* **2011**, *6*, 130.

60. Xu, P.S.; Sun, Y.M.; Shi, C.S.; Xu, F.Q.; Pan, H.B. The electronic structure and spectral properties of ZnO and its defects. *Nuclear Instruments and Methods in Physics Research Section B: Beam Interactions with Materials and Atoms* **2003**, *199*, 286–290.

61. Lin, B.; Fu, Z.; Jia, Y. Green luminescent center in undoped zinc oxide films deposited on silicon substrates. *Applied Physics Letters* **2001**, *79*, 943–945.

62. Tam, K.H.; Cheung, C.K.; Leung, Y.H.; Djurišić, A.B.; Ling, C.C.; Beling, C.D.; Fung, S.; Kwok, W.M.; Chan, W.K.; Phillips, D.L.; et al. Defects in ZnO Nanorods Prepared by a Hydrothermal Method. *The Journal of Physical Chemistry B* **2006**, *110*, 20865–20871.

63. An, W.; Wu, X.; Zeng, X.C. Adsorption of O_2, H_2, CO, NH_3, and NO_2 on ZnO Nanotube: A Density Functional Theory Study. *The Journal of Physical Chemistry C* **2008**, *112*, 5747–5755.

64. Safa, S.; Khajeh, M.; Azimirad, R. The effects of measuring atmosphere on ultraviolet photodetection performance of ZnO nanostructures. *Journal of Alloys and Compounds* **2018**, *735*, 1406–1413.

65. Purusothaman, Y.; Alluri, N.R.; Chandrasekhar, A.; Vivekananthan, V.; Kim, S.-J. Regulation of Charge Carrier Dynamics in ZnO Microarchitecture-Based UV/Visible Photodetector via Photonic-Strain Induced Effects. *Small* **2018**, *14*, 1703044.

66. Chen, R.-S.; Wang, W.-C.; Chan, C.-H.; Hsu, H.-P.; Tien, L.-C.; Chen, Y.-J. Photoconductivities in monocrystalline layered V2O5 nanowires grown by physical vapor deposition. *Nanoscale Research Letters* **2013**, *8*, 443.

67. Watanabe, H.; Wada, M.; Takahashi, T. The Activation Energy for Oxygen Desorption from Zinc Oxide Surfaces. *Japanese Journal of Applied Physics* **1965**, *4*, 945–947.

68. Carrey, J.; Carrère, H.; Kahn, M.L.; Chaudret, B.; Marie, X.; Respaud, M. Photoconductivity of self-assembled ZnO nanoparticles synthesized by organometallic chemistry. *Semiconductor Science and Technology* **2008**, *23*, 025003.

69. Worasawat, S.; Tasaki, K.; Neo, Y.; Pecharapa, W.; Hatanaka, Y.; Mimura, H. Persistent photocurrent characteristics of ZnO polycrystalline films prepared by RF magnetron sputtering. *Japanese Journal of Applied Physics* **2019**, *58*, 055505.

70. Moore, J.; Thompson, C. A Phenomenological Model for the Photocurrent Transient Relaxation Observed in ZnO-Based Photodetector Devices. *Sensors* **2013**, *13*, 9921–9940.

71. Madel, M.; Huber, F.; Mueller, R.; Amann, B.; Dickel, M.; Xie, Y.; Thonke, K. Persistent photoconductivity in ZnO nanowires: Influence of oxygen and argon ambient. *Journal of Applied Physics* **2017**, *121*, 124301.

72. Collins, R.J.; Thomas, D.G. Photoconduction and Surface Effects with Zinc Oxide Crystals. *Physical Review* **1958**, *112*, 388–395.

73. Melnick, D.A. Zinc Oxide Photoconduction, an Oxygen Adsorption Process. *The Journal of Chemical Physics* **1957**, *26*, 1136–1146.

74. Lany, S.; Zunger, A. Anion vacancies as a source of persistent photoconductivity in II-VI and chalcopyrite semiconductors. *Physical Review B* **2005**, *72*, 035215.

75. Mallampati, B.; Nair, S.V.; Ruda, H.E.; Philipose, U. Role of surface in high photoconductive gain measured in ZnO nanowire-based photodetector. *Journal of Nanoparticle Research* **2015**, *17*, 176.

76. Lee, J.-M.; Kim, K.-K.; Park, S.-J.; Choi, W.-K. Low-resistance and nonalloyed ohmic contacts to plasma treated ZnO. *Applied Physics Letters* **2001**, *78*, 3842–3844.

77. Chen, J.-J.; Jang, S.; Anderson, T.J.; Ren, F.; Li, Y.; Kim, H.-S.; Gila, B.P.; Norton, D.P.; Pearton, S.J. Low specific contact resistance Ti/Au contacts on ZnO. *Applied Physics Letters* **2006**, *88*, 122107.

78. Kim, H.-K.; Bae, J.W.; Kim, K.-K.; Park, S.-J.; Seong, T.-Y.; Adesida, I. Inductively-coupled-plasma reactive ion etching of ZnO using BCl3-based plasmas and effect of the plasma treatment on Ti/Au ohmic contacts to ZnO. *Thin Solid Films* **2004**, *447–448*, 90–94.

79. Murphy, T.E.; Blaszczak, J.O.; Moazzami, K.; Bowen, W.E.; Phillips, J.D. Properties of electrical contacts on bulk and epitaxial n-type ZnO. *Journal of electronic materials* **2005**, *34*, 389–394.

80. Heiland, G.; Mollwo, E.; Stöckmann, F. Electronic Processes in Zinc Oxide. In *Solid State Physics*; Academic Press: Cambridge, MA, USA, 1959; Vol. 8, pp. 191–323; ISBN 978-0-12-607708-7.

81. Takahashi, Y.; Kanamori, M.; Kondoh, A.; Minoura, H.; Ohya, Y. Photoconductivity of Ultrathin Zinc Oxide Films. *Japanese Journal of Applied Physics* **1994**, *33*, 6611–6615.

82. Razavi-Khosroshahi, H.; Edalati, K.; Wu, J.; Nakashima, Y.; Arita, M.; Ikoma, Y.; Sadakiyo, M.; Inagaki, Y.; Staykov, A.; Yamauchi, M.; et al. High-pressure zinc oxide phase as visible-light-active photocatalyst with narrow band gap. *Journal of Materials Chemistry A* **2017**, *5*, 20298–20303.

83. Lee, H.; An, N.; Jeong, S.; Kang, S.; Kwon, S.; Lee, J.; Lee, Y.; Kim, D.Y.; Lee, S. Strong dependence of photocurrent on illumination-light colors for ZnO/graphene Schottky diode. *Current Applied Physics* **2017**, *17*, 552–556.

84. Penfold, T.J.; Szlachetko, J.; Santomauro, F.G.; Britz, A.; Gawelda, W.; Doumy, G.; March, A.M.; Southworth, S.H.; Rittmann, J.; Abela, R.; et al. Revealing hole trapping in zinc oxide nanoparticles by time-resolved X-ray spectroscopy. *Nature Communications* **2018**, *9*, 478.

85. Tian, Y.; Zhang, J.; Guo, C.F.; Zhang, B.; Liu, Q. Photoconductive probing of the trap distribution in switchable interfaces. *Nanoscale* **2016**, *8*, 915–920.

86. Bube, R.H. *Photoconductivity of Solids*; R.E. Krieger Pub. Co: Huntington, NY, USA, 1978; ISBN 978-0-88275-660-8.

87. Randall, J.T.; Wilkins, M.H.F. Phosphorescence and electron traps - I. The study of trap distributions. *Proceedings of the Royal Society of London. Series A. Mathematical and Physical Sciences* **1945**, *184*, 365–389.

88. Rose, A. *Concepts in Photoconductivity and Allied Problems*; Interscience Publishers: New York, NY, USA, 1963; ISBN 978-0-88275-568-7.

89. Pillai, P.K.C.; Shroff, N.; Kumar, N.N.; Tripathi, A.K. Photoconductivity and dark-conductivity studies of CdS $1 - x$ Se x (Cu) sintered layers. *Physical Review B* **1985**, *32*, 8228–8233.

CHAPTER 5

Summary and Conclusion

5.1   Summary

We have identified the initial phases of formation and growth dynamics of amorphous silica nanosprings (SNSs). The low temperature and atmospheric pressure conditions during the initial stages of catalyst formation create an asymmetrically-shaped Au–Si catalyst. Once the Au–Si catalyst reaches a point of supersaturation, Si reacts with O_2 along the liquid–solid interface to form solid silica beneath the catalyst. As silica is formed, minimization of the surface free energy results in the formation of multiple individual silica nanowires beneath the Au–Si catalyst. The formation of individual silica nanowires is concomitant with the pinching of the Au–Si catalyst, where each single silica nanowire is localized to a region of the Au–Si catalyst. Using Laplace's Law, it is shown that the pinching of the Au–Si catalyst is a result of the system minimizing its energy.

The growth rates of individual nanowires are directly related to their diameters, and since the individual silica nanowires beneath a common Au–Si catalyst have variable diameters, they have corresponding variable growth rates. When the SNS consists of a bundle of tightly-packed nanowires, as opposed to a row of nanowires, we postulate that an additional anisotropy in the growth rate is produced when diffusion of O_2 to the inner nanowires is hindered by the outer layer of nanowires. In either case, a SNS comprised of either a row or a bundle of nanowires, the varying growth rates of the individual nanowires create variations in the work of adhesion (contact angle) about the outer boundary of the catalyst–nanowires interface. Using Stokes' theorem and a previous contact angle anisotropy mechanism that describes the helical precession of single nanowires, we show that an effective contact angle anisotropy mechanism produces the asymmetry necessary for the helical precession of the catalyst and the subsequent helical morphology of the SNS.

Utilizing the SNS as an insulating support for the novel conductive carbon, graphite from the University of Idaho thermolyzed asphalt reaction (GUITAR), has fully revealed its morphology and allowed the detailed analysis of its electrical transport properties. The Raman spectrum of a GUITAR coating on a silicon substrate displays two distinct peaks located at 1347 cm^{-1} and 1589 cm^{-1}, and a broad peak centered at ~2800 cm^{-1}. The broad peak reveals that GUITAR is located in Stage (2) of Ferrari and Robertson's three stage model used to characterize the disorder of carbons, where Stage (2) corresponds to the evolution of nanocrystalline graphite to amorphous carbon. Further analysis of the excitation

dependence of GUITAR's Raman spectrum reveals that the dispersion of the D and G peaks are indicative of GUITAR being characteristic of nanocrystalline graphite with a low sp^3 content.

Images obtained via scanning electron microscopy (SEM), transmission electron microscopy (TEM), and atomic force microscopy (AFM), together show that the GUITAR coating is a ~100 nm thick layer consisting of an agglomeration of irregularly shaped carbon nanospheres ranging in diameter from ~50 to 100 nm. Detailed TEM images of a GUITAR coating on a SNS reveal that the carbon nanospheres are comprised of unclosed graphitic flakes, varying in diameter from ~1 to 5 nm, consistent with estimations of the crystalline size calculated via Raman spectroscopic analyses. The analysis of the morphology indicates that the GUITAR coating is an agglomeration of carbon nanospheres formed via the accretion of unclosed graphitic flakes.

Eleven single GUITAR-coated SNS electrical devices were fabricated and used to characterize GUITAR's electrical transport properties. Each single GUITAR-coated SNS electrical device displayed a negative temperature coefficient of resistivity. The average temperature coefficient of resistivity of all 11 single GUITAR-coated SNS electrical devices was $-0.0017 \pm 0.00044 \ °C^{-1}$. The average resistivity and average temperature coefficient of resistivity confirm GUITAR's classification as a graphitic semimetal with properties consistent with nanocrystalline graphite. Raman spectroscopy, SEM, TEM, and AFM images, the negative temperature coefficient of resistivity, and the resistivity of GUITAR confirm that it is a graphitic semimetal composed of nanocrystalline graphite with a low sp^3 content.

A single polycrystalline ZnO-coated SNS electrical device was fabricated and used to characterize the optoelectronic properties of the polycrystalline ZnO layer using three excitation sources (405, 532, and 633 nm). The single ZnO-coated SNS device exhibits a typical two-step fast and slow rise and decay photocurrent response to all three excitation sources. Physical models were developed to explain the characteristics of the fast and slow rise and decay photocurrent response of each illumination source. These physical models show that the photocurrent responses of each illumination source are highly dependent on the excitation energy, the depths of the native point defects within ZnO, and the trapping of electrons and holes during and after excitation.

The slow photocurrent rise response for both the 532 and 633 nm excitation sources is attributed to the excitation of electron–hole pairs from the valence band to mid-gap states and from mid-gap states to the conduction band. The latter transitions trap holes in deep mid-gap states, resulting in a slow rate of the desorption of oxygen from the surface, which creates a high potential barrier, lowering the probability for electrons to overcome the barrier and adsorb surface oxygen. The slow rate of rise of the photocurrent response is enhanced with the 633 nm excitation source due to the energy of the source, mostly allowing transitions from mid-gap states to the conduction band, resulting in significant hole trapping, as compared to the 532 nm source. The slow photocurrent decay response for the 532 nm excitation source is attributed to significant deep hole trapping associated with sub-bandgap excitation, which considerably hinders the oxygen desorption mechanism, resulting in a high potential barrier and increased carrier lifetimes.

The depths of the traps have been estimated from the photocurrent decay curves of all three illumination sources. The calculated trap depths at 1, 10, and 100 min intervals following termination of illumination show that shallow level traps are vacated before deep level traps and that the deep level traps located at ~0.74–0.91 eV closely match the depths of single and doubly ionized oxygen vacancies that have previously been identified to be sources for hole trapping in ZnO.

The saturation photocurrent dependence on excitation intensity has been investigated for each illumination source. The ln–ln plots of the saturation photocurrent versus excitation intensity display distinct linear regions that can be represented by a power law, where the exponent defines the photocurrent response to excitation intensity. The slow increase in the density of recombination states, attributed to the conversion of electron trapping states to recombination states, decreases the electron lifetime and results in the observed sub-linearity. A phenomenological model was developed to explain the breaks in the slope of the saturation photocurrent versus excitation intensity profile for each excitation source. A logistic equation was used to model the saturation photocurrent dependence on excitation intensity. The saturation photocurrent versus excitation intensity profile for the 405 nm excitation source can be fitted with the sum of three different logistic functions, with each curve representing transitions from different defect states in the bandgap and different recombination rates.

5.2   Conclusion

We have investigated the initial phases of formation and growth dynamics of amorphous SNSs. Bundles of silica nanowires with varying diameters connected beneath a common Au–Si catalyst have corresponding varying growth rates. This variation in the growth rates creates an asymmetry in the interfacial surface tension about the outer boundary of the catalyst–nanowires interface and produces the subsequent helical morphology of the SNS. An effective contact angle anisotropy mechanism is presented and used to explain the helical morphology of SNSs. The effective contact angle anisotropy mechanism can be applied to other types of systems consisting of bundles of amorphous nanowires or nanotubes. The characterization of the initial phases of formation and growth dynamics of SNSs will assist future researchers in the development of methods for creating nanosprings and nanowires from other materials.

The latter part of this dissertation demonstrates the utility of the SNS as a suitable insulating support for the detailed characterization of the morphology and the electronic and optoelectronic properties of two-dimensional amorphous and polycrystalline nanocoatings. Single GUITAR- and ZnO-coated SNS electrical devices were fabricated and used to characterize GUITAR's electrical transport properties and the electrical and optoelectronic properties of polycrystalline ZnO. Raman spectroscopic analyses, the characterization of the electrical transport properties of 11 single GUITAR-coated SNS electrical devices, and the use of SNSs as a support for GUITAR have fully revealed GUITAR's morphology and its nanocrystalline graphitic structure. Understanding the fundamental electronic and structural properties of GUITAR will further reveal and advance its potential for applications in energy storage and conversion and in biological sensing.

The effects of sub-bandgap transitions and the defect density of states on the photocurrent response of a single ZnO-coated SNS have been investigated. The slow rise and decay photocurrent behavior of the 532 and 633 nm excitation sources is due to the trapping of carriers in deep mid-gap states and depends on the energy of the illumination source. A phenomenological model is presented to describe the saturation photocurrent dependence on excitation intensity and shows that the slopes of the saturation photocurrent versus excitation intensity profile of each illumination source are a function of the recombination rate of electrons and holes, the number of carriers available to populate the

conduction (valence) band, and the transition probabilities of defect states. Our investigation of the sub-bandgap photocurrent response in ZnO will assist future researchers in the advancement of ZnO-based device applications that require a wide spectral response. Finally, the work presented in this dissertation demonstrates the value of constructing similar core–shell nanostructured devices with other materials to uncover detailed electronic properties of materials.

5.3   Future Directions

The following is a summary of suggestions for improvements to, and future directions for the work presented in this dissertation. The electrical devices used in chapters 3 and 4 were fabricated using the drop-casting method described in section 3.3.3 of chapter 3. We have found that the drop-casting method is the most efficient method to fabricate single GUITAR- and ZnO-coated SNS electrical devices. The efficiency of the drop-casting method is due to the SNS growth and subsequent coating procedures and the limitations of standard photolithography procedures.

Several other fabrication methods have been proposed; however, they involve extra photolithography steps and present their own set of challenges to overcome. For example, circular, round, and triangular gold catalyst shapes were created on a Si/SiO$_2$ substrate using a standard photolithography procedure described in section 2.3.2 of chapter 2. SNSs were grown from these catalyst shapes to investigate the relationship between SNS growth paths and catalyst shapes. If a SNS could grow in a predictable path from the edge of the catalyst, subsequent masks could be designed to coat the SNSs with various metals or metal-oxides and create electrical contacts. However, this method involves several additional photolithography steps compared to the drop-casting fabrication method described in chapter 3 and could potentially leave photoresist residue between the SNS and its outer-shell coating. Another possible method to fabricate single metal- and metal-oxide-coated SNS devices is to use electron-beam lithography following drop-casting on a Si/SiO$_2$ substrate. This procedure would be advantageous over the fabrication methods described in chapter 3 because it would ensure the alignment of electrical contacts on each end of the coated SNS. Electron-beam lithography would also facilitate the fabrication of multiple contacts on a

single coated SNS that could accurately measure the resistivity and specific contact resistance using the transmission line model [1] measurement technique.

The drop-casting fabrication method described in chapter 3 did not result in significant device yields, despite the efficiency of the fabrication method. As described in chapter 3, 27 electrodes, each with a ~12,000 μm long channel, were patterned on a 2.5×2.5 cm^2 Si/SiO$_2$ substrate (chip) following drop-casting. This fabrication method resulted in approximately five active devices per chip. A re-design of the electrode mask could easily incorporate ~200 12,000 μm long channel electrodes per 2.5×2.5 cm^2 chip, significantly increasing the probability of achieving properly aligned electrical contacts with a single SNS and could result in an approximately eightfold increase in the number of active devices per chip.

Utilizing the SNS as an insulating support for GUITAR and the subsequent electrical device fabrication was an efficient method for measuring the electrical transport properties of GUITAR; however, the varying diameters of the SNSs used in the electrical devices, as well as the lack of a method to measure the thickness of the GUITAR coatings on individual SNSs provided a large degree of error compared to other possible electrical device architectures. Additionally, the two-point probe method cannot measure the specific contact resistance of the GUITAR–Ti/Au electrical contacts. Significant improvements in the accuracy of measurements of GUITAR's electrical transport properties can be achieved by creating an electrical device consisting of a GUITAR coating on a flat substrate with a well-defined active area. Figure 5.1 shows the fabrication process for this GUITAR electrical device. GUITAR could be coated onto a substrate with pre-defined mask-alignment marks. Following the deposition of GUITAR on the substrate, photoresist would be spun onto the GUITAR coating, and a mask would be used to create a pattern of rectangular strips of GUITAR. Using the photoresist as a mask, the GUITAR could be etched using oxygen plasma, creating rectangular strips of GUITAR. A final photolithography step to define metal contacts, followed by metal deposition and lift-off, would produce a GUITAR electrical device with a well-defined active area and the option to include multiple electrical contacts on one strip of GUITAR. The thickness of the GUITAR coating in the active area could be measured by AFM, and the transmission line model measurement method [1] could be employed to measure the resistivity and specific contact resistance of the GUITAR–Ti/Au electrical contacts.
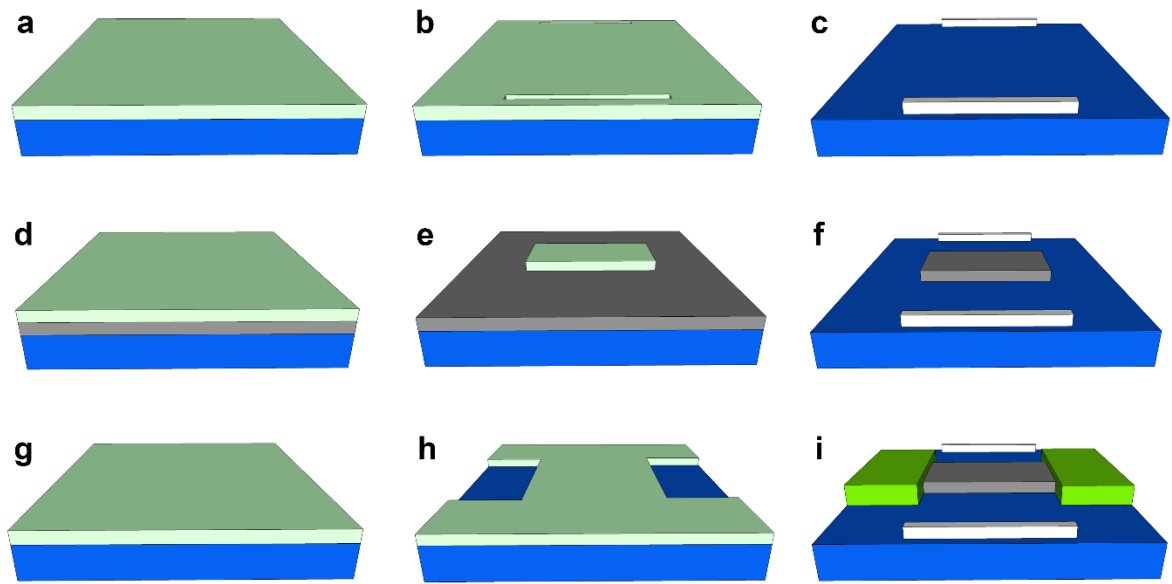
Figure 5.1 GUITAR electrical device fabrication process. (**a**) Photoresist is spun onto substrate. (**b**) Photoresist is patterned for alignment marks and developed. (**c**) Metal alignment marks are deposited via thermal evaporation and remaining metal and photoresist are removed. (**d**) GUITAR is coated onto substrate and photoresist is spun on top of GUITAR. (**e**) Photoresist is patterned and developed for GUITAR etching. (**f**) GUITAR is removed via oxygen plasma etching and remaining photoresist is removed. (**g**) Photoresist is spun onto sample. (**h**) Photoresist is patterned for electrodes and developed. (**i**) Ti/Au are deposited via thermal evaporation and remaining Ti/Au and photoresist are removed.

Further research regarding the rate of rise and decay of the photocurrent response for the single ZnO-coated SNS device can be performed by repeating the experiments after surface passivation, adjusting the oxygen concentration, or heating. Surface passivation and decreasing the oxygen concentration would inhibit the oxygen adsorption and desorption mechanisms and decrease the rate of decay of the photocurrent [2–8]. Heating will also decrease the rate of decay of the photocurrent [9]. However, these methods will not give detailed information about the identity, density, and depths of native point defects. Future experiments should focus on identifying and controlling the density of native point defects and their behavior as electron (hole) traps and studying the resulting photocurrent response characteristics. Penfold et al. have used x-ray absorption spectroscopy combined with a dispersive x-ray emission spectrometer to identify the source of the singly charged oxygen vacancy hole trap in ZnO [10], and controlling the native point defect density in ZnO can be achieved through doping, the modification of growth conditions [11], and annealing [12,

13]. Identifying and controlling native point defects in ZnO will be critical to understanding ZnO's optoelectronic properties and for developing effective ZnO-based nanoarchitectures for use in solar energy conversion applications.

References

1. Reeves, G.K.; Harrison, H.B. Obtaining the specific contact resistance from transmission line model measurements. *IEEE Electron Device Letters* **1982**, *3*, 111–113.

2. Carrey, J.; Carrère, H.; Kahn, M.L.; Chaudret, B.; Marie, X.; Respaud, M. Photoconductivity of self-assembled ZnO nanoparticles synthesized by organometallic chemistry. *Semiconductor Science and Technology* **2008**, *23*, 025003.

3. Cammi, D.; Ronning, C. Persistent Photoconductivity in ZnO Nanowires in Different Atmospheres. *Advances in Condensed Matter Physics* **2014**, *2014*, 1–5.

4. Liu, Y.; Zhang, Z.; Xu, H.; Zhang, L.; Wang, Z.; Li, W.; Ding, L.; Hu, Y.; Gao, M.; Li, Q.; et al. Visible Light Response of Unintentionally Doped ZnO Nanowire Field Effect Transistors. *The Journal of Physical Chemistry C* **2009**, *113*, 16796–16801.

5. Li, Q.H.; Gao, T.; Wang, Y.G.; Wang, T.H. Adsorption and desorption of oxygen probed from ZnO nanowire films by photocurrent measurements. *Applied Physics Letters* **2005**, *86*, 123117.

6. Moazzami, K.; Murphy, T.E.; Phillips, J.D.; Cheung, M.C.-K.; Cartwright, A.N. Sub-bandgap photoconductivity in ZnO epilayers and extraction of trap density spectra. *Semiconductor Science and Technology* **2006**, *21*, 717–723.

7. Prades, J.D.; Hernandez-Ramirez, F.; Jimenez-Diaz, R.; Manzanares, M.; Andreu, T.; Cirera, A.; Romano-Rodriguez, A.; Morante, J.R. The effects of electron–hole separation on the photoconductivity of individual metal oxide nanowires. *Nanotechnology* **2008**, *19*, 465501.

8. Mallampati, B.; Nair, S.V.; Ruda, H.E.; Philipose, U. Role of surface in high photoconductive gain measured in ZnO nanowire-based photodetector. *Journal of Nanoparticle Research* **2015**, *17*, 176.

9. Moore, J.; Thompson, C. A Phenomenological Model for the Photocurrent Transient Relaxation Observed in ZnO-Based Photodetector Devices. *Sensors* **2013**, *13*, 9921–9940.

10. Penfold, T.J.; Szlachetko, J.; Santomauro, F.G.; Britz, A.; Gawelda, W.; Doumy, G.; March, A.M.; Southworth, S.H.; Rittmann, J.; Abela, R.; et al. Revealing hole trapping in zinc oxide nanoparticles by time-resolved X-ray spectroscopy. *Nature Communications* **2018**, *9*, 478.

11. Alenezi, M.R.; Henley, S.J.; Silva, S.R.P. On-chip Fabrication of High Performance Nanostructured ZnO UV Detectors. *Scientific Reports* **2015**, *5*, 8516.

12. Kavitha, M.K.; Jinesh, K.B.; Philip, R.; Gopinath, P.; John, H. Defect engineering in ZnO nanocones for visible photoconductivity and nonlinear absorption. *Physical Chemistry Chemical Physics* **2014**, *16*, 25093–25100.

13. Bastatas, L.D.; Wagle, P.; Echeverria, E.; Slinker, J.D.; McIlroy, D.N. Electrical characterization of ZnO-coated nanospring ensemble by impedance spectroscopy: probing the effect of thermal annealing. *Nanotechnology* **2019**, *30*, 234006.
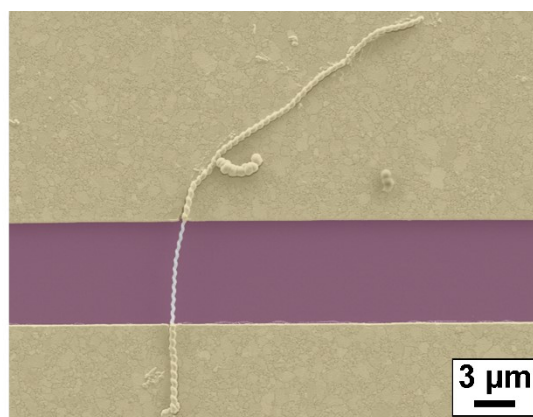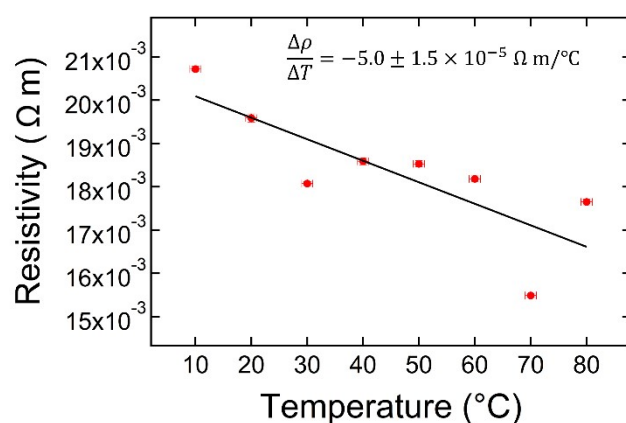
APPENDIX A

Single GUITAR-Coated Silica Nanospring Devices Overview

This appendix presents the resistivity vs. temperature profiles and false-color scanning electron microscopy images of the 11 single GUITAR-coated silica nanospring electrical devices used in the experiments described in chapter 3. The scanning electron microscopy images were acquired following electrical characterization and may not be representative of the device's condition during experimentation.

Device 1

$$\frac{\Delta\rho}{\Delta T} = -8.9 \pm 1.2 \times 10^{-6}\ \Omega\,\text{m/°C}$$

Device 2

$$\frac{\Delta\rho}{\Delta T} = -5.0 \pm 1.5 \times 10^{-5}\ \Omega\,\text{m/°C}$$
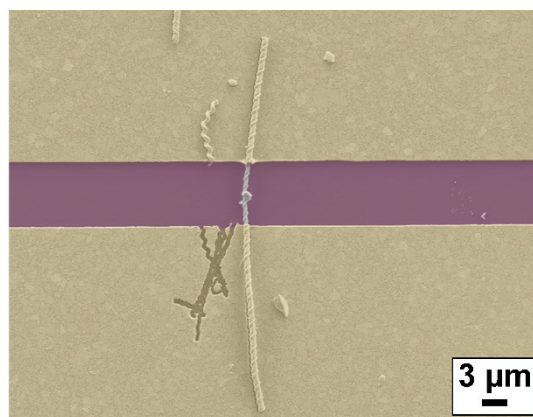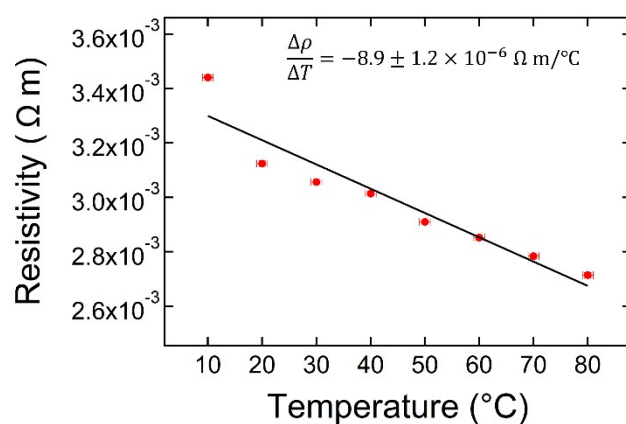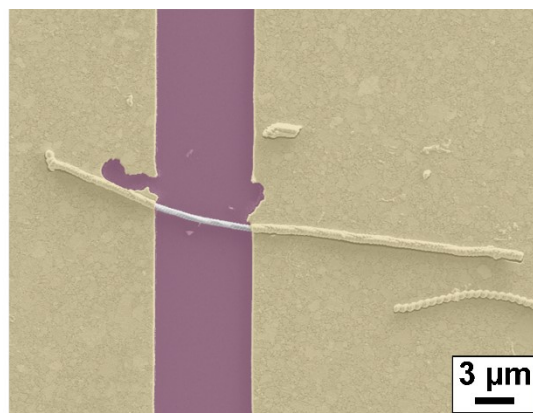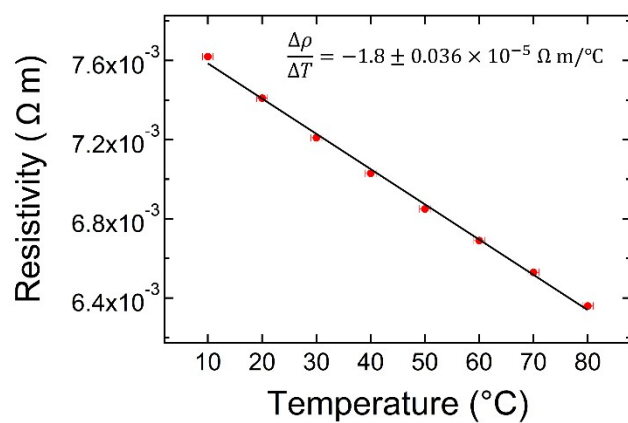
Device 3

Device 4

Device 5

Device 6

$$\frac{\Delta\rho}{\Delta T} = -7.9 \pm 0.36 \times 10^{-6} \ \Omega\,\text{m/°C}$$

Device 7

$$\frac{\Delta\rho}{\Delta T} = -2.3 \pm 0.032 \times 10^{-6} \ \Omega\,\text{m/°C}$$

Device 8

$$\frac{\Delta\rho}{\Delta T} = -1.6 \pm 0.043 \times 10^{-6} \ \Omega\,\text{m/°C}$$

Device 9

$$\frac{\Delta\rho}{\Delta T} = -1.3 \pm 0.056 \times 10^{-6}\ \Omega\,\text{m/°C}$$

Device 10

$$\frac{\Delta\rho}{\Delta T} = -2.2 \pm 0.049 \times 10^{-6}\ \Omega\,\text{m/°C}$$

Device 11

$$\frac{\Delta\rho}{\Delta T} = -1.2 \pm 0.069 \times 10^{-6}\ \Omega\,\text{m/°C}$$